The Dissertation Committee for Rebika Shrestha Certifies that this is the approved version of the following dissertation:

Direct Measurement of Membrane Dipole Field In Complex Model Membranes Via Vibrational Stark Effect Spectroscopy Coupled with Molecular Dynamics Simulations

Committee:

Lauren J. Webb, Supervisor

Ron Elber

David A. Vanden Bout

Vernita Gordon

Jeanne Stachowiak

Direct Measurement of Membrane Dipole Field In Complex Model Membranes Via Vibrational Stark Effect Spectroscopy Coupled with Molecular Dynamics Simulations

by

Rebika Shrestha, B. S.

Dissertation

Presented to the Faculty of the Graduate School of

The University of Texas at Austin

in Partial Fulfillment

of the Requirements

for the Degree of

Doctor of Philosophy

The University of Texas at Austin

August 2016

Dedication

This dissertation is dedicated to my late grandfather, Chij Kumar Shrestha, for always believing in me and supporting me throughout my life. I am grateful to my loving and caring husband, Abhi Bickram Rana, and my family for their unconditional love and support.

Acknowledgements

I would like to gratefully acknowledge my scientific teachers and my peers in the Department of Chemistry at The University of Texas at Austin who have been tremendously supportive to me throughout this academic endeavor. I would like to thank my thesis advisor, Dr. Lauren J. Webb for giving me an opportunity to work on such an exciting research topic and for her continuous support and guidance for past five years. I want to express my deep gratitude to Dr. Ron Elber and Dr. Alfredo Cardeñas for a very successful and beneficial collaborative research. I would like to thank members of my doctoral committee: Dr. David Vanden Bout, Dr. Vernita Gordon and Dr. Jeanne Stachowiak for their scientific insights. I am very thankful to Cari M. Anderson for being such a joyous fellow researcher in this project. I appreciate your hard work and unceasing enthusiasm. Lastly, I am extremely humble towards the past and the current members of Webb Group: Dr. Annette Raigoza, Dr. Christina Ragain, Dr. David Walker, Dr. Andrew Ritchie, Dr. Jason Dugger, Dr. Ignacio Gallardo, Seth Norman, Joshua Slocum, Elisa Novelli, and Jeremy First for a harmonious learning environment. I wish you all the best on your future.

Direct Measurement of Membrane Dipole Field In Complex Model Membranes Via Vibrational Stark Effect Spectroscopy Coupled with Molecular Dynamics Simulations

Rebika Shrestha, PhD

The University of Texas at Austin, 2016

Supervisor: Lauren J. Webb

Abstract: The heterogeneous composition of a biological membrane creates a complex electrostatic environment that regulates membrane structure and function. In this work, we investigated the magnitude of the membrane dipole field, $\vec{F}_d$, located entirely within the low dielectric membrane interior as a function of membrane composition complexity. We directly measured $\vec{F}_d$ in vesicle model membrane composed of 1,2-dimyristoyl-*sn*-glycero-3-phosphocholine (DMPC) using vibrational Stark effect (VSE) shifts of nitrile oscillators systematically placed along the membrane interior coupled with extensive Molecular Dynamics (MD) simulations. We calculated the absolute magnitude of $\vec{F}_d$ in DMPC vesicles to be 8-11 MV/cm, at the high end of the range provided in literature. We increased the complexity of the membrane composition by intercalating cholesterol molecule at a wide range of concentration (0- 40 mol%) and found that cholesterol increased $\vec{F}_d$ at low concentration (~10 mol%), and decreased $\vec{F}_d$ at higher concentration (>10 mol%). This result, when compared to lipid bilayers containing a cholesterol

derivative, 6-ketocholestanol (6-kc) that differs from cholesterol by only a ketone functional group, was strikingly different. Using the spectral line widths obtained from Fourier-transform infrared spectroscopy experiments and molecular dynamic simulations on model lipid-sterol bilayers, we propose that the membrane dipole field is greatly correlated to the local membrane structure and organization regulated by the sterols in the bilayer. We propose that at low concentrations, cholesterol increases dipole field by increasing packing density of disordered lipids, cholesterol and their associated hydrogen bonded water dipoles whereas at high concentrations, the sterol decreases the field by forming liquid ordered state enriched in cholesterol, thus spacing out phospholipids along with water dipoles. 6-kc, on the other hand, is homogeneously distributed and increases hydrogen bonding with water dipoles via two polar groups on its sterol ring, thus never promoting ordered domain and increasing the dipole field monotonously.

We also investigated the translocation mechanism of positively, negatively and zwitterionic charged tryptophan molecules through a phospholipid bilayer using time dependent fluorescence spectroscopy and atomically detailed simulations. Both experiment and simulation reproduced the qualitative trend and suggested that the fastest permeation occurred for positively charged tryptophan. Molecular dynamics simulations revealed that the translocation mechanism was assisted by a local defect and the permeation process was insignificantly influenced by the long-range electrostatic interactions, such as the membrane dipole potential.

Table of Contents

List of Tables

List of Figures

Chapter 1 Introduction

1.1 Membrane Electrostatics

Biological membranes are dynamic structures composed of lipid bilayer forming a semipermeable barrier between the interior of the cell and the extracellular matrix. The self-assembling lipid molecules make a bilayer scaffold to which small molecules and membrane proteins intercalate and create a heterogeneous and complicated membrane system. Plasma membranes, in particular, mostly consist of phospholipids comprised of polar head groups, glycerol backbone and apolar tail region. Figure 1.1 represents a molecular structure of the common biological phosphocholine lipid 1,2-dimyristoyl-sn-glycero-3-phosphocholine (DMPC), which contains a phosphocholine head group, glycerol backbone and fourteen-carbon long alkyl tail. The aqueous phase surrounding the charged lipid head group region consists of ions, water molecules and often the charged proteins, peptides and sterols intercalated onto and within the bilayer. This creates a complex array of electrostatic potentials about and within the membrane. These electrostatic potentials are a major driving force behind important membrane functions such as the binding of proteins and ions to the membrane, the structural conformation and function of those proteins, and the transportation of ions and metabolites across ion channels.[1-3]

Conceptually, the total electrostatic potential profile in and at biological membranes is a complicated sum of three components that are distributed uniformly and

at particular distance from membrane center, shown schematically in Figure1.1-2.[1-3] The first component is the transmembrane potential (V_{trans}), which is a result of the difference in ion concentrations across a bilayer.[1] Lipid membranes are known to be selectively permeable to ions and macromolecules. This creates ion gradients and therefore, an electrical potential difference at the two aqueous phases across a membrane; the magnitude of the transmembrane potential in biological membranes ranges from 10 – 100 mV generating an electric field up to 0.1 MV/cm.[1] The transmembrane potential is known to affect the ion transport, binding of transmembrane proteins and enzymatic activities.[1-3] The second component, the surface potential (V_s), originates from the charged species localized at the membrane-water interface and has been estimated by the Gouy-Chapman theory of diffuse double layer. The charged lipid head group exposed to the aqueous region attract oppositely charged ions in the bulk aqueous phase and cause an accumulation of charges at the interface creating a surface potential of 8 – 30 mV in magnitude, which drops to the bulk value over a few nanometers.[1-3] This potential generates a field of 0.01 MV/cm which spans the membrane-bulk water interface. [1-3] In biology, the surface potential and transmembrane potential have an additive effect on control and regulation of membrane functions.[1-3] For example, even though the transport of ions across a membrane is facilitated by the transmembrane potential, the amount of ions crossing the membrane barrier is dependent on the surface potential itself.

The third and the largest potential is the dipole potential (V_d), which results from the alignment of dipolar residues located in between the lipid-water interface and the

hydrocarbon-like interior of the membrane.[1] Based on previous studies, the magnitude of this potential is estimated to be about 100 – 1000mV. It is located entirely within the low dielectric hydrophobic interior of a membrane spanning over a small distance of a few nanometers, giving rise to a huge electric field of about 1 – 10 MV/cm.[4,5] However, the fact that it exists entirely within the membrane interior makes the direct measurement and control of this potential extremely challenging and therefore, it is the least understood electrostatic potential of all.

1.2 MEMBRANE DIPOLE FIELD

Membrane dipole field originates from the collection of molecular dipole moments at the membrane-water interface oriented towards the interior of the membrane. In the literature, the lipid polar head groups, the ester linkages to the glycerol moiety and the water molecules accumulated at the membrane interface have been established as the molecular origins of the dipolar strength within the membrane.[4-8] In a phospholipid molecule, the head group contains a positively charged choline group and negatively charged phosphate group separated over a distance of two C-C bonds producing a dipole moment of ~2 D.[4,5,7,8] The carbonyl groups of the ester linkages between the head group and the hydrocarbon chain contribute a dipole moment of ~ 1.8 D per carbonyl molecule. Lastly, the polar water molecules hydrogen bound to the carbonyls and the phosphate group at the membrane-water interface as well as in bulk have dipole moment of about 2 D per water molecule, and thus it is the major contributor to the membrane dipole potential.[4] The orientation and the density of these dipole moments within the membrane

interface regulate the dipole potential leading to a field as large as 1-10 MV/cm.[4,5] The field strength of such high magnitude alters the structure and orientation of membrane proteins and hence regulates many aspects of membrane biological functions such as ion-transport rates across lipid membranes,[9-13] membrane fusion,[14] redox reaction kinetics,[15] partitioning and translocation of small macromolecules such as Na^+-K^+-ATPase and phospholipase A_2,[16-19] and insertion and folding of membrane peptides like mitochondrial amphipathic signal peptide p25,[17] and simian immunodeficiency viral fusion peptide.[20]

Since its discovery by Liberman and Topaly in 1969, the membrane dipole potential has been studied using various experimental and theoretical techniques.[6, 7] Previously, the dipole potential has been estimated based on the potential difference across a lipid monolayer measured using a vibrating plate (Kelvin) method and an ionizing electrode circuits.[5] Similarly, Flewelling and Hubbell estimated the dipole potential of the egg phosphatidylcholine membrane to be 280 mV based on the translocation rate of lipophilic ions across the bilayer.[21,22] Recently, a flurry of voltage sensitive dyes such as RH421, di-8-ANEPPS, ANNINE-6, etc. have become popular probes for membrane dipole potential.[4,23-28] When embedded into the membrane, their chromophore lies in the head group region, where they are sensitive to the local electric field originating from the dipole potential. Likewise, the dipole field has also been evaluated using microscopy techniques such as atomic force microscopy[30] and cryo-electron microscopy[29] and molecular dynamic (MD) simulations.[22, 31]

However, all of these measurement techniques are indirect and the results are puzzling. For example, the conductance and ion translocation methods are indirect electrical measurements; use of bulky charged dye molecules perturbs the native membrane environment and the dye itself might be sensitive to changes in physical properties such as fluidity and phase changes in addition to the electric field. The microscopy techniques are also flawed in the sense that the sensitivity is low and the required pretreatment of samples such as freezing or collapsing to make supported lipid bilayers changes the native electrostatic features. The computational studies are heavily dependent on the type of force fields used and not all force fields have been optimized for lipids, therefore, the partial charges on individual atoms and the dipole moments of the lipid head groups varies with the force field used. Lastly, different water models, variations in treatment of long-range electrostatics and lack of consideration of polarization effects strongly affect the dipole potential calculation.

Here, we have employed a novel spectroscopy technique called vibrational Stark effect (VSE) spectroscopy to directly measure the magnitude and the direction of the membrane dipole field as function of its complexity. In VSE spectroscopy, we measure the influence of an electric field on the vibrational frequency of a molecule.mode of a chromophore. Compared to previous spectroscopic techniques, the probes used in this technique are small diatomic molecules and minimally invasive to the native structure. The theory has been well developed and tested in experiments to measure the electrostatic fields at protein-protein interfaces and the results coincide well with the literature.

1.3 VIBRATIONAL STARK EFFECT SPECTROSCOPY

Molecular vibrations are sensitive to the local electrostatic fields. When a diatomic molecule is excited to a higher vibrational energy level, the bond length slightly increases due to its anharmonicity; if there is a charge separation between the two atoms, the dipole moment differs between the ground vibrational state and the excited vibrational state. An external electric field, $\vec{F}$, when applied to a matrix of dipoles, stabilizes these dipoles differently; as a result, there is a shift in the vibrational absorption energy, ΔE, that is linear with the difference in dipole moments, $\Delta\vec{\mu}$, and the applied field, $\vec{F}$. This is called the vibrational Stark effect (VSE) and given by Equation 1-1

$$\Delta E = hc\Delta\nu_{obs} = -\Delta\vec{\mu} \bullet \vec{F} \qquad (1\text{-}1)$$

where h is the Planck's constant, c is the speed of light and $\Delta\nu_{obs}$ is the change in vibrational frequency. We can measure $\Delta\nu_{obs}$ spectroscopically by obtaining the infrared spectrum of the oscillator in the absence and presence of an electric field, $\vec{F}$. The difference in the dipole moment, $\Delta\vec{\mu}$, also called the Stark tuning rate, is a measure of sensitivity of an oscillator's vibrational frequency to an external electric field. If the direction of the applied electric field aligns parallel to the direction of $\Delta\vec{\mu}$, the absorption energy of the oscillator shifts towards lower energy and if they align anti parallel, the absorption energy shifts towards higher energy. We show this schematically in Figure 1.3-1 where the black spectrum represents the reference spectrum and the red and blue

spectrum represent shift towards either lower or higher energy respectively in presence of an external field.

Previously, VSE spectroscopy has been applied to measure the local electrostatic field within proteins, nucleic acids as well as membrane bicelles. For example, in their pioneering work, Boxer and coworkers reported the first ever experimental measurement of vibrational Stark effect in proteins, providing quantitative information on the sensitivity of a vibrational transition to an applied electric field.[34] They measured the vibrational Stark effect for a carbonyl vibration bound to a heme iron in myoglobin as they perturbed the local electrostatic environment via changes in pH values and mutations to the wild type deoxymyoglobin. They further extended the strategy to a modified picketed fence porphyrin and cytochrome c and determined that in all cases the Stark tuning rate of C=O did not change significantly, and therefore the carbonyl stretch frequency for C=O bound to the heme iron is a sensitive and anisotropic local reporter of changes in electric field.[34] Since then, VSE of a number of site-specific infrared probes such as the O-H stretch modes,[35] S-H stretch mode ,[36] nitrile stretch ($C \equiv N$),[37,38,39] and azide bond (N_3)[39] molecules convoluted within biological moieties have been applied to probe electrostatic forces at complex biological systems such as protein-protein interfaces.[40-49]

In this study, we employ the VSE spectroscopy of the nitrile-stretching band to probe the local electrostatic field located entirely within the interior of a complex biological model membrane. The nitrile-stretching mode is a popular reporter of the electrostatic environment in biological systems for several reasons. (1) The vibrational

transition gives rise to an intense narrow peak and it occurs in an uncluttered region of infrared spectrum separated from absorption bands of other functional groups found in proteins and membranes. (2) The probe itself is a small diatomic molecule and perturbs the system minimally. (3) The polarity of the nitrile is between an amide group and a methylene group, thus it can easily be placed inside the hydrophobic interior of a protein or membrane bilayer as well as accommodated in a solvent exposed environment. (4) Most importantly, the nitrile band has been extensively studied both theoretically and experimentally.[47,48,49,50] Nitriles are incorporated at regions of interests by placing a nitrile derivatized amino acid such as cyanoalanine, 5-cyanotryptophan, cyanocysteine[46] or *p*-cyanophenyalanine.[39,47,49,50,51,52] Nitrile derivatized unnatural amino acids are particularly attractive because they create minimal perturbation to the native biological structure. It can be incorporated into the polypeptide sequence of interest in a fairly convenient manner *in vitro* via post-translational amino acid modification[44] or standard solid phase peptide synthesis[53,54] or *in vivo* by direct subcloning,[55] suppressor tRNA modifications[56,57] and amino acid replacement techniques.[58-60]

VSE spectroscopy experiments are performed in two steps. First, a suitable infrared probe is chosen and its sensitivity to an electric field, otherwise known as the Stark tuning rate, is calibrated by measuring its response towards a known applied electric field. Once calibrated, the vibrational probe is then placed into a region of interest and used as a sensitive, local and directional reporter of the electrostatic field at local vicinity of the probe. In our experiments, we investigated the absolute dipole electric field that spans from the membrane-water interface to the hydrophobic interior of the

membrane by using a nitrile-derivatized amino acid, *p*-cyanophenyalanine (*p*-CN-Phe). The Stark tuning rate of this probe has been previously calibrated by Boxer and his group to be 0.67 cm^{-1}/(MV/cm).[51,52] We systematically placed the nitrile infrared probe across a lipid bilayer, starting near the membrane-water interface and moving towards the hydrophobic core. The local electrostatic environments at these two locations are entirely different; the membrane-water interface is very heterogeneous with charged lipid head groups, ions and water molecules, whereas the hydrophobic core is homogeneous and mostly comprised of nonpolar hydrocarbons. The nitrile-stretching mode is sensitive to the electrostatic features at its vicinity, as a result of which the vibrational absorption energy of the nitrile shifted towards higher wavenumber upon its placement in the membrane interior compared to the membrane-water interface.

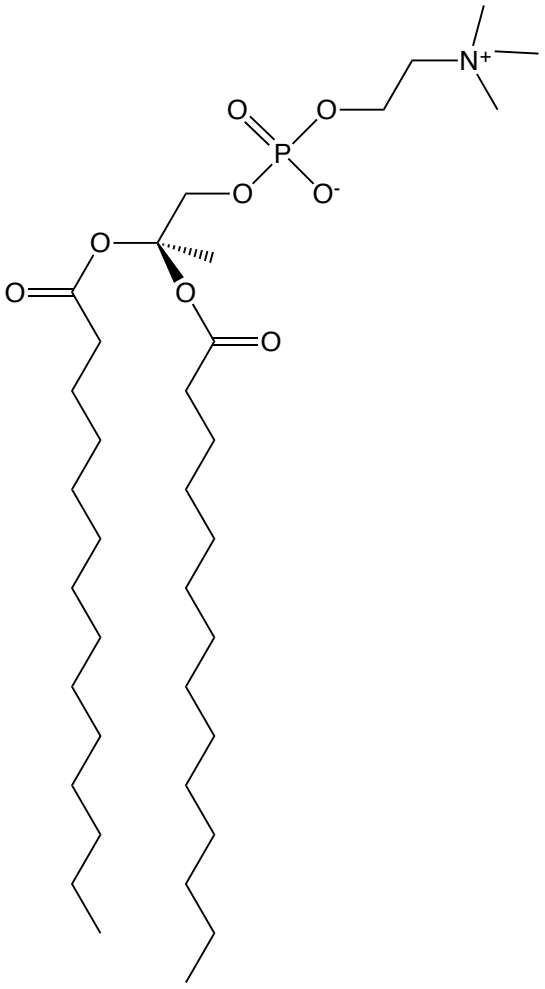

Figure 1.1: Molecular structure of a phospholipid, 1,2-dimyristoyl-sn-glycero-3-phosphocholine (DMPC) containing a phosphocholine head group, glycerol backbone and 14 carbon long alkyl tail.

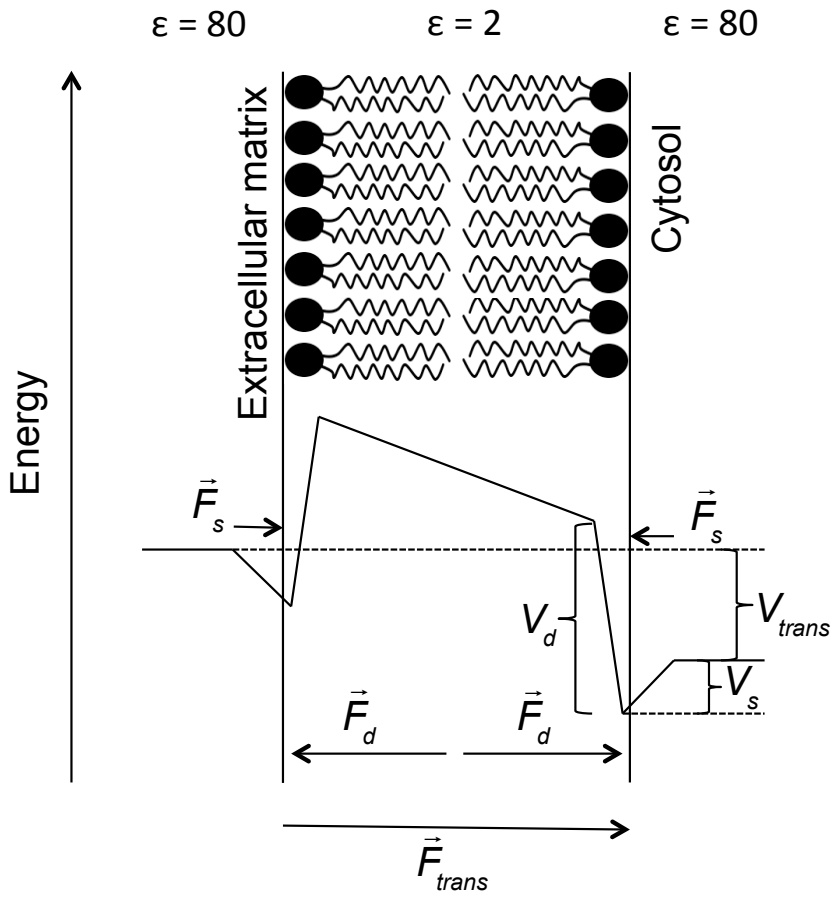

Figure 1.2: Schematic representation of the total electrostatic profile across a lipid bilayer membrane. V_{trans}, V_s and V_d represent the transmembrane potential, surface potential and dipole potential respectively and $\vec{F}_{trans}$, $\vec{F}_s$ and $\vec{F}_d$ represent their corresponding fields. The dipole field, F_d is the largest and least understood of all membrane potential.

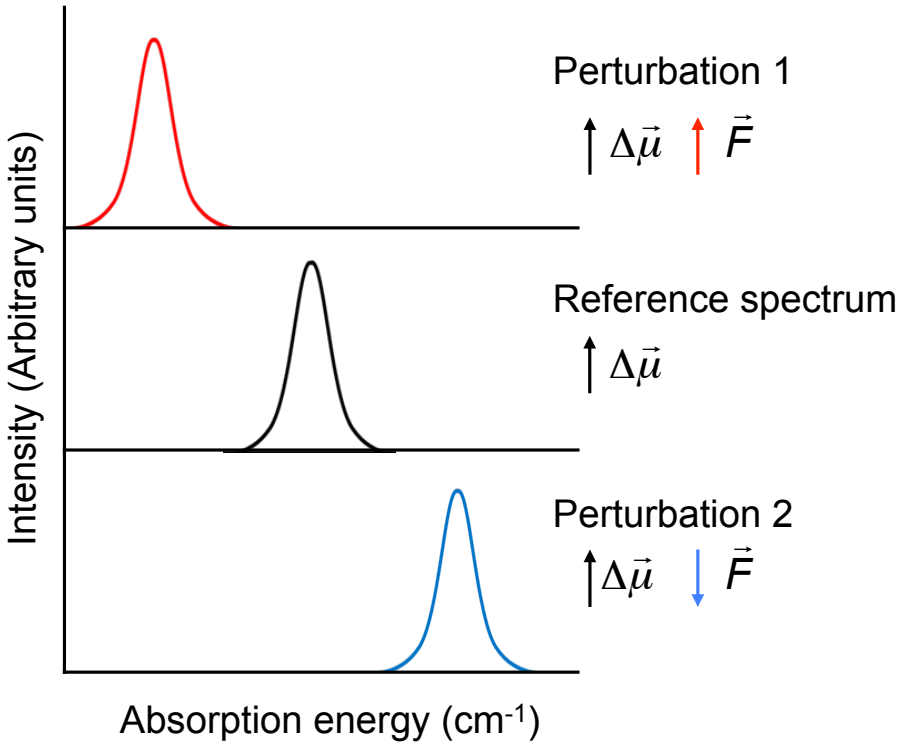

Figure 1.3: Schematic representation of VSE spectroscopy. $\Delta\vec{\mu}$ and $\Delta\vec{F}$ are the Stark tuning rate of the probe and change in electrostatic field, respectively. If $\Delta\vec{F}$ is aligned parallel to $\Delta\vec{\mu}$, the absorption energy of the probe shifts to lower frequency and if aligned anti parallel, the absorption energy shifts to higher frequency.

1.4 REFERENCES

1. Honig, B. H.; Hubbell, W. L.; Flewelling, R. F. Electrostatic Interactions in Membranes and Proteins. *Annu. Rev. Biophys. Biophys. Chem.* **1986**, *15*, 163-193.
2. McLaughlin, S. The Electrostatic Properties of Membranes. *Annu. Rev. Biophys. Biophys. Chem.* **1989**, *18*, 113-136.
3. Cevc, G. Membrane Electrostatics. *Biochim. Biophys. Acta*. **1990**, *1031*, 311-382.
4. Clarke, R. J. The Dipole Potential of Phospholipid Membranes and Methods for Its Detection. *Adv. Colloid Interface Sci.* **2001**, *89-90*, 263-281.
5. Brockman, H. Dipole Potential of Lipid Membranes. *Chem. Phys. Lipids.* **1994**, *73*, 57-79.
6. Liberman, Y. A.; Topaly, V. P.
7. Wang, L. Measurements and Implications of the Membrane Dipole Potential. *Annu. Rev. Biochem.* **2012**, *81*, 615-635.
8. Bechinger, B; Seelig, J. Interactions of Electric Dipoles with Phospholipid Head Groups. A ^{2}H and ^{31}P NMR Study of Phloretin and Phloretin Analogues in Phosphatidylcholine Membranes.
9. Schamberger, J.; Clarke, R. J. Hydrophobic Ion Hydration and the Magnitude of the Dipole Potential. *Biophys. J.* **2002**, *82*, 3081-3088.
10. Duffin, R. L.; Garrett, M. P.; Flake, K. B.; Durrant, J. D.; Busath, D. D. Modulation of Lipid Bilayer Interfacial Dipole Potential by Phloretin, RH421, and 6-ketocholestanol as Probed by Gramicidin Channel Conductance. *Langmuir* **2003,** *19*, 1439–1442.

11. Phillips, L. R.; Cole, C. D.; Hendershot, R. J.; Cotten, M.; Cross, T. A.; Busath, D. D. Noncontact Dipole Effects on Channel Permeation. III. Anomalous Proton Conductance Effects in Gramicidin. *Biophys. J.* **1999,** *77*, 2492–2501.

12. Hladky, S. B. The Energy Barriers to Ion Transport by Nonactin Across Thin Lipid Membranes. *Biochim. Biophys. Acta* **1974**, *352*, 71−85.

13. Bala, S.; Kombrabail, M. H.; Prabhananda, B. S. Effect of Phloretin on Ionophore Mediated Electroneutral Transmembrane Translocations of H(+), K(+) and Na(+) in Phospholipid Vesicles. *Biochim. Biophys. Acta*. **2001**, *1510*, 258−269

14. Cladera, J.; Martin, I.; Ruysschaert, J. M.; O'Shea, P. Characterization of the sequence of interactions of the fusion domain of the simian immunodeficiency virus with membranes. *J. Biol. Chem.* **1999**, *274*, 29951–29959.

15. Alakoskela, J.-M. I.; Kinnunen, P. K. J. Control of a Redox Reaction on Lipid Bilayer Surfaces by Membrane Dipole Potential. *Biophys. J.* **2001**, *80*, 294–304.

16. Alakoskela, J.-M. I.; Soderlund, T.; Holopainen, J. M.; Kinnunen, P. K. J. Dipole Potential and Head-group Spacing are Determinants for the Membrane Partitioning of Pregnanolone. *Mol. Pharmacol*. **2004**, *66*, 161–168.

17. Cladera, J.; O'Shea, P. Intramembrane Molecular Dipoles Affect the Membrane Insertion and Folding of a Model Amphiphilic Peptide. *Biophys. J.* **1998**, *74*, 2434–2442.

18. Starke-Peterkovic, T.; Turner, N.; Else, P. L.; Clarke, R. J. Electric Field Strength of Membrane Lipids From Vertebrate Species: Membrane Lipid Composition and

Na1,K1-ATPase molecular activity. *Am. J. Physiol. Regul. Integr. Comp. Physiol.* **2005**, *288*, R663–R670.

19. Maggio, B. Modulation of Phospholipase A2 by Electrostatic Fields and Dipole Potential of Glycosphingolipids in Monolayers. *J. Lipid Res.* **1999**, *40*, 930–939.
20. Buzon, V.; Cladera, J. Effect of Cholesterol on the Interaction of the HIV GP41 Fusion Peptide with Model Membranes. Importance of the Membrane Dipole Potential. *Biochem* **2006**, *45*, 15768−15775.
21. Flewelling, R. F.; Hubbell, W. L. The Membrane Dipole Potential in a Total Membrane Potential Model. Applications to Hydrophobic Ion Interactions with Membranes. *Biophys. J.* **1986**, *49*, 541-552.
22. Franklin, J. C.; Cafiso, D. S. Internal Electrostatic Potentials in Bilayers: Measuring and Controlling Dipole Potentials in Lipid Vesicles. *Biophys. J.* **1993**, *65*, 289-299.
23. Gross, E.; Bedlack, R. S.; Loew, L. M. Dual-Wavelength Ratiometric Fluorescence Measurement of the Membrane Dipole Potential. *Biophys. J.* **1994**, *67*, 208-216.
24. Clarke, R. J. Effect of Lipid Structure on the Dipole Potential of Phosphatidylcholine Bilayers. *Biochim. Biophys. Acta* **1997**, *1327*, 269-278.
25. Klymchenko, A.S.; Duportail, G.; M´ely, Y.; Demchenko, A. P. Ultrasensitive Two-Color Fluorescence Probes for Dipole Potential in Phospholipid Membranes. *Proc. Natl. Acad. Sci. USA* **2003**, *100*, 11219–24.

26. Demchenko, A. P.; M´ely, Y.; Duportail, G.; Klymchenko, A. S. Monitoring Biophysical Properties of Lipid Membranes by Environment-Sensitive Fluorescent Probes. *Biophys. J.* **2009**, *96*, 3461–3470.

27. Demchenko, A. P.; Yesylevskyy, S. O. Nanoscopic Description of Biomembrane Electrostatics: Results of Molecular Dynamics Simulations and Fluorescence Probing. *Chem. Phys. Lipids.* **2009**, *160*, 63–84.

28. Zouni, A.; Clarke, R. J.; Holzwarth, J. F. Kinetics of the Solubilization of Styryl Dye Aggregates by Lipid Vesicles. *J. Phys. Chem*. **1994**, *98*, 1732–1738.

29. Wang, L.; Bose, P.S.; Sigworth, F. J. Using Cryo-EM to Measure the Dipole Potential of a Lipid Membrane. *PNAS.* **2006**, *103*, 18528-18533.

30. Yang, Y.; Mayer, K. M.; Wickremasignhs, N. S.; Hafner, J. H. Probing the Lipid Membrane Dipole Potential by Atomic Force Microscopy. *Biophys. J.* **2008**, *95*, 5193-5199.

31. Schamberger, J.; Clarke, R. J. Hydrophobic Ion Hydration and the Magnitude of the Dipole Potential. *Biophys. J.* **2002**, *82*, 3081-3088.

32. Chattopadhyay, A.; Boxer, S. G. Vibrational Stark Effect Spectroscopy. *J. Am. Chem. Soc.* **1995***, 117*, 1449-1450.

33. Fried, S. D.; Boxer, S. G. Measuring Electric Fields and Noncovalent Interactions Using the Vibrational Stark Effect. *Acc. Chem. Res.* **2015**, *48*, 998-1006.

34. Park, E. S.; Andrews, S. S.; Hu, R. B.; Boxer, S. G. Vibrational Stark Spectroscopy in Proteins: A Probe and Calibration for Electrostatic Fields. *J. Phys. Chem. B* **1999**, *103*, 9813-9817.

35. Saggu, M.; Levinson, N. M.; Boxer, S. G. Direct Measurements of Electric Fields in Weak O−H···π Hydrogen Bonds. *J. Am. Chem. Soc.* **2011**, *133*, 17414−17419.

36. Saggu, M.; Levinson, N. M.; Boxer, S. G. Experimental Quantification of Electrostatics in X−H···π Hydrogen Bonds. *J. Am. Chem. Soc.* **2012**, *134*, 18986−18997.

37. Andrews, S. S.; Boxer, S. G. Vibrational Stark Effects of Nitriles I. Methods and Experimental Results. *J. Phys. Chem. A.* **2000**, *104*, 11853−11863.

38. Fafarman, A. T.; Boxer, S. G. Nitrile Bonds as Infrared Probes of Electrostatics in Ribonuclease S. *J. Phys. Chem. B* **2010**, *114*, 13536− 13544.

39. Waegele, M. M.; Culik, R. M.; Gai, F. Site-Specific Spectroscopic Reporters of the Local Electric Field, Hydration, Structure, and Dynamics of Biomolecules. *J. Phys. Chem. Lett.* **2011**, *2*, 2598-2609.

40. Suydam, I. T.; Boxer, S. G. Vibrational Stark Effects Calibrate the Sensitivity of Vibrational Probes for Electric Fields in Proteins.*Biochem* **2003**, *42*, 12050−12055.

41. Fafarman, A. T.; Boxer, S. G. Nitrile Bonds as Infrared Probes of Electrostatics in Ribonuclease S. *J. Phys. Chem. B.* **2010**, *114*, 13536–13544.

42. Silverman, L. N.; Pitzer, M. E.; Ankomah, P. O.; Boxer, S. G.; Fenlon, E. E. Vibrational Stark Effect Probes for Nucleic Acids. *J. Phys. Chem. B.* **2007**, *111*, 11611-11613.

43. Getahun, Z.; Huang, C. Y.; Wang, T.; DeLeon, B.; DeGrado, W. F.; Gai, F. Using Nitrile-Derivatized Amino Acids as Infrared Probes of Local Environment. *J. Am. Chem. Soc.* **2003**, *125*, 405–411.

44. Stafford, A. J.; Ensign, D. L.; Webb, L. J. Vibrational Stark Effect Spectroscopy at the Interface of Ras and Rap1A Bound to the Ras Binding Domain of RalGDS Reveals an Electrostatic Mechanism for Protein-Protein Interaction. *J. Phys. Chem. B* **2010**, *114*, 15331–15344.

45. Webb, L. J.; Boxer, S. G. Electrostatic Fields Near the Active Site of Human Aldose Reductase: 1. New Inhibitors and Vibrational Stark Effect Measurements. *Biochem.* **2008**, *47*, 1588-1598.

46. Alfieri, K. N.; Vienneau, A. R.; Londergan, C. H. Using Infrared Spectroscopy of Cyanylated Cysteine To Map Membrane Binding Structure and Orientation of the Hybrid Antimicrobial Peptide CM15. *Biochem* **2011**, *50*, 11097-11108.

47. Mukherjee, S.; Chowdhury, P.; DeGrado, W. F.; Gai, F. Site- Specific Hydration Status of an Amphipathic Peptide in AOT Reverse Micelles. *Langmuir* **2007**, *23*, 11174–11179.

48. Tucker, M. J.; Getahun, Z.; Nanda, V.; DeGrado, W. F.; Gai, F. A New Method for Determining the Local Environment and Orientation of Individual Side Chains of Membrane-Binding Peptides. *J. Am. Chem. Soc.* **2004**, *126*, 5078–5079.

49. Liu, J.; Strzalka, J.; Tronin, A.; Johansson, J. S.; Blasie, J. K. Mechanism of Interaction between the General Anesthetic Halothane and a Model Ion Channel

Protein, II: Fluorescence and Vibrational Spectroscopy Using a Cyanophenylalanine Probe. *Biophys. J.* **2009**, *96*, 4176–4187.

50. Hu, W.; Webb, L. J. Direct Measurement of the Membrane Dipole Field in Bicelles Using Vibrational Stark Effect Spectroscopy. *J. Phys. Chem. Lett.* **2011**, *2*, 1925-1930.
51. Andrews, S. S.; Boxer, S. G. Vibrational Stark Effects of Nitriles I. Methods and Experimental Results. *J. Phys. Chem. A* **2000**, *104*, 11853–11863.
52. Andrews, S. S.; Boxer, S. G. Vibrational Stark Effects of Nitriles II. Physical Origins of Stark Effects from Experiment and Perturbation Models. *J. Phys. Chem. A* **2002**, *106*, 469–477.
53. Ayers, B.; Blaschke, U. K.; Camarero, J. A.; Cotton, G. J.; Holford, M.; Muir, T. W. Introduction of Unnatural Amino Acids into Proteins Using Expressed Protein Ligation. *Biopolymers* **1999**, *51*, 343–354.
54. Cotton, G. J.; Muir, T. W. Generation of a Dual-Labeled Fluorescence Biosensor for Crk-II Phosphorylation Using Solid-Phase Expressed Protein Ligation. *Chem. Biol.* **2000**, *7*, 253–261.
55. Heim, R.; Prasher, D. C.; Tsien, R. Y. Wavelength Mutations and Posttranslational Autooxidation of Green Fluorescent Protein. *Proc. Natl. Acad. Sci. U.S.A.* **1994**, *91*, 12501–12504.
56. Furter, R. Expansion of the Genetic Code: Site-Directed p- Fluoro-phenylalanine Incorporation in E. coli. *Protein Sci.* **1998**, *7*, 419–426.

57. Wang, L.; Brock, A.; Herberich, B.; Schultz, P. G. Expanding the genetic code of E. coli. *Science* **2001**, *292*, 498–500.

58. Cowie, D. B.; Cohen, G. N. Biosynthesis by E. coli of Active Altered Proteins Containing Selenium Instead of Sulfur. *Biochim. Biophys. Acta* **1957**, *26*, 252–261.

59. Brawerman, G.; Ycas, M. Incorporation of the Amino Acid Analog Tryptazan into the Proteins of E. coli. Arch. *Biochem. Biophys.* **1957**, *68*, 112–117.

60. Munier, R.; Cohen, G. N. Incorporation of Structural Analo- gues of Amino Acid into the Bacterial Proteins during Their Synthesis in Vivo. *Biochim. Biophys. Acta* **1959**, *31*, 378–391.

Chapter 2 Materials And Methods

2.1 Characterization of Vesicles

2.1.1 Materials

1,2-dimyristoyl-*sn*-glycero-3-phosphocholine (DMPC) powders were purchased from Avanti Polar Lipids, Inc and were used without further purification. Hepes, NaN_3 and D_2O were purchased from Sigma Aldrich. $PrCl_3 \bullet 6H_2O$ was purchased from Alfa Aesar. HPLC grade water and Chloroform were purchased from Fisher Scientific. All peptides were synthesized using standard Fmoc solid-state peptide synthesis.

2.1.2 Sample Preparation

About 30.0 mg of DMPC powder was dissolved in 2 mL of chloroform and dried under vacuum for at least 2 hours before it was introduced into a N_2-glove box overnight. The dried lipid film was then hydrated in 1.5 mL of 10 mM Hepes buffer, pH 6.7, maintained at a temperature above 23^oC, which is the melting temperature (T_m) for DMPC. The mixture was vigorously mixed using a vortex mixer for 5 minutes and then sonicated with a bath sonicator using 16 – 18 Watts power in an ice bath until the milky solution (indicative of multilamellar vesicles) turned into a hazy translucent solution (indicative of SUVs). Sonication was performed at a cycle of 30 seconds pulse-on and 15 seconds pulse-off to minimize sample degradation by over heating. The sample was then centrifuged for 60 minutes at 12000 g to remove any titanium particles released by the tip and lipid and peptide aggregates. The sample was stored at a temperature above T_c and

was stable for three to five days. Peptides and cholesterol to be incorporated into the vesicles were added to the lipids before dissolving in chloroform.

2.1.3 ^{31}P NMR Spectroscopy

Samples for ^{31}P NMR spectroscopy were prepared by mixing 150 µL of D_2O and 550 µL of vesicle sample in a NMR tube. The experiments were carried out at 202.343 MHz on a Varian INOVA-500 NMR at 27°C. The spectra were processed using Mrestnova software.

2.1.4 Dynamic Light Scattering

About 1 mL of clear sample solution was collected in a disposable polystyrene cuvette that was rinsed with ethanol and dried just before adding samples. The particle size measurements were made on a Malvern Zetasizer Nano ZS instrument at temperature of 25 °C with a viscosity of 0.8872 cP and refractive index of 1.330.

2.1.5 Atomic Force Microscopy

2.5 µL of sample was deposited on a freshly cleaved mica surface. AFM imaging was performed using general purpose, n-type silicon cantilevers with a spring constant of 40 N/m and a resonance frequency of 325 kHz. AFM images were taken on an Asylum MFP-3D Stand Alone AFM operating in tapping-mode. Images were processed to remove noise along the fast-scan direction and flattened using Gwddyion software.

2.2 VIBRATIONAL STARK EFFECT SPECTROSCOPY IN DMPC BILAYER

2.2.1 Materials

1,2-dimyristoyl-*sn*-glycero-3-phosphocholine (DMPC) powders were purchased from Avanti Polar Lipids, Inc and were used without further purification. Hepes, NaN_3 and D_2O were purchased from Sigma Aldrich. $PrCl_3 \bullet 6H_2O$ was purchased from Alfa Aesar. HPLC grade water and Chloroform were purchased from Fisher Scientific. All peptides were synthesized using standard Fmoc solid-state peptide synthesis.

2.2.2 Vesicle Preparation

About 30.0 mg of DMPC powder was dissolved in 2 mL of chloroform and dried under vacuum for at least 2 hours before it was introduced into a N_2-glove box overnight. The dried lipid film was then hydrated in 1.5 mL of 10 mM Hepes buffer, pH 6.7, maintained at a temperature above 23^{o}C, which is the melting temperature (T_m) for DMPC. The mixture was vigorously mixed using a vortex mixer for 5 minutes and then sonicated with a bath sonicator using 16 – 18 Watts power in an ice bath until the milky solution (indicative of multilamellar vesicles) turned into a hazy lipid solution (indicative of SUVs). Sonication was performed at a cycle of 30 seconds pulse-on and 15 seconds pulse-off to minimize sample degradation by over heating. The sample was then centrifuged for 60 minutes at 12000 g to remove any titanium particles released by the tip and lipid and peptide aggregates. The sample was stored at a temperature above T_c and was stable for three to five days. Peptides and cholesterol to be incorporated into the vesicles were added to the lipids before dissolving in chloroform.

2.2.3 Circular Dichroism Spectroscopy

To collect CD spectra, vesicle solutions had to be further diluted to avoid saturating the detector. 1 and 0.5 mM solutions were diluted by factors of 1/10 and 1/5, respectively, resulting in solutions that were 0.1 mM overall in peptide. CD spectra were collected in both buffer and TFE solvent. The initial concentrations of 1 and 0.5 mM corresponded to 900 and 450 peptides per vesicle, respectively. CD spectra were recorded using a 1 mm path length quartz cell on a Jasco J-815 CD spectrometer over the wavelength range 190−250 nm at 0.2 nm resolution, a scanning rate of 50 nm/min, and a response time of 4 s. The spectra were background subtracted using 10 mM Hepes buffer as the background with Spectra Manager for Windows 95/NT Spectra Analysis software.

2.2.4 Molecular Dynamics Simulation

Dr. Ron Elber and Dr. Alfredo Cardeñas performed MD simulations of two of the helical systems probed in the experiments, αLAX(16) and αLAX(25) (i.e., the inner- and outermost nitrile positions), in a bilayer of DMPC molecules. All simulations were performed with the program MOIL[1,2] using a combination of the united-atom Berger force field[3] for the acyl chain atoms of the lipid molecules and the OPLS force field[4] for their headgroup region and the peptide atoms. The CHARMM-GUI membrane builder facility[5,6] was used to set up the initial configurations of the membrane-intercalated peptide system. The simulated bilayer membrane contained 128 DMPC molecules (64 in each leaflet), 5630 TIP3P water molecules,[7] and one of the two simulated helical peptides (αLAX(16) or αLAX(25)). The initial configurations of the peptides were taken from a

previous study, in which model α- helices were constructed with Avogadro 1.0, an open-source molecular modeling tool.[8] Initially, the peptides were embedded vertically inside the bilayer systems with the helical axis parallel to the normal to the membrane surface. There were 23025 total atoms for the αLAX(16) simulation and 23022 atoms for the αLAX(25) simulation. The dimensions of the simulation boxes were 63.4 × 63.4 × 80.0 $Å^3$. Periodic boundary conditions were imposed in the three spatial directions, and the particle mesh Ewald method[9] was used for long-range electrostatic interactions with a grid of 64 × 64 × 80. The cutoffs for van der Waals interactions and for the real space component of the electrostatics forces were set to 9.8 Å. In all the simulations, they constrained the water bond length and angles with a matrix implementation of the SHAKE algorithm.[10,11] The simulations were done with multiple time steps according to r-RESPA,[12] with a 1 fs time step to integrate the bonding, van der Waals, and real-space component of the Ewald sum and a 4 fs time step to evaluate the reciprocal-space component of the Ewald sum. After a 50 ns equilibration period, production runs of 100 ns for αLAX(16) and 200 ns for αLAX(25) were carried out at 298 K and constant volume. Configurations were saved every 1 ps for determination of the distribution of tilt and nitrile probe angles. Convergence of the sampled configurations was assessed by estimating block averages of the tilted angle of the helix vector with respect to the membrane axis. The atomic positions of the Cα of H1 and H31 were used to estimate the helix vector. The sampled configurations from the molecular dynamics configurations were also used to compute the electric field at the position of the nitrile probe. For the calculation of the electric field, we placed a unit charge at the position of Cα in the nitrile

probe and use Coulomb's law with a larger cutoff of 18 Å to minimize truncation errors for the estimate of the electric field.[13]

2.2.5 Fourier-Transform Infrared Spectroscopy

Fourier transform infrared (FTIR) measurements of the nitrile absorption energy were recorded at room temperature in a sample cell comprised of two sapphire windows separated by 125 μm thick PETE spacers in a Bruker Vertex 70 FTIR instrument. The sample cell was illuminated with light in the range 2000−2500 cm^{-1} selected by a broad bandpass filter (Spectrogon, Parsippany, NJ) placed in front of the instrument's IR source. Spectra were collected with a liquidnitrogen-cooled indium antimide (InSb) detector and were composed of 3000 scans at 2.0 cm^{-1} spectral resolution. Background-subtracted spectra were fitted to a single Gaussian line shape with a custom least-squares fitting program to determine the peak center, ν_{obs}, and the full width at half-maximum (FWHM). Uncertainty in absorption energy is reported as the standard deviation of at least three measurements.

2.3 Effect of Cholesterol on Membrane Dipole Field

2.3.1 Materials

1,2-dimyristoyl-*sn*-glycero-3-phosphocholine (DMPC) powder was purchased from Avanti Polar Lipids, Inc. (Alabaster, AL) and was used without further purification. Cholesterol, 6-ketocholestanol, Hepes, NaN_3, and D_2O were purchased from Sigma Aldrich (St. Louis, MO). $PrCl_3 \cdot 6H_2O$ was purchased from Alfa Aesar (Ward Hill, MA).

HPLC grade water and chloroform were purchased from Fisher Scientific (Pittsburg, PA). All peptides were synthesized using standard Fmoc solid-state peptide synthesis and obtained from Abgent Technologies (San Diego, CA) and InnoPep (San Diego, CA).

2.3.2 Vesicle Preparation

Small unilamellar vesicles (SUV) were prepared using sonication as described in reference 14.[14] For samples containing cholesterol, about 30 mg of DMPC powder and a correct amount of cholesterol powder and lyophilized peptide (determined as described below) were taken together in a vial and dissolved in approximately 1 mL of chloroform. For samples containing 6-kc, a stock solution of 6-kc in methanol was made, from which the correct volume was added to the lipid and peptide solution in chloroform. The sample was then vortexed for 5 min, dried under vacuum for 2 hr, then transferred into a N_2(g)-purged glove box overnight. The dried sample was then hydrated with 1.5 mL of 10 mM Hepes buffer with 0.02% (w/v) NaN_3, pH 7.2, and maintained at a temperature above 23˚C, the gel-liquid crystal transition temperature (T_c) of DMPC. This was vortex mixed for 5 min to get a homogeneous distribution of multilamellar vesicles. Small unilamellar vesicles were obtained by placing the multilamellar vesicle suspension in a sonication bath maintained at 35˚C until the milky solution (indicative of multilamellar vesicles) cleared to slightly cloudy (indicative of light scattering by residual large particles remaining in the lipid suspension). These residuals were removed by centrifugation at 12000×*g* for approximately one hour to achieve a clear vesicle solution. The vesicle size distribution of each batch was determined using dynamic light scattering technique on

a Malvern Zetasizer Nano ZS instrument equipped with He-Ne light source (633 nm) and photodiode detector. The average vesicle diameter determined from all batches of vesicle samples was determined to be ~73 nm with standard deviation of 35 nm. All samples were stored at a temperature above T_c and were stable for up to 5 days.

Sterols were added at concentrations of 0, 5, 10, 15, 20, 30 and 40 mol% and peptides were added to make a total concentration of 1 mM. On average, a homogeneous distribution of 1 mM peptide a ratio of 33 peptides per 1000 lipids. The secondary structure of the peptides inside the vesicles was determined by circular dichroic (CD) spectroscopy using Jasco J-815 CD spectrometer. CD spectra were recorded using a 1 mm path length quartz cell over the range of 190 – 250 nm wavelength at 0.2 nm resolution, 50 nm/min scanning rate and 4 s response time and were background subtracted using 10 mM Hepes buffer as the background with Spectra Manager for Windows 95/NT Spectra Analysis software.

2.3.3 Fourier Transform Infrared Spectroscopy

Infrared spectra of vesicle samples containing the VSE probe were recorded at room temperature ($>T_c$) in a sample cell composed of two sapphire windows separated by 125 μm thick PETE spacers in a Bruker Vertex 70 FTIR instrument. The sample cell was illuminated with light in the range of 2000–2500 cm^{-1} selected by a broad band pass filter (Spectrogon, Parsippany, NJ) placed in front of the instrument's IR source. Spectra were collected with a liquid nitrogen-cooled indium antimide (InSb) detector and were composed of 3000 scans at 2.0 cm^{-1} spectral resolution. Background-subtracted spectra

were fit to a single Gaussian line shape with a custom least-squares fitting program to determine the peak center, ν_{obsd}, and full width at half maximum (FWHM). Uncertainty in absorption energy is reported as the standard deviation of at least three measurements.

2.3.4 Molecular Dynamics Simulations

Dr. Ron Elber and Dr. Alfredo Cardeñas computed molecular dynamics trajectories for the αLAX(16) at different compositions for the sterols in a bilayer of DMPC molecules. Three trajectories were computed for both cholesterol and 6-kc (Table 2). The total number of DMPC and sterol molecules was kept at 160 molecules in all the simulations.

They used the CHARMM-GUI[5,6] membrane builder facility to build a starting configuration of the membrane system with the helical peptide initially embedded inside the membrane, along the membrane axis. Initially they prepared the three cholesterol/DMPC systems with the membrane builder tool and used these configurations to build the three 6-kc/DMPC systems by adding the carbonyl bond in the corresponding sterol ring. The simulations were performed with the molecular simulation code MOIL[1,2] using a combination of the united-atom Berger force field for the acyl chain atoms of the lipid molecules and the OPLS force field for their head group region and the peptide atoms.[3,4] For the cholesterol, they used parameters developed by Pasenkiewicz-Gierula et al.,[15] and for the nitrile bond of the probe they used parameters from Price et al.[16] For water they used the SPC water model.[17]

After the initial setup, they heated the system to a target temperature of 298 K for a period of 2 ns and then performed 1 ns of equilibration at a constant pressure of 1 atm using a recently developed stochastic algorithm to sample the isobaric-isothermal ensemble.[18] Production runs of 200 ns were performed in the NVT ensemble with the last 100 ns of simulation data used for analysis.

Periodic boundary conditions were imposed in the three spatial directions and the smooth particle mesh Ewald method[9] was used for long-range electrostatic interactions with enough number of grids to satisfy the requirement of 1 grid/Å. The cutoffs for van der Waals interactions and for the real space component of electrostatics forces were set to 9.5 Å. In all the simulations they constrained water bond length and angles with a matrix implementation of the SHAKE algorithm.[10] The simulations were done with multiple time steps according to r-RESPA,[12,19] with 1 fs time step to integrate the covalent, van der Waals and real-space component of the Ewald sum, and a 4 fs time step to evaluate the reciprocal-space component of the Ewald sum. Configurations were saved every 1 ps for determination of the structural properties of the membrane systems. Convergence of the sampled configurations was assessed by estimating block averages of the tilted angle of the helix vector with respect to the membrane axis and the orientation of the probe angle with respect to the membrane axis. The atomic positions of the Cα of H1 and H31 were used to estimate the helix axis orientation. They also performed a 150 ns simulation of a pure lipid bilayer containing 160 DMPC molecules for comparison to the results of the helix/sterol/membrane systems.

Sterol composition	# of DMPC	# of sterol	# of water	Total # atoms
10 %	144	16	7150	28785
20 %	128	32	6909	27790
40 %	96	64	6355	21362

Table 2.1: Composition details of the simulations performed for cholesterol and 6-ketocholestanol.

2.4 UNASSISTED TRANSPORT OF TRYPTOPHAN ACROSS A LIPID BILAYER

2.4.1 Materials

1,2–dioleoyl-sn-glycerol-3-phosphocholine (DOPC, dissolved in chloroform) was purchased from Avanti Polar Lipids, Inc. L-tryptophan, N-acetyl-L-tryptophanamide (NATA), HEPES buffer, and NaN_3 were purchased from Sigma-Aldrich; citric acid monohydrate, sodium bicarbonate ($NaHCO_3$), and sodium carbonate anhydrous ($NaCO_3$) were purchased from Fisher Scientific; anhydrous sodium phosphate (Na_2HPO_4) was purchased from Mallindkrodt Pharmaceuticals. Buffers of various pH values were prepared in HPLC grade water purchased from Fischer Scientific. All chemicals were used as received unless noted.

2.4.2 Vesicle Preparation

Large unilamellar vesicles were prepared using an extrusion method. 945 μL of DOPC lipid in chloroform (25 mg/mL) was dried under vacuum for at least 2 hours

and placed in a N_2(g)-purged glove box overnight to get rid of any residual solvent. The dried lipids were hydrated in 1.0 mL of 10 mM Hepes buffer with 0.02% NaN_3, pH 7.2, for at least 30 minutes and agitated vigorously using a vortex mixer for 5 min. The hydrated lipid suspension was then subjected to at least ten cycles of a freeze-thaw process consisting of alternately placing the sample vial in liquid N_2 and warm water bath. The lipid suspension was then loaded into gas-tight syringe of a mini-extruder (Avanti Polar Lipids) and extruded through a membrane of 100 nm pore size twenty times, during which time the milky solution visibly cleared. The large unilamellar vesicles were then collected in a vial and stored at room temperature for further usage. For pH experiments, vesicles were prepared in three other buffers at pH 10.1 (0.1 M Na_2CO_3, 0.1M $NaHCO_3$), pH 5.5 (0.1 M Na_2CO_3, 0.1M $NaHCO_3$) and pH 2.4 (0.1M Citric acid, 0.2 M Na_2HPO_4). The average diameter of vesicles was determined to be 150 ± 17 nm using Malvern Zetasizer Nano ZS instrument equipped with a He-Ne laser light source to illuminate sample at wavelength of 633 nm and collected at a scattering angle of 173 degrees. All measurements were made at temperature of 35°C, viscosity of 0.8872 cP, refractive index of 1.330, equilibration time of 120 s and path length of 1 cm.

2.4.3 Amino Acid Permeation Through A Lipid Bilayer

100 μL of vesicle suspension was mixed with 300 μL of 10 mM tryptophan in the appropriate buffer (described previously) for various amounts of time maintained at 27°C. The time was in the range of minutes (5, 10, 15, 30 45 and 60 min) and hours (2, 3, 5, 7, 8, 12 and 24 hrs). At each time point, the mixture was immediately passed through a

PD-10 desalting column (GE Healthcare) containing 8.3 mL of Sephadex G-25 medium previously equilibrated with the same buffer. Small molecules such as free tryptophan that had not diffused into the bilayer were trapped within the pores of the column, while the large vesicles were eluted out and collected in a vial. Fluorescence measurements of tryptophan associated with these vesicles were made with a Synergy H4 Fluorimeter set to an excitation wavelength of 280 nm and emission wavelength of 348 nm.

Rate constant and permeability coefficient calculation

The kinetics of tryptophan permeation into the vesicle bilayer were determined by fitting the change in fluorescence over length of time to equation 1:[32,33]

$$\left[F(t)\right]_i = \left[F(eq)\right]_i \left(1 - e^{-kt}\right) \qquad (2\text{-}1)$$

where $\left[F(t)\right]_i$ is the fluorescence from amino acids inside the vesicles at time *t*, $\left[F(eq)\right]_i$ is the fluorescence from amino acids at equilibrium inside vesicles at $t = \infty$, and *k* is the permeation rate constant. The permeability coefficient (P) under different pH conditions requires more elaborate analysis and assumptions motivated by (current) experimental and computational observables. We therefore will discuss the calculation of P in the results discussion section.

2.4.4 Molecular Dynamics Simulation

In all simulations performed by Dr. Ron Elber and Dr. Alfredo Cardeñas, the periodic box contains a total of 40 DOPC molecules (20 in each leaflet), 1542 water

molecules, and 1 or 2 tryptophan molecules. For the charged tryptophan species (positively or negatively charged amino group or the zwitterionic molecule), only one permeant was added in the simulation box. For the uncharged neutral species, two tryptophan molecules were added in the box, one in each leaflet making sure that the separation of their center of masses was always greater than 32 Å. When needed, an additional counterion (chloride or sodium ions) was added to the aqueous solution to keep the electroneutrality of the simulation box. The simulations were performed at a constant temperature of 300 K and constant volume. The cell size is $37 \times 37 \times 75$ Å^3 with the z axis (perpendicular to the membrane surface) corresponding to the largest side. The area per lipid is 68.5 Å^2 , close to the reported experimental value of 72.1 Å^2 for DOPC membrane bilayers.[20] All of the permeants were modeled with the OPLS united-atom force field,[21] and a combination of Berger/OPLS parameters was used for the lipid molecules.[22] The SPC model was used to represent the water molecules.[23] We applied periodic boundary in the three spatial directions. The long-range electrostatics interactions were computed with the smooth particle mesh Ewald method[24] with $32 \times 32 \times 64$ cubic grids. The cutoff for the real component of the electrostatic potential and the van der Waals interactions was set to 9.0 Å. We used a matrix implementation of SHAKE to constrain water bond lengths and angles.[25,26] We employed rRESPA24 to integrate the equations of motion with a short time step of 1 fs to evaluate the covalent, van der Waals, and real component of the electrostatics interactions, and a longer time step of 4 fs to estimate the reciprocal space component of the Ewald sum.[27] The initial configurations were taken from previously performed simulations of a terminally blocked

tryptophan (NATA) permeation through a bilayer membrane of DOPC molecules.[28] In the current simulation, the NATA molecule was replaced for any of the four different tryptophan species considered here. After an initial 500 ps equilibration period, production jobs of 50 ns were launched in each of the umbrella windows considered. We used a harmonic potential to constrain the position of the center of mass of the permeants on 33 windows along the membrane axis (z axis). The separation between consecutive windows was 2 Å, and the harmonic force constant applied was of 7 kcal/mol. For windows closer to the membrane center (4 Å away from the center), the simulations of the charged tryptophan species were extended to 90 ns to improve the convergence of the structural results at those membrane depths. Convergence was assessed by comparison of the results of independent simulations for the two membrane layers. We use the z-constraint method[29,30] to obtain the potential of mean force and permeability estimates for membrane permeation of the different tryptophan moieties. We further evaluate the sampling using ergodic measures we have employed in the past.[31,32]

2.5 REFERENCES

1. Elber, R.; Roitberg, A.; Simmerling, C.; Goldstein, R.; Li, H. Y.; Verkhivker, G.; Keasar, C.; Zhang, J.; Ulitsky, A. Moil a program for simulations of macromolecules. *Comput. Phys. Commun.* **1995**, *91*, 159-189.
2. Ruymgaart, A.P.; Cardenas, A. E.; Elber, R. MOIL-opt: Energy-Conserving Molecular Dynamics on a GPU/CPU System. *J. Chem. Theory Comput.* **2011**, *7*, 3072–3082.
3. Berger, O.; Edholm, O.; Jähnig, F. Molecular dynamics simulations of a fluid bilayer of dipalmitoylphosphatidylcholine at full hydration, constant pressure, and constant temperature. *Biophys. J.* **1997**, *72*, 2002-2013.
4. Jorgensen, W. L.; Tiradorives, J. The OPLS Potential Functions for Proteins. Energy Minimization for Crystals of Cyclic Peptides and Crambin. *J. Am. Chem. Soc.* **1988**, *110*, 1657-1666.
5. Jo, S.; Kim, T.; Iyer, V. G.; Im, W. CHARMM-GUI: A web-based graphical user interface for CHARMM. *J. Comput. Chem.* **2008**, *29*, 1859-1865.
6. Jo, S.; Lim, J. B.; Klauda, J. B.; Im, W. CHARMM-GUI Membrane Builder for Mixed Bilayers and Its Application to Yeast Membranes. *Biophys. J.* **2009**, *97*, 50-58.
7. Jorgensen, W. L.; Chandrasekhar, J.; Madura, J. D.; Impey, R. W.; Klein, M. L. Comparison of simple potential functions for simulating liquid water. *J. Chem. Phys.* **1983**, *79*, 926-935.

8. Hu, W.; Webb, L. J. Direct Measurement of the Membrane Dipole Field in Bicelles Using Vibrational Stark Effect Spectroscopy. *J. Phys. Chem. Lett.* **2011**, *2*, 1925-1930.
9. Essmann, U.; Perera, L.; Berkowitz, M. L; Darden, T.; Lee, H.; Pedersen, L. G. A smooth particle mesh Ewald method. *J. Chem. Phys.* **1995**, *103*, 8577-8593.
10. Weinbach, Y.; Elber, R. Revisiting and parallelizing SHAKE. *J. Comput. Phys.* **2005**, *209*, 193-206.
11. Ryckaert, J. P.; Ciccotti, G.; Berendsen, H. J. C Numerical integration of the cartesian equations of motion of a system with constraints: molecular dynamics of n-alkanes. *J. Comput. Phys.* **1977**, *23*, 327-341.
12. Tuckerman, M.; Berne, B. J.; Martyna, G. J. Reversible multiple time scale molecular dynamics. *J. Chem. Phys.* **1992**, *97*, 1990-2001.
13. Patra, M.; Karttunen, M.; Hyvonet, M.T.; Falck, E.; Lindqvist, P.; Vattulainen, I. Molecular dynamics simulations of lipid bilayers: Major artifacts due to truncating electrostatics interactions. *Biophys. J.* **2003**, *84*, 3636-3645.
14. Morrissey, J. H. *Morrisey Lab Protocol for Preparing Phospholipid Vesicles (SUV) by Sonication*. Trigger Website. http://tf7.org/suv.pdf (accessed March 15, 2012).
15. Pasenkiewicz-Gierula, M.; Rog, T.; Kitamura, K.; Kusumi, A. Cholesterol effects on the phosphatidylcholine bilayer polar region: A molecular simulation study. *Biophys. J.* **2000**, *78*, 1376-1389

16. Price, M. L. P.; Ostrovsky, D.; Jorgensen, W. L. Gas-phase and liquid-state properties of esters, nitriles, and nitro compounds with the OPLS-AA force field. *J. Comput. Chem.* **2001**, *22*, 1340-1352
17. Berendsen, H. J. C.; Grigera, J. R.; Straatsma, T. P. THE MISSING TERM IN EFFECTIVE PAIR POTENTIALS. *J. Phys. Chem.* **1987**, *91*, 6269-6271
18. Di Pierro, M.; Elber, R.; Leimkuhler, B. A Stochastic Algorithm for the Isobaric-Isothermal Ensemble with Ewald Summations for All Long Range Forces. *J Chem Theory Comput* **2015**, *11*, 5624-5637
19. Egberts, E.; Berendsen, H. J. C. Molecular-Dynamics Simulation of a Smectic Liquid-Crystal with Atomic Detail. *J. Chem. Phys.* **1988**, *89*, 3718-3732
20. Liu, Y. F.; Nagle, J. F. Diffuse Scattering Provides Material Parameters and Electron Density Profiles of Biomembranes. *Phys. Rev. E* **2004**, *69*, 040901-1−040901-4.
21. Jorgensen, W. L.; Tiradorives, J. The Opls Potential Functions for Proteins - Energy Minimizations for Crystals of Cyclic-Peptides and Crambin. *J. Am. Chem. Soc.* **1988**, *110*, 1657−1666.
22. Berger, O.; Edholm, O.; Jahnig, F. Molecular Dynamics Simulations of a Fluid Bilayer of Dipalmitoylphosphatidylcholine at Full Hydration, Constant Pressure, and Constant Temperature. *Biophys. J.* **1997**, *72*, 2002−2013.
23. Berendsen, H. J. C.; Grigera, J. R.; Straatsma, T. P. The Missing Term in Effective Pair Potentials. *J. Phys. Chem.* **1987**, *91*, 6269−6271.

24. Essmann, U.; Perera, L.; Berkowitz, M. L.; Darden, T.; Lee, H.; Pedersen, L. G.; Smooth, A. Particle Mesh Ewald Method. *J. Chem. Phys*. **1995**, *103*, 8577−8593.

25. Weinbach, Y.; Elber, R. Revisiting and Parallelizing Shake. *J. Comput. Phys.* **2005**, *209*, 193−206.

26. Ryckaert, J. P.; Ciccotti, G.; Berendsen, H. J. C. Numerical Integration of Cartesian Equations of M Otion of a System with Constraints - Molecular Dynamics of N-Alkanes. *J. Comput. Phys*. **1977**, *23*, 327−341.

27. Tuckerman, M.; Berne, B. J.; Martyna, G. J. Reversible Multiple Time Scale Molecular-Dynamics. *J. Chem. Phys.* **1992**, *97*, 1990−2001.

28. Cardenas, A. E.; Jas, G. S.; DeLeon, K. Y.; Hegefeld, W. A.; Kuczera, K.; Elber, R. Unassisted Transport of N-Acetyl-LTryptophanamide through Membrane: Experiment and Simulation of Kinetics. *J. Phys. Chem. B* **2012**, *116*, 2739−2750.

29. Marrink, S. J.; Berendsen, H. J. C. Simulation of Water Transport through a Lipid-Membrane. *J. Phys. Chem.* **1994,** *98*, 4155− 4168.

30. Marrink, S. J.; Berendsen, H. J. C. Permeation Process of Small Molecules across Lipid Membranes Studied by Molecular Dynamics Simulations. *J. Phys. Chem.* **1996**, *100*, 16729−16738.

31. Kirmizialtin, S.; Elber, R. Computational Exploration of Mobile Ion Distributions around Rna Duplex. *J. Phys. Chem. B* **2010**, *114*, 8207−8220.

32. Straub, J. E.; Thirumalai, D. Exploring the Energy Landscape in Proteins. *Proc. Natl. Acad. Sci. U.S.A.* **1993**, *90*, 809−813.

Chapter 3 Model Membranes

3.1 VESICLES AS MODEL MEMBRANES

Vesicles are self-closed, spherical aqueous dispersions of phospholipids where one or more of the bilayers entrap solvent.[1,2] The characteristic topology of vesicles, where a relatively impermeable lipid bilayer completely encapsulates an aqueous inside and their ability to entrap various solutes in the aqueous phase during formation, make vesicles extremely attractive model membranes in studying immune therapies and drug delivery systems.[2] Hydrophobic compounds interact with the hydrophobic interior of the bilayer whereas hydrophilic compounds are attracted to the charged head groups, absorbed on the surface, or entrapped in the aqueous compartments. In 1978, a New York Academy of Sciences meeting on "Liposomes and Their Uses in Biology and Sciences" categorized vesicles into three classes based on their size and lamellarity and are referred to by three letter acronyms.[1] Multilamellar vesicles or MLVs are vesicles composed of two or more spheres of lipid bilayers enclosed within.[1] Unilamellar vesicles under 100 nm are termed as small unilamellar vesicles or SUVs where as spheres larger than 100 nm are classified as large unilamellar vesicles or LUVs.[1] A schematic representation of different kinds of vesicles is presented in Figure 3.1-1. The vesicle size and its lamellae depend on the preparation technique.[1,2] For example, swelling of the dry phospholipid film in an aqueous solvent forms MLVs and single lamellar vesicles are prepared from MLVs suspension either by sonication or by extruding them multiple times through a porous membrane of different sizes. The sonication technique makes a dispersion of

small unilamellar vesicles whereas the extrusion technique prepares more homogenous distribution of LUVs of a specific size. In our studies, we make use of unilamellar vesicles of both SUVs and LUVs, composed of two kinds of phospholipids: 1,2-dimyristoyl-*sn*-glycero-3-phosphocholine (DMPC) and 1,2–dioleoyl-sn-glycerol-3-phosphocholine (DOPC). This particular class of phospholipids consists of a zwitterionic phosphocholine head group with a positively charged choline group and a negatively charged phosphate group, two glycerol backbones, *sn*-1 and *sn*-2, attached to saturated alkyl tails as shown in Figure 1.1-1. The phospholipids form smectic mesophases that undergo a characteristic gel-liquid crystalline phase transition above the transition temperature, T_m .[1] The transition temperature, also called the melting temperature depends on the length and saturation of acyl chain lengths. The T_m of phospholipids composed of the same acyl chain at both positions increases by 14-17 °C for every additional two-methylene units, whereas incorporation of a double bond, branched chains or a bulky groups such as cyclopropane lowers T_m by a considerable amount. At temperatures below T_m, vesicles are considered to be solid; when above T_m, they are considered to be fluid. DMPC has a transition temperature of 23 °C and DOPC has a transition temperature of 42 °C.[1] In our studies, all vesicle samples were prepared and used at temperatures above T_m for ease and stability.

3.2 CHARACTERIZATION OF VESICLES

We characterized lipid vesicles using ^{31}P nuclear magnetic resonance (NMR) spectroscopy, dynamic light scattering and atomic force microscopy.

3.2.1 ^{31}P NMR Spectroscopy

The spectral line shape of the NMR spectrum provides qualitative information on the size of vesicles. A "wide-line" or powder-line shape due to the restricted anisotropic motion is indicative of multilamellar vesicles, whereas a single narrow peak is representative of unilamellar vesicles.[4-6] Figure 3.2a and Figure 3.2b shows representative ^{31}P NMR spectra obtained for (a) vesicles composed of 30 mM DMPC lipids only, (b) 30 mM DMPC lipids plus 2 mM of peptides, respectively. In both cases, we obtained a single narrow peak confirming the presence of unilamellar vesicles. We can further affirm the single lamellarity of the vesicles by measuring the ratio between the number of lipid molecules on the outer surface to the inner surface. For micellar structure, all phospholipids face the bulk solution.[4-6] In MLVs, only a small fraction of phospholipids face the outer bulk solution and the ratio of the phospholipids in the outer lamellar to the inner lamellar is much smaller than 1.[4-6] And in unilamellar vesicles, the ratio is usually between 1 and 2.2 and tends to decrease with larger vesicles.[4-6] We measured this ratio by recording ^{31}P NMR spectra of vesicles after adding external shift reagents. Paramagnetic ions such as Pr^{3+} have very short electron relaxation times and upon interaction with the phosphate ions in the lipid head group, perturb the nuclear spin relaxation times and cause a chemical shift downfield. Because lipid bilayers are impermeable to lanthanide cations, Pr^{3+} only shifts the signal from the outer monolayer, splitting the single narrow peak into two.[4-6] In Figure 3.2c, we show ^{31}P NMR spectrum obtained for 30mM DMPC lipids plus 2 mM of peptides and 0.5 mol% of $PrCl_3 \cdot H_2O$. Compared to Figure 3.2b, the spectrum has two split peaks and the ratio of area of the

shifted peak to the un-shifted peak is 2 indicating that the vesicles are indeed unilamellar and smaller in size.

3.2.2 Dynamic Light Scattering

Particle size analysis was done using dynamic light scattering technique. Dynamic light scattering (DLS), sometimes referred to as Quasi-Elastic Light Scattering (QELS), is a non-invasive, well-established technique for measuring the size distribution of molecules and particles typically in the submicron to nanometer length scale range. Typical applications of DLS are the characterization of particles, emulsions or molecules, which have been dispersed or dissolved in a liquid. The Brownian motion of particles or molecules in suspension causes laser light to be scattered at different intensities. In DLS, we measure the time-dependent fluctuations in the intensity of scattered light due to the diffusive motion of the particle. Analysis of these intensity fluctuations yields the velocity of the Brownian motion and hence the particle size using the Stokes-Einstein relationship given by

$$D_h = \frac{k_B T}{3\pi\eta D_t} \qquad (3\text{-}1)$$

where D_h is the hydrodynamic diameter or the particle size, D_t is the translational diffusion coefficient, k_β is Boltzmann's constant, T is thermodynamic temperature and η is dynamic viscosity.

We ran DLS measurements to get a size distribution of our vesicles prepared with the sonication method. We measured the average hydrodynamic diameter of the vesicles suspension to be 59 ± 8 nm, verifying that the vesicles were indeed small unilamellar vesicles.

3.2.3 Atomic Force Microscopy

The size distribution is further confirmed by images taken with Agilent 5500 Atomic Force Microscope. AFM is a high resolution imaging technique that works by bringing the cantilever tip in contact with the surface of interest. An ionic repulsive force from the surface applied to the tip bends the cantilever upwards. The amount of bending, measured by a laser spot reflected on to a split photo detector, can be used to calculate the force. By keeping the force constant while moving the tip across the surface, the vertical movement of the tip follows the surface profile and is recorded as the surface topography by the AFM.

Figure 3.3a and Figure 3.3b show the amplitude and phase images of 30 mM DMPC vesicles prepared with 1 mM of αLAX(23) deposited on a freshly cleaved mica surface and air dried for 2 hours with 400 nm and 100 nm resolution respectively. According to a paper by a Xue-Feng and group at Wuhan University, China, the initially absorbed vesicles disrupture and form a flat bilayer membrane on the surface and the intact vesicles are then stably adsorbed on the bilayer surface.[7] The round shapes in Figure 3.3a and Figure 3.3b are representative of intact vesicles and measure about 50 nm

in size correlating with the size distribution obtained from DLS measurement. The images also show a homogeneous distribution of uniform size vesicles.

3.2.4 Conclusion

In conclusion, we demonstrated that we prepared small unilamellar vesicles using the sonication method. We successfully characterized vesicle size and lamellarity using DLS, NMR and AFM.

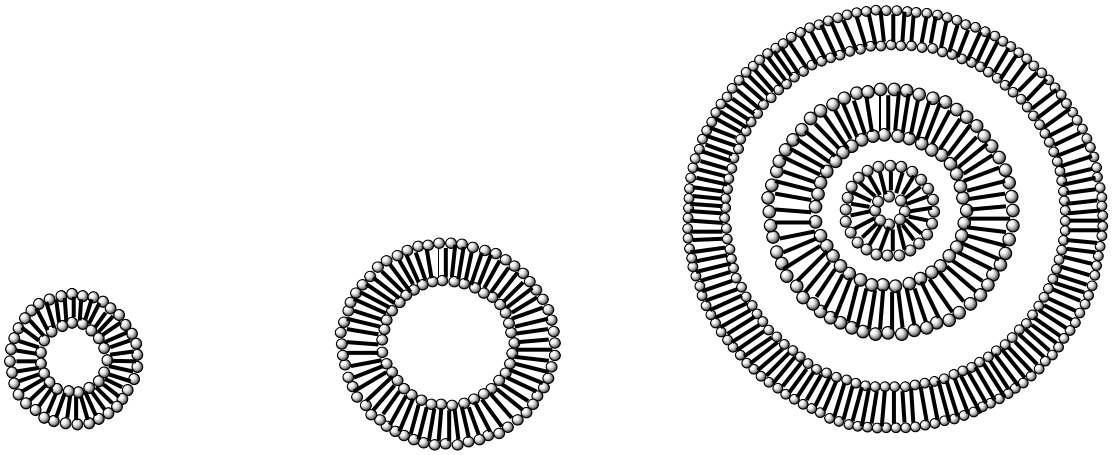

Small Unilamellar Vesicle (SUV) < 100 nm

Large Unilamellar Vesicle (LUV) 100-1000 nm

Multilamellar Vesicle (MLV) micron in size

Figure 3.1: Different classes of vesicles based on their size and lamellarity. Small unilamellar vesicles (SUV) are less than 100 nm in diameter, large unilamellar vesicles (LUV) are between 100 and 1000 nm in diameter and multilamellar vesicles are micron in size and have more than one lipid bilayer.

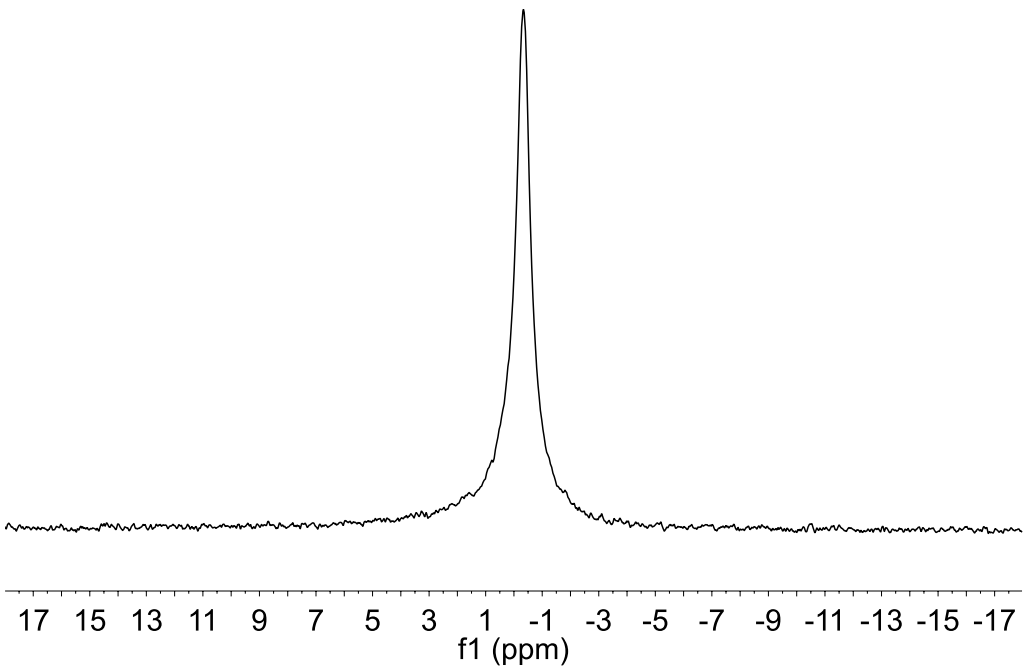

(a)

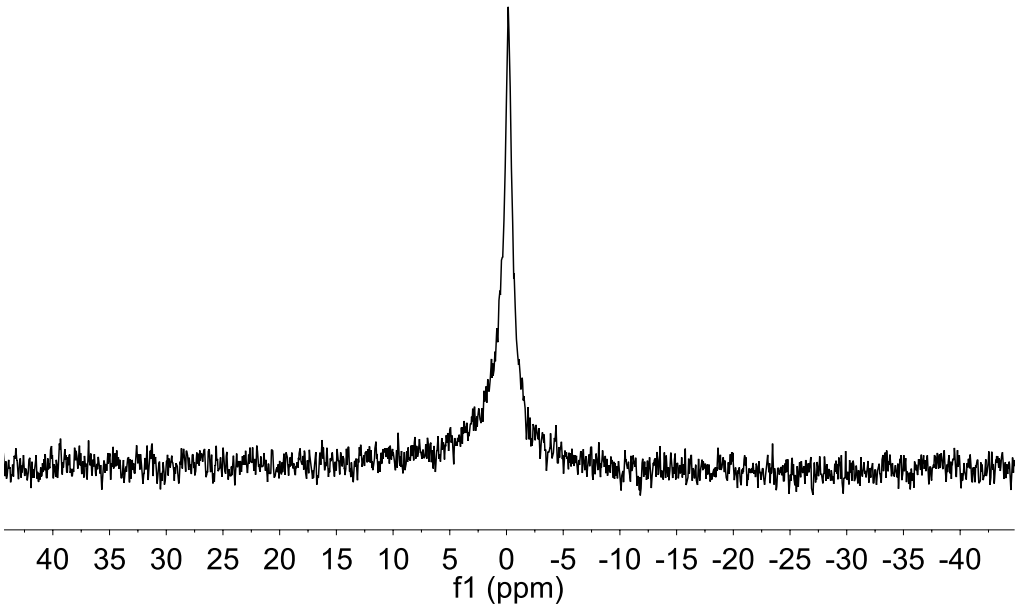

(b)

Figure 3.2 continued on next page.

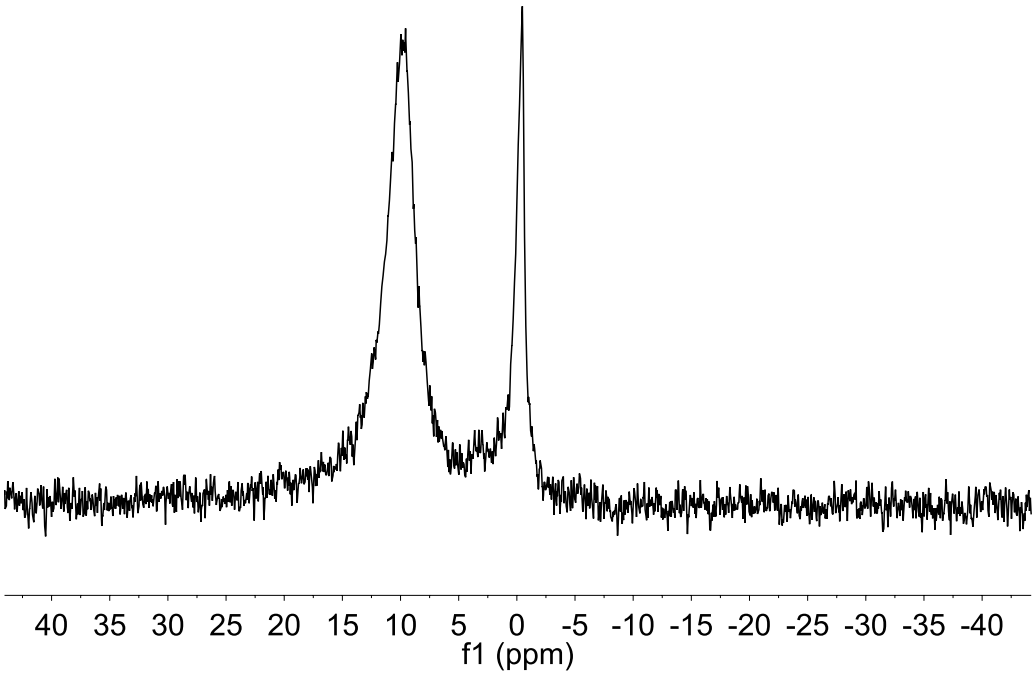

(c)

Figure 3.2: ^{31}P-NMR spectra for DMPC vesicles prepared with 30 mM DMPC lipids (a) vesicle only (b) vesicles with 2 mM peptide and (c) vesicles with 2 mM peptide and Pr^{3+}. The single sharp peak in (a) and (b) is representative of small unilamellar vesicles. Addition of lanthanide ions shifts the phosphorus peak from the phospholipids on the outer layer splitting a single narrow peak in (a) and (b) into two as shown in (c).

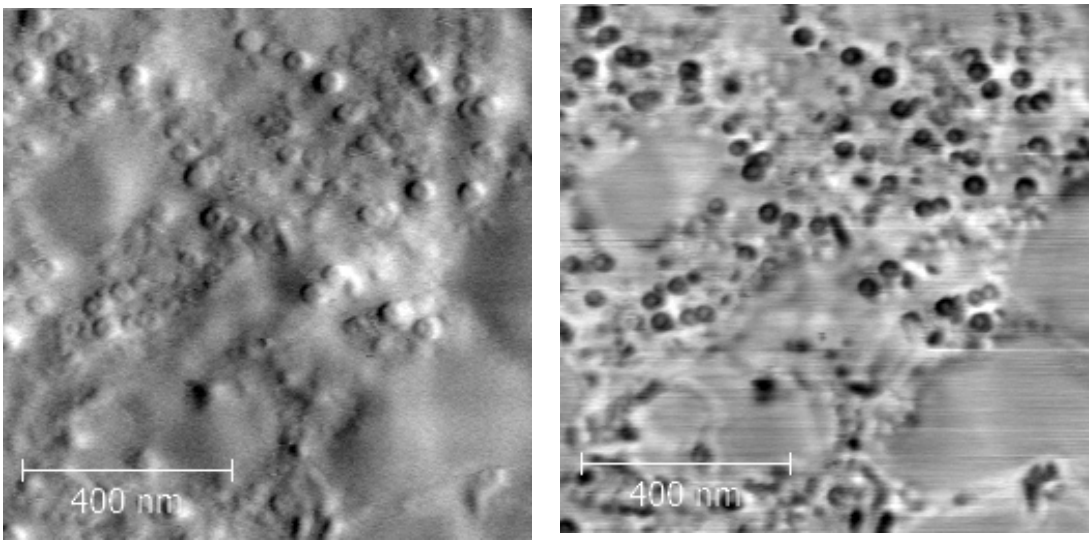

Figure 3.3: AFM amplitude image (on the left) and phase image (on the right) taken on 30 mM DMPC vesicles intercalated with 1 mM αLAX(23) deposited on a freshly cleaved mica surface and air dried. The images were taken using an Asylum MFP-3D Stand Alone AFM operating in tapping-mode and flattened and processed on a Gwyddion software.

3.3 REFERENCES

1. Szoka, F. Jr.; Papahadjopoulos, D. Comparative Properties and Methods of Preparation of Lipid Vesicles (Liposomes). *Ann. Rev. Biophys. Bioeng.* **1980**, *9*, 467-508.
2. Huang, C. Studies on Phosphatidylcholine Vesicles. Formation and Physical Characteristics. *Biochem.* **1969**, *8 (1),* 344-352.
3. Kumar, V. V.; Baumann, W. J. Bilayer Asymmetry in Lysophosphatidylcholine/Cholesterol (1:1) Vesicles. A Phosphorus-31 NMR Study. *Biochemical and Biophysical Research Communications* **1986**, *139*, 25-30.
4. Fenske, D. B. Structural and Motional Properties of Vesicles as revealed by Nuclear Magnetic Resonance. *Chem. Phys. Lipids.* **1993**, *64*, 143-16219.
5. Bystrov, V. F.; Shapiro, Y. E.; Viktorov, A. V.; Barsukov, L. I.; Bergelson, L. D. ^{31}P-NMR signals from inner and outer surfaces of phospholipid membranes. *FEBS Lett.* **1972,** *25*, 337-338
6. Fröhlich, M.; Brecht, V.; Peschka-Süss, R. Parameters Influencing the Determination of Liposome Lamellarity by ^{31}P-NMR. *Chemistry and Physics of Lipids*. **2001**, *109*, 103-112.
7. Xue-Feng, L.; Gao-Yong, Z.; Jin-Feng, Dong.; Xiao-Hai, Z.; Xin-Lin, H. An Atomic Force Microscopy Study on Small Unilamellar Vesicle Structures on Mica. *Chin. J. Chem*. **2006**, *24*, 311-315.
8. Teschke, O.; de Souza, E. F. Liposome Structure Imaging by Atomic Force Microscopy: Verification of Improved Liposome Stability during Adsorption of

Multiple Aggregate. *Langmuir* **2002**, *18*, 6513-6520.

Chapter 4 Direct Measurement of Membrane Dipole Field Using Vibrational Stark Effect Spectroscopy Coupled with Molecular Dynamics Simulation

The author's contribution to this publication[1] is the collection of experimental data and writing the manuscript.

4.1 INCORPORATION OF NITRILES PROBE INSIDE THE VESICLES

In this research, we directly measured the dipole electrostatic field spanning from the membrane-water interface into the middle of hydrocarbon interior of the lipid bilayer using vibrational Stark effect spectroscopy of a nitrile vibrational chromophore placed at various locations inside the bilayer. We incorporated the nitrile probe in the bilayer interior of small unilamellar vesicles (SUVs) composed of DMPC phospholipids by inserting an α-helical transmembrane peptide containing an unnatural amino acid, *p*-cyanophenylalanine (*p*-CN-Phe). The α-helical transmembrane helix was composed of the polypeptide sequence, HHGGPGLA*m*L*n*XGPGGHH where $m + n = 18$, and X is the *p*-cyanophenylalanine. The repeating leucine and alanine motifs make an alpha helix structure with a helix length of 28.5 Å, GGPG sequence anchors the peptide at the lipid head group region and ensures it orients parallel to the bilayer normal, and the two histidine amino acids at both ends make the peptide soluble in the aqueous region. We systematically

[1] Shrestha, R.; Cardenas, A. E.; Elber, R.; Webb, L. J. Measurement of the Membrane Dipole Electric Field in DMPC Vesicles Using Vibrational Shifts of p-Cyanophenylalanine and Molecular Dynamics Simulations. *J. Phys. Chem. B* **2015**, *119*, 2869-2876

moved the unnatural amino acid along the polypeptide sequence to probe different regions across the bilayer normal, starting from the water-membrane interface to the hydrophobic bulk interior. The amino acid sequences for the four peptides used in our experiments are provided in Table 4.1. The positions of the nitrile probes were chosen in correspondence with the depth of a bilayer moving from the C- to N-terminus of the peptide such that αLAX(25) probed the lipid−water interface, αLAX(16) probed the hydrophobic interior, and αLAX(23) and αLAX(21) were intermediate between these two extreme positions as shown in Figure 4.1. As we changed the location of the nitrile probe inside the membrane, we also changed the local electrostatic environment that the probe was exposed to, as a result, we observed shift in the absorption energy of the nitrile-stretching mode as a function of its local environment.

4.2 CIRCULAR DICHROISM SPECTROSCOPY

We characterize the secondary structure and the orientation of the helical peptides in our vesicles using circular dichroic (CD) spectroscopy and extensive molecular dynamics simulation of our peptide-vesicle bilayer. According to Table 4.1, all four polypeptides were mostly comprised of leucine and alanine in the core of the peptide backbone, which make them extremely hydrophobic and insoluble in buffer. They are soluble only in hydrophobic solvents such as TFE or when incorporated into the lipid bilayer. Figure 4.2 shows representative CD spectra for all four peptides described in Table 4.1 incorporated inside vesicles (in blue) and, as a control, when dissolved in

hydrophobic TFE solvent (in black). When dissolved in TFE, all four peptides showed strong α-helical characteristics with two minima at 208 and 222 nm and a high maximum at 195 nm.[4] CD spectra were nearly superimposable for all peptide sequences and changing the position of the unnatural amino acid along the polypeptide chain did not affect the secondary structure of the helix. Upon intercalation into the lipid bilayer of DMPC vesicles, the peptides maintained the double trough characteristics at 208 and 220 nm, and therefore their helical secondary structure as shown in blue in Figure 4.2. However, there was a slight decline in the magnitude of the spectral intensity obtained for peptides intercalated in the vesicles compared to the control solutions, likely caused by the increased turbidity of the vesicle solution.[5] In summary, the spectra in Figure 4.2 demonstrate that these peptide sequences exhibit strong α-helical characteristics when intercalated into our DMPC vesicles, as expected.

4.3 Molecular Dynamics Simulation

While CD spectra clearly confirm stable helical secondary structure for each peptide studied here, they do not provide any information on the local orientation of that helix within the membrane. When each peptide folds into its energy minimized helical structure, the length of the hydrophobic repeating leucine and alanine motif is 28.5 Å.[3] which is a few angstroms greater than the hydrophobic thickness of a DMPC bilayer, ~26 Å, calculated based on the length of adjacent hydrocarbon tails.[6,7] The hydrophobic mismatch between the hydrophobic bilayer thickness and the hydrophobic stretch of the helix predicts that the helix will tilt within the membrane to ensure stable transmembrane

insertion and avoid distortion of the lipid bilayer but does enable a distribution of the orientation of the nitrile bond vector within the membrane.[8] It is possible to estimate a tilt angle of 24.1° by simple geometric calculation of minimum difference in the hydrophobic length of the peptide versus the membrane. However, this would not provide any information on the range of stable conformations that would be expected during a steady-state experiment. Hence, in order to gain atomistic detail on the orientation of the helix inside the bilayer and the local environment around the nitrile probe itself, our collaborators, Dr. Ron Elber and Dr. Alfredo Cardeñas, performed extensive molecular dynamics simulation on the two peptides containing the outer- and innermost placed nitrile groups, αLAX(25) and αLAX(16), respectively, embedded in a slab of DMPC lipids representing the bilayer. Figure 4.3 shows representative snapshots of both peptides surrounded by DMPC lipids and explicit water molecules.

The α-helical secondary structure of both of the transmembrane peptides remained intact for the entire simulation period of 100 ns for αLAX(16) and 200 ns for αLAX(25), as expected from the steady-state CD spectroscopy. Both peptides were initially inserted vertically into the bilayer (i.e., helical axis parallel to the bilayer normal) but in both cases, a slight tilting of the helical backbone of the peptide was soon observed in the trajectories. We quantified the magnitude of this tilt by measuring the angle of the helical axis (defined by a line through the center of the peptide backbone stretching from Cα of histidine residues at both termini of the peptide) with respect to the membrane normal for every snapshot collected in our 100−200 ns simulations. Figure 4.4 shows the normalized histogram of the tilt angle of αLAX(25) (black) and αLAX(16) (red), with

respect to the bilayer normal calculated over the course of the simulation. Both peptides show a distribution of tilt angles at slightly different average values: 21 ± 7° for αLAX(25) and 25 ± 4° for αLAX(16). The estimated tilt angle of 24.1° obtained from a simple calculation for geometric model described earlier falls within the range of angles obtained from the simulation of both peptides. In addition to fairly accurate representation of helix orientation in the membrane, the MD simulations also provide a distribution width (i.e., standard deviation) for this important property.

Along with perturbations in helix tilt, the position of the nitrile probe along the bilayer normal was also affected by rotation of the side chain about the χ1 torsion angle (defined by N−Cα−Cβ−Cγ), and therefore fluctuated greatly. Because the angle of the nitrile with respect to the membrane normal is the relevant physical quantity in determining the electric field measured through VSE, we determined this angle for every snapshot obtained in our simulations. Figure 4.5 shows the normalized histogram of the angle the nitrile bond makes with respect to the membrane normal for both probe locations, αLAX(25) (black) and αLAX(16) (red). For αLAX(25), the nitrile angle exhibits a bimodal distribution and shows a heterogeneous population of at least two stable conformations, whereas the nitrile attached to αLAX(16) has a homogeneous distribution of the angle relative to αLAX(25). To determine the cause of this observation, we investigated individual representative snapshots of each peptide. In the case of αLAX(25), the vibrational probe remained fixed at an angle of ~67° for the first 50 ns of the simulation, and then abruptly switched its position to 122° and stayed there for the rest of the 150 ns simulation period. Upon further inspection, structures observed

during the first 50 ns of the simulation appeared to be perturbed, with the hydrophobic CN-Phe side chain pointed towards the membrane−water interface interacting closely with the zwitterionic headgroup of the lipid and TIP3P water. When the angle switched to 122°, the CN-Phe side chain was now completely immersed in the hydrophobic membrane interior, and remained within a small range of angles around this value. We therefore used the equilibrated conformations from the last 150 ns of simulation data to estimate the nitrile angle. This gave a value of 122 ± 15°. In the case of αLAX(16), the nitrile molecule remained relatively stable at 110° with occasional perturbations to angles as large as 140°, i.e., approaching an orientation perpendicular to the plane of the membrane. These observations are consistent with the different environments in which the nitriles are placed by virtue of their different amino acid sequences. Because of its position near the center of the lipid bilayer, the nitrile probe on αLAX(16) was located in a low dielectric hydrocarbon membrane interior and experienced essentially identical intermolecular interactions no matter how it was oriented about the helical axis. This resulted in a nitrile orientation that remained relatively fixed at 110° with occasional excursions to other stable conformations. We determined an average nitrile angle of 112 ± 23° for the nitrile probe on the peptide αLAX(16). The larger distribution of observed angles at this position was due to the more homogeneous hydrophobic environment found at the core of the lipid bilayer membrane, with a smaller penalty for orientation sampling of the CN-Phe side chain around the χ1 torsion angle.

4.4 FOURIER- TRANSFORM INFRARED SPECTROSCOPY

Figure 4.6 shows representative normalized vibrational absorption spectra of the nitrile probes on peptides, αLAX(25) (black), αLAX(23) (blue), αLAX(21) (green), and αLAX(16) (red) intercalated into DMPC vesicles at 0.5 mM concentration. As we move the nitrile probe deeper into the membrane, we see shift in its absorption energy from 2228.18 ± 0.07 cm^{-1} at αLAX(25) to 2231.05 ± 0.02 cm^{-1} in αLAX(16). In Table 4.2, we report the average absorption peak frequencies and full width at half-maximum (FWHM) of nitrile stretching band at all four peptide locations, αLAX(25), αLAX(23), αLAX(21) and αLAX(16) incorporated into vesicles at concentrations of 0.5 and 1 mM peptides, along with their associated standard deviation from at least three experimental replicates. For all four peptides, the mean peak frequencies for the nitrile absorption band are red shifted relative to the nitrile absorption frequency measured for *p*-CN-Phe dissolved in water (2237.5 cm^{-1}).[9] This indicates that the nitrile molecule attached to all four peptides is localized in a hydrophobic environment compared to a well-solvated buffer. This provides additional experimental evidence that both the molecular model and the MD sampling are accurately describing the position of the nitrile within the bilayer interior. We know from our peptide design and MD simulation that the nitrile at position 25 is near the hydrophilic membrane water interface and nitrile at position 16 is located in the lipid tail region. The nitrile is exposed to two significantly different electrostatic environments at these positions. As a result, we see a Stark shift of +2.9 cm^{-1} and +2.6 cm^{-1} in moving from position 25 to position 16 for 0.5 mM and 1 mM peptide,

respectively. With these measured values of $\Delta\nu_{obs}$, 0.67 cm^{-1} /(MV/cm) for the Stark tuning rate of nitrile,[3] and an angle of 122 ± 15° between the nitrile bond and bilayer normal computed for αLAX(25) in Equation 1-1, we calculated the magnitude of the dipole electric field to be 8.1 ± 4 MV/cm for 0.5 mM peptide and 7.3 ± 3 MV/cm for 1 mM peptide. We also calculated the absolute field values based on αLAX(16)'s nitrile-membrane normal angle of 112 ± 23°, and the results are 11.4 ± 11 MV/cm and 10.3 ± 10 MV/cm for 0.5 and 1 mM peptide, respectively. For position of the nitrile, the average magnitudes of the calculated dipole field fall within the error range of each other and are larger than the dipole field value of –6 MV/cm determined previously for lipid bicelles.[3] The large error of 3 and 11 MV/cm associated with the average dipole field represents the distribution of the dipole field values which are determined based on the distribution of the nitrile orientation obtained from molecular dynamics simulation studies.

In a steady-state FTIR experiment such as those described here, the line width of the absorption peak can be used to assess the homogeneity of the local molecular environment surrounding an oscillator.[3,9,10,11] For example, Gai and co-workers[9,11] have shown that the nitrile stretching vibration in *p*-CN-Phe has a wider spectrum in polar solvents like water compared to apolar solvents like THF because of a greater number of microenvironments around the nitrile as it forms hydrogen bonds with water. The data in Table 4.2 clearly show that the full width at half maximum (FWHM) of nitrile's vibrational peak systematically decreased as the probe was moved deeper into the membrane (i.e., from αLAX(25) to αLAX(16)). In bilayers containing 0.5 mM peptide, the FWHM of nitrile absorption peak decreased by 1.7 cm^{-1} between αLAX(25) to

αLAX(16) and in bilayers containing 1 mM peptide, the FWHM narrowed by 0.8 cm^{-1}. This translocation moves the nitrile probe from the heterogeneous lipid–solution interface containing water, buffer ions, the zwitterionic headgroup, and the acyl linkage to the fatty acid chain, all near position 25, into a significantly more homogeneous environment dominated by the hydrocarbon tail of the lipid at position 16. To investigate the role of the electric field in this result, we calculated the absolute value of the electric field experienced by the Cα of *p*-CN-Phe on αLAX(25) and αLAX(16) for every snapshot in our MD trajectories. The normalized distributions of fields calculated on both positions are shown in Figure 4.7, where the distributions for αLAX(25) and αLAX(16) are shown in black and red, respectively. When the nitrile is near the middle of the membrane, small changes in the structure of the system do not result in large differences in the immediate chemical environment around the nitrile, since it is fully immersed in the middle of the bilayer. At position 16, even if the nitrile experiences large conformational changes relative to the helical backbone, because it is in the interior of the membrane, it will experience a constant hydrophobic hydrocarbon environment. This chemical homogeneity of the functional groups around the probe results in a tighter distribution of electric fields, seen clearly in Figure 4.7 and inferred from the small FWHM in Table 4.2. However, when the nitrile is near the lipid headgroup, it is in a heterogeneous chemical environment where small changes in the position of the nitrile can make large changes in its nearest chemical neighbors, including the lipid headgroup, or water and ions in the near-surface region. This heterogeneous chemical environment near the lipid–solvent interface means that even small changes in orientation can place the nitrile in

dramatically different environments. This in turn leads to a wider distribution of electric fields experienced by the nitrile in the course of a steady state experiment, as calculated in Figure 4.7 and seen clearly in the vibrational absorption spectrum described in Table 4.2. While this intuitive result is not surprising, the close connection of the measured FWHM to calculated electrostatic fields from the MD simulations demonstrates the importance of good, long-time-scale MD simulations in interpreting spectral data of complex and heterogeneous biological systems. In conclusion, we have demonstrated the use of VSE spectroscopy on site-specific nitrile chromophore coupled with molecular dynamics simulation in a model vesicle membrane to directly measure the dipole electrostatic field contained within the low dielectric interior of the bilayer.

4.5 CONCLUSION

Previous VSE spectroscopy of nitriles introduced into model bicelle membranes assumed an orientation of the nitrile chromophore from simplistic models and lacked details on the distribution of orientations the nitrile might assume within the bilayer. We have addressed these shortcomings by using extensive molecular dynamic sampling to determine the distribution of angles the nitrile probe assumes in our experiments both from the tilt of the helix in the bilayer and the torsional rotation of the *p*-CN-Phe side chain. While our experimental results agree with previous measurements in bicelles, as well as other measurements in the literature, we now have included a range of values for the magnitude of the dipole field. Vesicles are a more chemically diverse and robust model membrane system than bicelles, and we have demonstrated a simple spectroscopic

methodology to probe the membrane electrostatic environment while maintaining the membrane integrity. Ongoing work in our laboratory is investigating the molecular origin of the dipole field and its role in membrane organization and function.

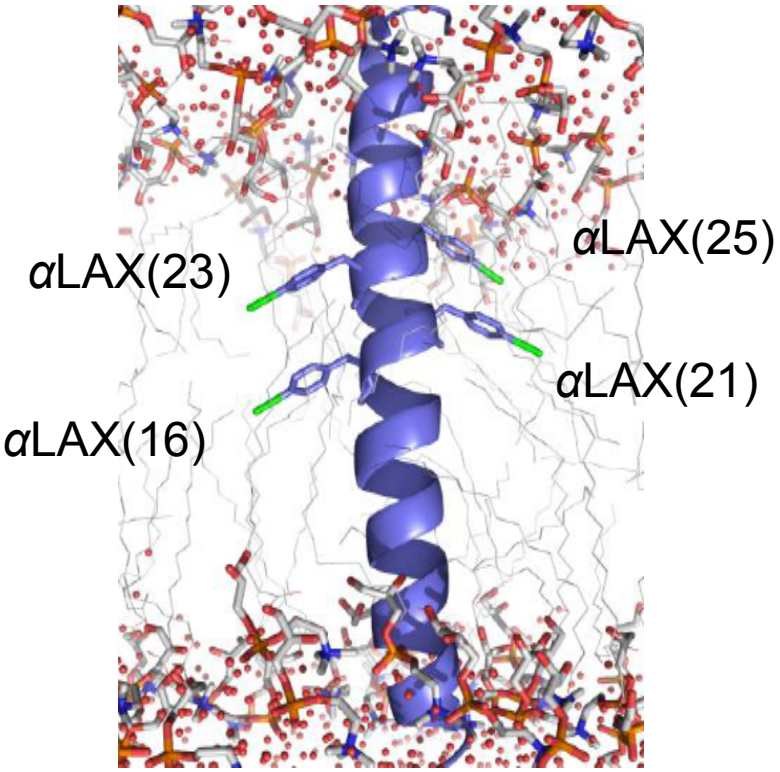

Figure 4.1: A molecular model of α-helix intercalated into the membrane interior containing the unnatural amino acid *p*-cyanophenylalanine (*p*-CN-Phe) at various positions along the polypeptide sequence. αLAX(25), αLAX(23), αLAX(21) and αLAX(16) represents the helix with *p*-CN-Phe incorporated at the position 25, 23, 21 and 16 respectively.

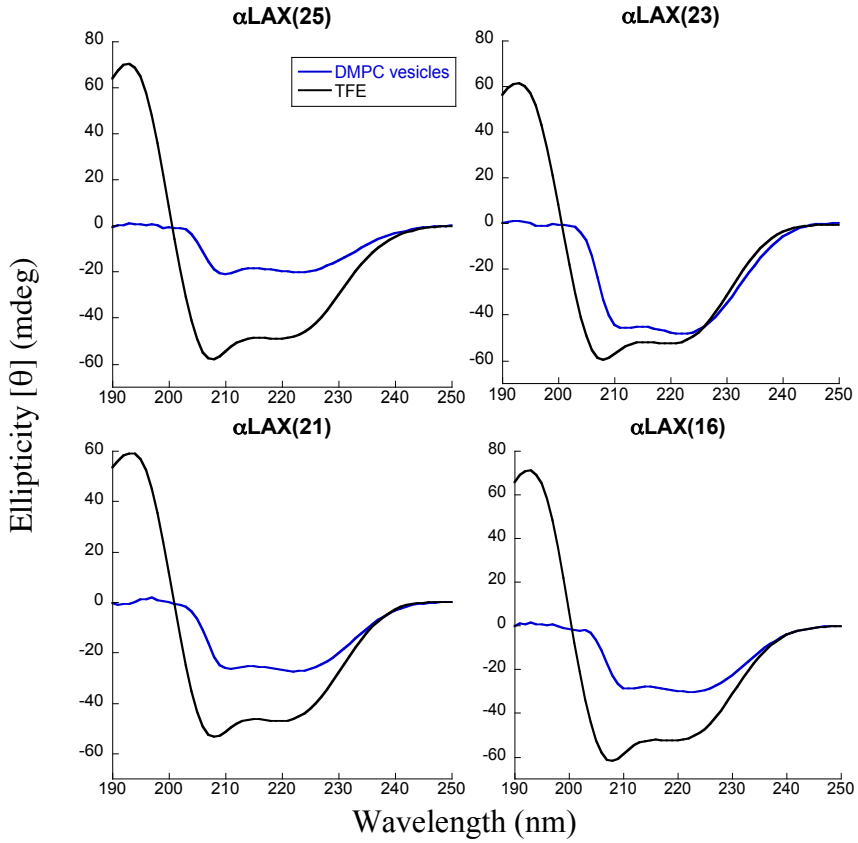

Figure 4.2: Representative CD spectra of 1 mM *α*LAX(25), *α*LAX(23), *α*LAX(21), and *α*LAX(16) dissolved in TFE (black) and intercalated in DMPC vesicles (blue). Spectral intensity is presented in units of mdeg.

(a) (b)

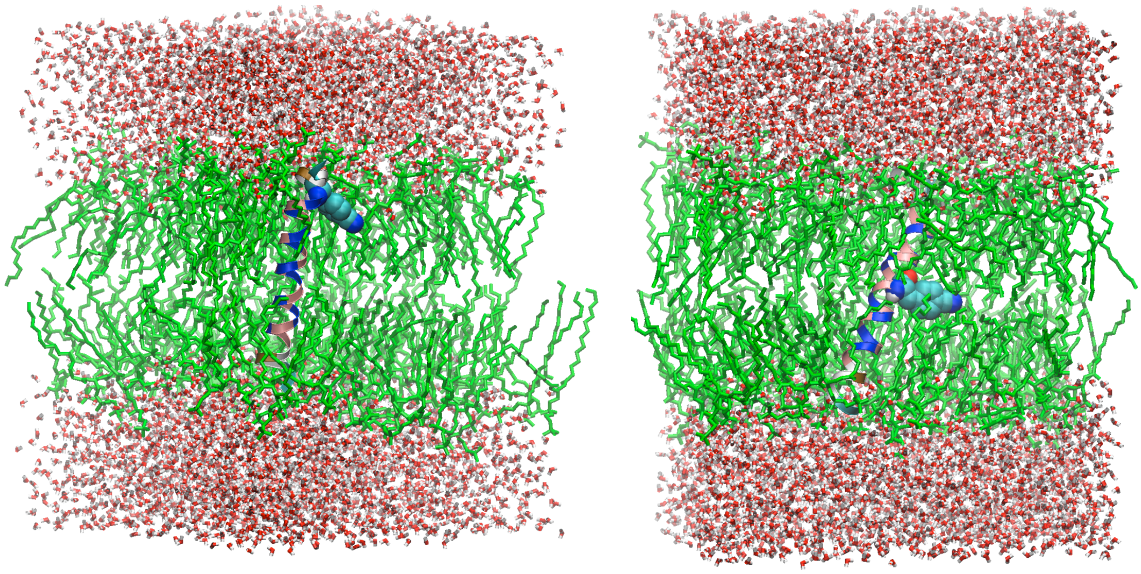

Figure 4.3: Snapshots of molecular dynamic simulations of (A) αLAX(25) and (B) αLAX(16) embedded vertically into a bilayer composed of 128 DMPC molecules (green), 5630 TIP3P water molecules (red and gray) and a molecule of each peptides (with the *p*-CN-Phe probe in space-filling representation). Molecular snapshots were prepared with the program VMD.

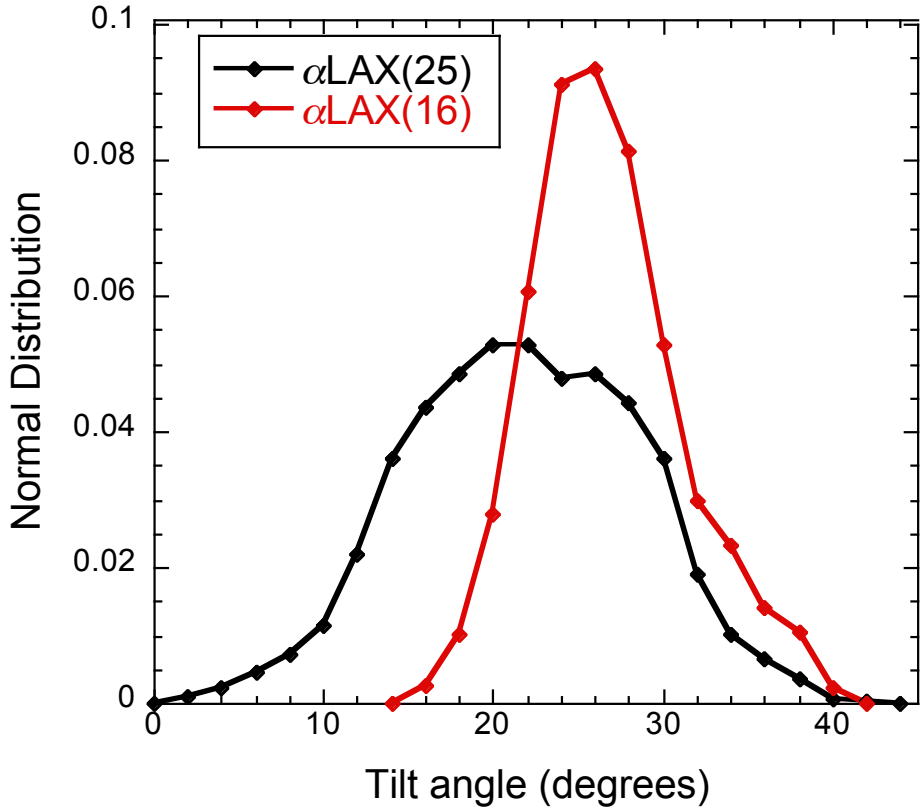

Figure 4.4: Normalized histogram of tilt angle distribution of transmembrane helical peptides, αLAX(25) (black) and αLAX(16) (red), with the normal of a lipid bilayer composed of 128 DMPC lipid molecules computed by molecular dynamics simulation.

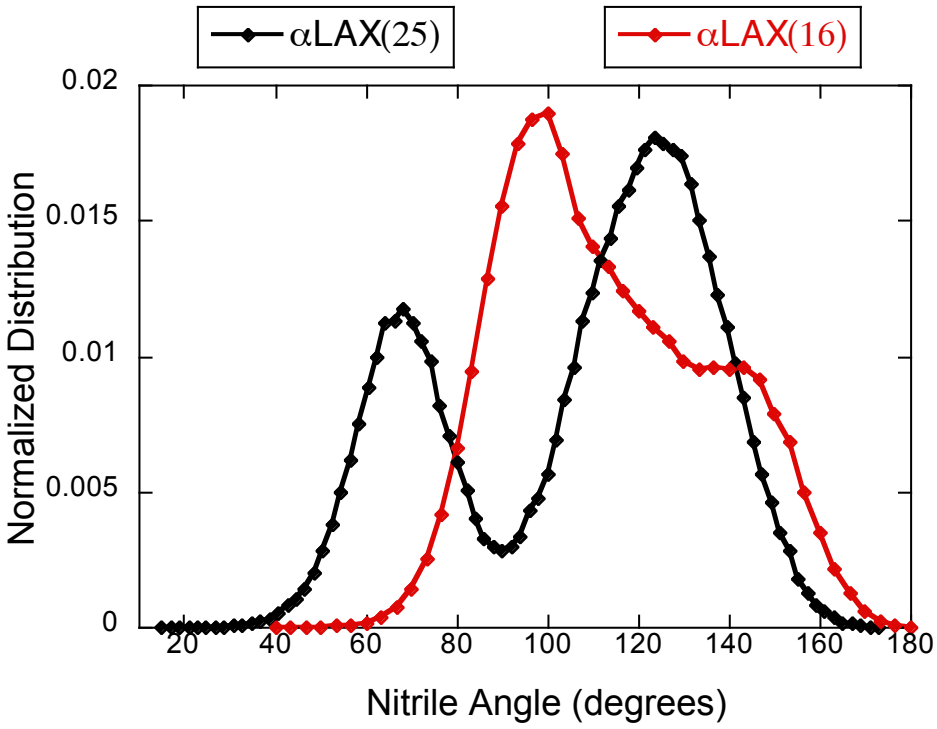

Figure 4.5: Normalized histogram of the angle between the nitrile probe on transmembrane peptide αLAX(25) (black) and αLAX(16) (red) and the normal of the bilayer composed of 128 DMPC lipid molecules computed by molecular dynamics simulation. The computed angle is the angle between the nitrile bond and the membrane axis.

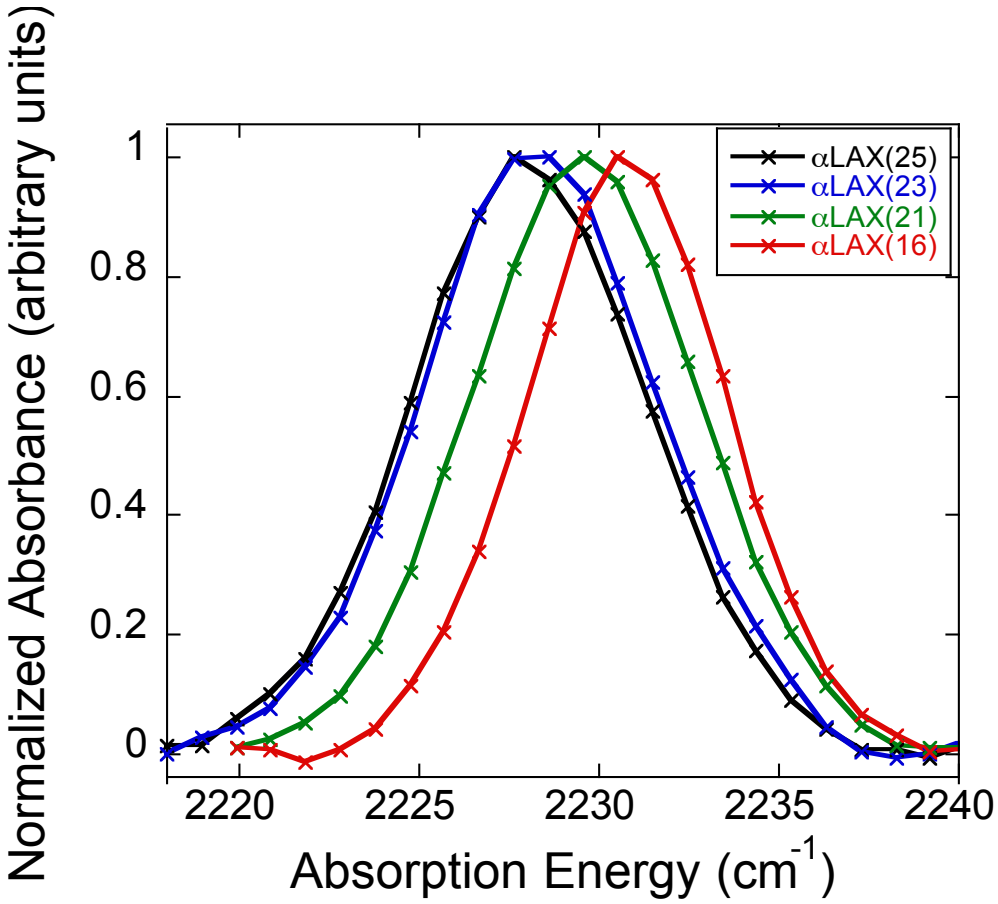

Figure 4.6: Normalized representative FTIR spectra of 0.5 mM peptides αLAX(25) (black), αLAX(23) (blue), αLAX(21) (green), and αLAX(16) (red) inserted in vesicles composed of 30 mM DMPC. Measured data points are shown by "×".

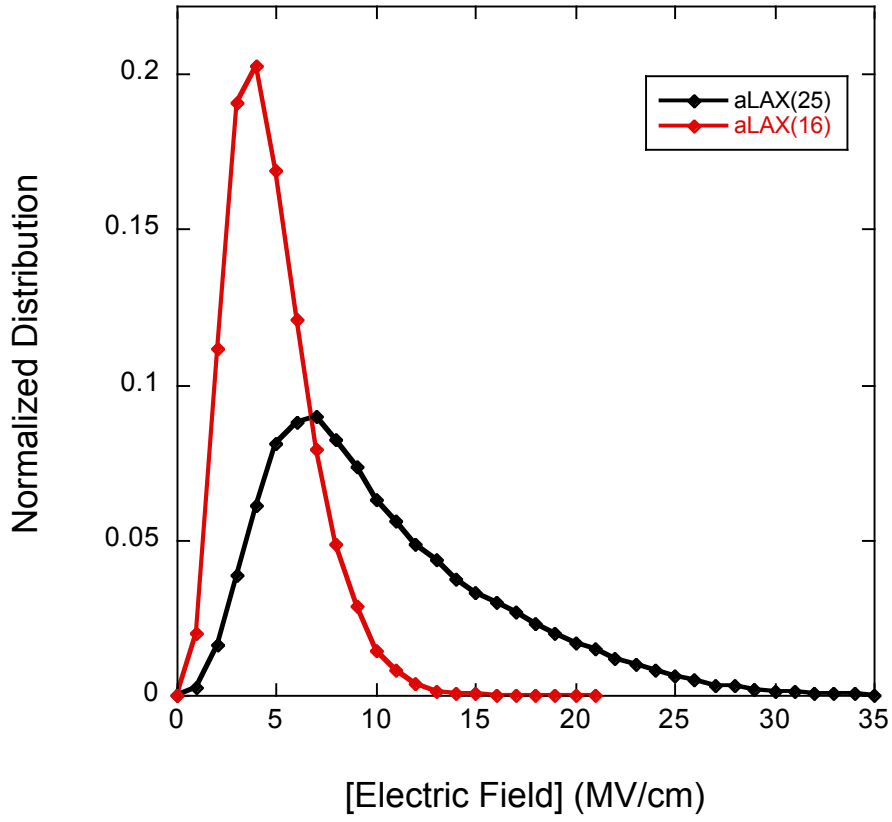

Figure 4.7: Normalized histogram of the absolute value of the electric field on Cα of the nitrile probe on transmembrane peptide αLAX(25) (black) and αLAX(16) (red) embedded into bilayer composed of 128 DMPC lipid molecules computed by molecular dynamics simulation.

Peptide	Sequence
αLAX(25)	HHGGPGLALALALALALALALA**X**GPGGHH
αLAX(23)	HHGGPGLALALALALALALALA**X**ALGPGGHH
αLAX(21)	HHGGPGLALALALALALALA**X**ALALGPGGHH
αLAX(16)	HHGGPGLALALALAL**X**LALALALALGPGGHH

Table 4.1: Amino acid sequences of the four polypeptides described in this work. X = *p*-CN-Phe.

	0.5 mM peptide		1 mM peptide	
Peptide	ν_{obs}	FWHM	ν_{obs}	FWHM
αLAX(25)	2228.18 ± 0.07	7.9 ± 0.1	2227.98 ± 0.06	7.0 ± 0.2
αLAX(23)	2228.51 ± 0.04	7.8 ± 0.4	2228.43 ± 0.05	6.9 ± 0.8
αLAX(21)	2229.86 ± 0.06	7.5 ± 0.1	2229.75 ± 0.06	6.9 ± 0.3
αLAX(16)	2231.05 ± 0.02	6.2 ± 0.1	2230.57 ± 0.05	6.2 ± 0.2

Table 4.2: Average mean peak frequencies (ν_{obs}) and full width half maximum (FWHM) of the nitrile stretching band for 0.5 mM and 1 mM peptides intercalated into DMPC vesicles.

4.6 REFERENCES

1. Hessa, T.; Kim, H.; Bihlmaier, K.; Lundin, C.; Boekel, J.; Andersson, H.; Hilsson, I.; White, S. H.; Heijne, G. von. Recognition of Transmembrane Helices by the Endoplasmic Reticulum Translocon. *Nature* **2005**, *433*, 377-381.
2. Johansson, A. C. V.; Lindahl, E. Amino-Acid Solvation Structure in Transmembrane Helices from Molecular Dynamics Simulations. *Biophys. J.* **2006**, *91*, 4450-4463.
3. Hu, W.; Webb, L. J. Direct Measurement of the Membrane Dipole Field in Bicelles Using Vibrational Stark Effect Spectroscopy. *J. Phys. Chem. Lett.* **2011**, *2*, 1925-1930.
4. Kelly, S. M.; Price, N. C. The Use of Circular Dichroism in the Investigation of Protein Structure and Function. *Current Protein and Peptide Science.* **2000**, *1*, 349-384.
5. Litman, B. J. Effect of Light Scattering on the Circular Dichroism of Biological Membranes. *Biochem* **1972**, *11*, 3243-3247.
6. Kučerka, N.; Nieh, M. P.; Katsaras, J. Fluid Phase Lipid Areas and Bilayer Thicknesses of Commonly Used Phosphatidylcholines as a Function of Temperature. *Biochim. Biophys. Acta.* **2011**, *1808*, 2761-2771.
7. Kučerka, N.; Liu, Y.; Chu, N.; Petrache, H. I.; Tristram-Nagle, S.; Nagle, J. F. Structure of Fully Hydrated Fluid Phase DMPC and DLPC Lipid Bilayers Using X-Ray Scattering from Oriented Multilamellar Arrays and from Unilamellar Vesicles. *Biophys. J.* **2005**, *88*, 2626-2637.

8. Webb, R. J.; East, J. M.; Sharma, R. P.; Lee, A. G. Hydrophobic Mismatch and the Incorporation of P1eptides into Lipid Bilayers: A Possible Mechnaism for Retention in the Golgi. *Biochem* **1998**, *37*, 673-679.
9. Getahun, Z.; Huang, C. Y.; Wang, T.; DeLeon, B.; DeGrado, W. F.; Gai, F. Using Nitrile-Derivatized Amino Acids as Infrared Probes of Local Environment. *J. Am. Chem. Soc.* **2003**, *125*, 405–411.
10. Waegele, M. M.; Culik, R. M.; Gai, F. Site-Specific Spectroscopic Reporters of the Local Electric Field, Hydration, Structure, and Dynamics of Biomolecules. *J. Phys. Chem. Lett.* **2011**, *2*, 2598-2609.
11. Getahun, Z.; Huang, C. Y.; Wang, T.; DeLeon, B.; DeGrado, W. F.; Gai, F. Using Nitrile-Derivatized Amino Acids as Infrared Probes of Local Environment. *J. Am. Chem. Soc.* **2003**, *125*, 405–411.

Chapter 5 Effect of Cholesterol on Membrane Dipole Field

5.1 INTRODUCTION

Biological membranes are complex, heterogeneous structures composed of amphiphilic lipids that form a bilayer scaffold into which small molecules and proteins can intercalate and alter the physical and chemical properties of the membrane. Of special interest to many researchers is the effect of the intercalation of cholesterol, which provides mechanical strength and fluidity to the cell membrane, a characteristic that distinguishes eukaryotic from prokaryotic cells. Cholesterol can constitute as much as 50% of the total molecular composition of a plasma membrane in eukaryotic cells,[1] thereby significantly influencing membrane organization, dynamics, and function. Experimental studies using nuclear magnetic resonance (NMR),[2,3,4] electron paramagnetic resonance (EPR),[5,6,7,8] and differential scanning calorimetry (DSC)[8,9,10,11] have repeatedly shown that cholesterol induces temperature dependent "dual effects" on the phases of the lipid bilayer; cholesterol makes the gel phase more fluid below the transition temperature (T_m) and the liquid crystalline phase more rigid above T_m. The later effect is significant for the role that this is believed to play in the formation of heterogeneous, dynamic, nanoscale domains enriched in glycolipids, sphingolipids, and cholesterol, often called "lipid rafts." These domains are thought to be crucial for cellular functions including signal transduction, cell adhesion, and membrane trafficking.[1,12] However, despite development of various *in vivo* visualization techniques of lipid rafts, there is still a lack of consensus about their size, definition and function.

Cholesterol and its derivatives such as 6-ketocholestanol (6-kc), ergosterol, and 7-dehydrocholesterol have various physicochemical effects on lipid membranes stemming from excluded volume, steric, and electrostatic factors that collectively modify bilayer structure, fluidity, and function. Of these, the sterols' effect on the membrane dipole potential (V_d) is the least understood.[13,14,15] A substantial amount of experimental and computational research have focused on this subject, but the results of these efforts have occasionally been contradictory. Several experimental results show that cholesterol increases the dipole potential inside a membrane,[15-20] but in contrast, other experiments and molecular dynamics (MD) simulations have concluded that cholesterol actually decreases the membrane dipole potential.[21,22] These contradictions could stem from a lack of understanding of the mechanism by which cholesterol affects electrostatic fields associated with the membrane. Researchers have proposed several hypothesis: 1) cholesterol increases dipole potential by altering the strength and orientation of dipole moments associated with lipid head groups;[16] 2) cholesterol increases the dipole potential by increasing the volume of lipid head group, which in turn reorganizes the presence of water dipole moments at the membrane interface;[17] or 3) the dipole moment of cholesterol itself adds incrementally to the magnitude of the electric potential dropped across the bilayer.[15] These hypothesizes have been proposed based on the results of a variety of indirect experimental techniques such as atomic force microscopy,[22] ion-transport rates,[23] ratiometric fluorescence measurements,[24,25] and conductance method;[26] or computationally through MD simulations[18,21,27,28] applied on lipid bilayers with different amounts of cholesterol.

In our work, we set out to examine these hypothesizes by directly measuring the magnitude of the dipole field inside a bilayer composed of a saturated phospholipid, 1,2-dimyristoyl-*sn*-glycero-3-phosphocholine (DMPC) and 0-40 mol% of cholesterol using vibrational spectroscopy experiments and extensive molecular dynamic simulation of model membranes. We implemented the vibrational Stark effect (VSE) spectroscopy of a nitrile probe that we systematically place across cholesterol containing bilayer by inserting α-helical peptides that we discussed in detail in earlier chapter 3. The nitrile vibrational probe is sensitive to the local environment surrounding it. As we move the nitrile probe from the membrane-water interface to the middle of the hydrophobic core, the electrostatic environment changes dramatically. The nitrile molecule reports the change in its local vicinity by shifting its vibrational absorption energy between αLAX(25) and αLAX(16). Using this absorption energy change, we calculated the absolute electric field, which in this case is the dipole field $\vec{F}_d$ between the two positions using Equation 1-1 inside vesicle lipid bilayer composed of different cholesterol concentration. We showed that cholesterol increased the dipole field at lower concentrations (~10 mol%) and decreased it at higher concentrations (up to 40 mol%). Molecular dynamics simulations studies of DMPC-cholesterol bilayers containing only αLAX(16) allowed us to examine the lateral organization of membrane components in model bilayers composed of 10, 20 and 40 mol% cholesterol concentration. The incorporation of cholesterol into the lipid bilayer mostly affects the ordering of the aliphatic chain and because peptide αLAX(16) positions the nitrile in the hydrophobic core, it accounts for the changes in the local environment around the aliphatic chains in

its absorption peak. From MD studies, we evaluated the effect of cholesterol concentration on the orientation of the helix and the nitrile probe attached to the helix. Using our experimental data and results from simulation studies, we demonstrate that both the chemical structure and the concentration of sterol affect the chemical environment of the bilayer in different ways, which in turn alters the membrane dipole field in complex yet predictable ways.

5.2 COMPARISON WITH 6-KETOCHOLESTANOL

In order to understand the molecular origin of cholesterol's effect on the internal membrane dipole potential, we carried out similar VSE measurements on lipid bilayers containing a cholesterol derivative, 6-ketocholestanol (6-kc). 6-kc is structurally similar to cholesterol with the same tetracyclic fused ring structure and a short 7 carbon long chain but has a ketone group replacing the double C-C bond on the second ring. We can think of this ketone group on 6-kc as a small perturbation on cholesterol molecule. The experiments with 6-kc were carried out by another fellow graduate student, Cari M. Anderson in the Webb group. Despite its structural resemblance to cholesterol, 6-kc has consistently been found to increase the membrane dipole field.[15,23,24,28,29] 6-kc has been shown to sit further up in the bilayer compared to cholesterol because of the additional oxygen that forms hydrogen bonds with the interfacial waters and increases membrane fluidity.[28] This is in contrast with cholesterol, which sits deeper in the bilayer under lipid head group "umbrellas," making the bilayer less fluid. By directly measuring the elelctrostatic dipole field in lipid bilayers containing these two very similar sterols, we

aim to elucidate and quantify how small sterols affect membrane electrostatics by changes in local membrane structure and organization.

5.3 CIRCULAR DICHROIC SPECTROSCOPY

In these experiments, we moved the position of nitrile probe along the bilayer normal by inserting a polypeptide containing the unnatural amino acid *p*-cyanophenylalanine at various locations along the sequence, as described previously in Table 4.1. The repeating leucine-alanine (LA) construct forms a strong hydrophobic helical peptide that is insoluble in buffer, but partitions into the self-assembling membrane bilayer during vesicle formation.[30] We confirmed the helical secondary structure of these nitrile-containing peptides inside vesicles containing 0-40 mol% cholesterol and 0-40 mol% 6-kc with CD spectroscopy. Figure 5.2 shows representative CD spectra obtained for 1 mM peptides intercalated into vesicles composed of (a) DMPC and 20 mol% cholesterol and (b) DMPC and 20 mol% 6-kc for the peptides αLAX(25) (black), αLAX(23) (blue), αLAX(21) (green), and αLAX(16) (red). All peptides show two significant minima located near 208 and 222 nm, which are characteristics of helical secondary structure.[31] On average, a homogeneous distribution of 1 mM peptide results in a ratio of 33 peptides per 1000 lipids. We did not observe any distortions in the CD spectra at any concentration or compositions, demonstrating that peptides did not aggregate within the bilayer at this low concentration. Although we are only showing data for vesicles containing 20 mol% sterol, this observation was consistent at all vesicle compositions.

5.4 MOLECULAR DYNAMICS SIMULATIONS

We computed molecular dynamics trajectories for the peptide αLAX(16) at different compositions of the sterols in a bilayer of DMPC lipids. We analyzed the orientation of the helix and the nitrile probe within the bilayer membrane and the hydrogen bonding between the phosphocholine head groups, glycerol backbone, sterols and water molecules at the membrane-water interface.

5.4.1 Peptide Orientation

Figure 5.3 shows representative snapshots taken from the equilibrated helix-membrane simulation of (a) 10 mol% cholesterol; (b) 20 mol% cholesterol; (c) 40 mol% cholesterol; (d) 10 mol% 6-kc; (e) 20 mol% 6-kc; and (f) 40 mol% 6-kc, run for a total of 200 ns each. For the results reported here, all analysis was done using data from the last 100 ns of the simulation to allow the system to equilibrate. These snapshots clearly show that the peptides are indeed helical and inserted parallel to the membrane normal with some, although not excessive, degree of tilt. Sterols are known to perturb the ordering of the alkyl fatty chains and the membrane bilayer thickness. The hydrophobic mismatch between the helical section of the peptide and the low dielectric hydrophobic alkyl chains in the bilayer creates a distribution in the angles of the helical backbone with respect to the membrane normal. We calculated this distribution of helix tilt angles from the simulation trajectories for each bilayer composition, and results are shown in Figure 5.4. The width of the distribution changed with the concentration of sterol molecules. For both sterols, the helix tilt angle distribution exhibits a broader range at 10 mol%

cholesterol than the distribution at either 20 mol% or 40 mol% cholesterol. In the case of 6-kc, the helix tilt angle shows a broader distribution in general at all concentrations compared to cholesterol, although the broadest distribution remains at the concentration of 10 mol%. The trend in the magnitude of the tilt angle as concentration changed was also consistent for both sterols. For each composition under investigation, the mean helix tilt angles were determined to be 12 ± 5°, 21 ± 4° and 20 ± 4 for 10, 20 and 40 mol% cholesterol respectively, and 30 ± 6°, 39 ± 5° and 35 ± 4° for 10, 20 and 40 mol% 6-kc respectively. The α-helix had a maximum tilt angle in bilayers containing 20 mol% of either sterol, followed by 40 mol%, then 10 mol%.

We also determined orientations of the nitrile bond inside the bilayer by measuring the *p*-CN-Phe side chain's N-Cα-Cβ-Cγ χ_1 torsional angle. In our experiments, the nitrile on peptide αLAX(16) is located in the middle of hydrophobic core of the lipid bilayer, so any changes in the ordering of lipid alkyl chains induced by different amounts of sterol affect the orientation of the nitrile. We combined this measurement with the measurement of the helix tilt angle shown in Figure 5.4 to determine the nitrile's orientation inside the bilayer with respect to the plane of the membrane. Figure 5.5 shows the normal distribution of this angle simulated for αLAX(16) in bilayers containing 10, 20 and 40 mol% cholesterol shown in solid line and in bilayers containing 10, 20 and 40 mol% 6-kc shown in dashed line . For cholesterol containing bilayers, we obtained a unimodal distributions of nitrile angle with respect to the membrane normal for 10 and 40 mol% cholesterol with mean angles of 113 ± 13° and 125 ± 10° respectively and bimodal

distribution for 20% cholesterol with two maximum angles at 120° and 85°. In the case of 6-kc, nitrile orientation remained unimodal at all sterol concentrations of interest with mean values of 90 ± 16°, 76 ± 16°, and 110±10° for 10, 20 and 40% 6-kc respectively. For the purpose of calculating the dipole electric field projected onto the oscillator's bond axis, we estimate the orientation of oscillator based on these mean average values obtained through this distribution analysis.

5.4.2 Hydrogen Bond Network

The membrane-water interface is extremely heterogeneous, due in large part to a network of hydrogen bonds between phospholipid head groups, water molecules and sterols. As sterol concentration changes, the distribution of these hydrogen bonds will change as well, altering the arrangement of dipoles at the membrane-water interface. Hence, quantitative analysis of the number of hydrogen bonds observed in simulations provides detailed information on structural and chemical rearrangements in the sterol-lipid bilayer as a function of sterol concentration. We calculated average number of hydrogen bonds for different hydrogen bonding chemical pairs. In Figure 5.6, we show the average number of hydrogen bonds between phospholipid-water (black), phospholipid-phospholipid (blue), phospholipid-sterol (green), sterol-sterol (red), and sterol:water (magenta) calculated from MD simulations of lipid bilayer containing cholesterol (solid lines) or 6-kc (dashed lines). Figure 5.6 highlights two important observations: (i) the number of hydrogen bonds between phospholipids and water were largest compared to other molecules because of the greater number of hydrogen bond

donors and acceptors located at the phospholipid head group; and (ii) the only significant difference between cholesterol and 6-kc in this analysis was the extent of hydrogen bonding between the sterol and the water (data shown in magenta). Because of the extra ketone functional group on 6-kc, this sterol is susceptible to significantly more hydrogen bonds to water than cholesterol (1 versus 0.6 hydrogen bonds per sterol, respectively) at all concentrations. This observation is significant because water dipoles are thought to be the major contributor to the magnitude of the dipole field. We will return to this observation in the discussion section.

5.5 Fourier Transform Infrared Spectroscopy

5.5.1 Vibrational Absorption Energy Shifts

In our FTIR experiments, we used α-helical peptides containing a single *p*-CN-Phe unnatural amino acid to incorporate the nitrile oscillator at four different positions within the bilayer, beginning from the membrane-water interface with peptide αLAX(25) and progressing towards the middle of hydrophobic core with peptide αLAX(16). The potential gradient between the lipid's charged head group and terminal alkyl chains creates a strong dipole field that shifts the vibrational absorption energy of the nitrile oscillator between αLAX(25) and αLAX(16). Figure 5.7 shows representative normalized infrared spectra of αLAX(25) (black), αLAX(23) (blue), αLAX(21) (green), and αLAX(16) (red) placed into vesicles composed of DMPC and 20 mol% cholesterol. The absorption energy of the nitrile increased by 2.7 cm^{-1} between αLAX(25) and αLAX(16). We determined the vibrational energy shifts ($\Delta\nu_{obs}$) at each composition and

the results are plotted in Figure 5.8 for different concentrations of cholesterol represented by black triangle and for different concentration of 6-kc represented by red triangles. As we increased the concentration of cholesterol in our vesicles from 0 to 10 mol%, the $\Delta\nu_{obs}$, increased from 2.59 cm^{-1} to 2.85 cm^{-1} but as we increased beyond 10 mol%, the $\Delta\nu_{obs}$ began to decrease to as low as 2.37 cm^{-1} for 40 mol% cholesterol. In contrast, in vesicles containing 6-kc, $\Delta\nu_{obs}$ increased monotonically with increasing concentration over the entire range examined.

Using these experimentally measured values of $\Delta\nu_{obs}$, the nitrile's Stark tuning rate of 0.67 cm^{-1}/ (MV/cm),[32,33] and the average nitrile angle obtained from MD simulations, we calculated the dipole field using Equation 1-1. Because of the computational costs of the MD simulations, we performed MD calculations only on systems with sterol concentrations of 0, 10, 20 and 40 mol% while we collected experimental $\Delta\nu_{obs}$ data for 0, 5, 10, 15, 20, 25, 30 and 40 mol% sterol. So, in order to determine the nitrile orientations in lipid bilayer with 5, 15, 25 and 30 mol% sterol, we estimated the angle for each composition with the one calculated for the immediately lower concentration. For example, for 15 mol% cholesterol, we used the average nitrile angle of 113° that we calculated from the normal distribution plot obtained for 10 mol% cholesterol. In the case of lipid bilayers containing 6-kc, we used the nitrile angle of 112° for 0-15 mol% 6-kc, 76° for 20-35 mol% 6-kc and 110° for 40 mol% 6-kc. Our MD simulations on 10 mol% 6-kc resulted in a mean average angle of 90° which would imply no shift in the nitrile's absorption energy. This is in contrast with the experimental result, and so we consider the average nitrile angle calculated from this simulation to be an

outlier. Because of this, we estimated the nitrile orientation for 0 to 15 mol% 6-kc with the average nitrile angle that we calculated for 0 mol% 6-kc. This is a reasonable assumption because previous experiments have demonstrated that at low concentrations, 6-kc perturbs the lipid alkyl chains only minimally, and the local environment around the nitrile are essentially the same in bilayers with and without 6-kc. The calculated dipole field values and their corresponding experimental $\Delta\nu_{obs}$ are presented in Table 5.1.

Results in Table 5.1 clearly show that the absolute dipole field within a lipid bilayer changes both with the structure of intercalated sterol molecule and its concentration. It increases slightly by ~1 MV/cm upon incorporation of a small amount of cholesterol (10 mol%), then drops substantially to 6 MV/cm as the cholesterol concentration increases to the highest value of 40 mol%. The large errors that are reported for $\vec{F}_d$ in Table 5.1 do not reflect experimental errors, but represent distribution of the field calculated based upon the range of computational sampling of the nitrile orientation within the bilayer obtained from MD simulation.

5.5.2 Analysis of Spectral Line Widths

The addition of sterol molecules to a lipid bilayer increases heterogeneity of the system mostly by changing the ordering of the lipid alkyl chains. The nitrile probe on peptide αLAX(16) places the oscillator at the ends of these alkyl tails where the system is most perturbed. The oscillator is very sensitive to the local chemical environment, which is reflected in the full width half maximum (FWHM) values of its absorption peak.[34] In Figure 5.9, we plot the experimental average FWHM values for the absorption peaks of

the nitrile attached to αLAX(16) that we placed in vesicles containing 0-40 mol% of each sterol. For cholesterol containing bilayers, the FWHM values of nitrile peaks, shown in black circles, rises monotonically with higher cholesterol concentration while the FWHM values of nitrile peaks in 6-kc containing bilayers, shown in red circles, do not exhibit any clear trend as a function of concentration, and appear to gyrate around a value of ~6.5 cm^{-1}. This result indicates that the central region of the bilayer, where the nitrile in αLAX(16) is placed, gets progressively more diverse in its chemical environment as the concentration of cholesterol is increased, but remains relatively homogeneous as more 6-kc is added. The analysis on FWHM values in addition to the absorption frequency values, the number of hydrogen bonds and the distribution of helix tilt and nitrile angle, all indicate that cholesterol and 6-kc, despite of their similar structures, perturb the local structure and chemical environment of the lipid bilayer very differently. As a result, lipid bilayers create unique electrostatic profiles in presence of sterols, which greatly affect the dipole field across the headgroup and the bulky hydrophobic interior.

5.6 DISCUSSION

Cholesterol intercalation into a lipid bilayer membrane induces ordering in the alkyl chains of lipid membranes,[35,36] increasing membrane density,[36,37,38,39,40] decreasing fluidity,[41.42] and increasing mechanical strength.[43] The purpose of this work is to elucidate the effect of cholesterol and an analogue sterol, 6-kc on the magnitude of the membrane's dipole electric field. Cholesterol can impact the dipole field in two ways: 1) directly through the inclusion of its own molecular dipole moment (~2.01 D)[15] into the system of

ordered dipoles; or 2) indirectly by inducing changes in the physicochemical properties of membrane including fluidity, stiffness, and packing.[16-21]

One of the most widely observed impacts of cholesterol in lipid membranes is its condensing effect because of the non-ideal interaction of cholesterol with phospholipids.[44] Cholesterol participates in hydrogen bonding with water molecules and other phospholipids through a polar hydroxyl group or via water bridges, thus anchoring itself to the membrane-aqueous interface.[45] Molecular simulations have shown that upon incorporation of cholesterol into a pure lipid bilayer, there is a decrease in the formation of *gauche* rotamers in the lipid alkyl chains and a substantial reduction in the average tilt of the lipid chains with respect to the plane of the membrane bilayer.[21] These two structural effects straighten the hydrocarbon tails of the lipid, which in turn increases the packing density of lipid molecules and condenses the area per molecule.[21,37,38,46]

However, the sterol's condensing effect strongly depends on temperature and lipid bilayer composition.[12,46-48] Several ^{2}H NMR measurements and MD simulation studies have predicted a binary cholesterol-phospholipid phase diagram showing distinct phases at different cholesterol concentrations.[48] A pure lipid bilayer exists in a gel-like phase below the transition temperature, and a fluid-like liquid disordered phase (L_d) above the transition temperature.[48] At low concentrations (≤10 mol%) and temperatures above T_m, cholesterol has minimal effect on the alkyl chain ordering and the lipid bilayer exists as liquid disordered phase L_d.[48] At slightly higher concentration, between 10-22 mol%, cholesterol lowers the enthalpy of s_o-to-L_d phase transition and induces an intermediate region, the liquid ordered phase (L_o) in which lipids have the lateral mobility

of the fluid phase but alkyl chains are ordered just like in the gel phase, coexisting with L_d phase. [44-48] At higher concentrations (≥ 22 mol%), cholesterol-phospholipid bilayers exist in all L_o phase forming clusters of cholesterol enriched domain.[44-48] However no such phase transitions have been reported for 6-kc-phospholipid bilayer. The extra ketone group on the 6-kc maintains the hydration level at the membrane-water interface and the bilayer always exists in L_d phase. ^{31}P NMR experiments performed by Cari Anderson show an increase in the fluidity of the lipid bilayer upon intercalation of 6-kc into lipid bilayer.

Although we did not collect calorimetric data to show phase transitions in our experiments, we can rationalize the differences in the dipole field based on the lipid packing density at different concentrations of sterols. In Figure 5.10, we show schematic representations of phospholipid, peptide and sterol organization in lipid bilayers containing 0 mol% (Figure 5.10a), 10 mol% (Figure 5.10b), and 40 mol% cholesterol (Figure 5.10c), and 40 mol% 6-kc (Figure 5.10d), all shown at temperatures above the T_m. Taken together, Figure 5.10 shows a possible mechanism for lateral organization of lipids at different concentrations of sterols based on our analysis of the experimental FWHM values of the absorption peak of nitrile in αLAX(16) (Figure 5.9), qualitative analysis of helix tilt angle distribution (Figure 5.4) and extent of hydrogen bonding between the sterol and the water molecules (Figure 5.6) obtained from MD simulation of sterol-lipid-peptide bilayer.

With no sterol, a lipid bilayer above T_m is in a fluid or liquid disordered phase (Figure 5.10a). Upon incorporation of a small amount of cholesterol up to ~10 mol% into

the bilayer, phospholipids remain in the disordered state; however the interaction between cholesterol and phospholipids reduces the area occupied by each lipid and lengthens the bilayer. The structural change results in increased lipid packing, which allows for incorporation of a greater number of lipids in a vesicle, represented in Figure 5.10b. This increases the macroscopic disorder of the bilayer, which is exhibited by the broad distribution of the helix tilt angle of αLAX(16) shown in Figure 5.4 that we calculated from 100 ns long simulation of bilayers containing 10 mol% cholesterol. Also, as the number of phospholipids increases, the density of the water molecules that are hydrogen bound to the phospholipid head group increases as well, shown in Figure 5.6. Hence, at 10 mol% cholesterol, the elevated packing of phospholipids, cholesterol and water molecules in a bilayer collectively increase the dipole density at the membrane-water interface causing the net dipole field to go up.

At concentrations greater than 10 mol% cholesterol, the magnitude of the measured dipole field steadily decreases. We propose that this decline is due to the formation of cholesterol-rich ordered domains, shown schematically in Figure 5.10c for bilayers with 40 mol% cholesterol. Previous studies of the binary lipid-cholesterol phase diagram discussed above have demonstrated that cholesterol induces liquid ordered phase at high concentrations of 40 mol%. Although our data does not exhibit such phase transitions in our experiments directly, it does suggest that chemical components of our bilayer system have transitioned to a more ordered state. For example, the normal distribution plots of the helix tilt angle calculated for bilayers with 20 mol% and 40 mol% cholesterol are narrower compared to 10 mol% cholesterol (Figure 5.4). A narrow

distribution implies that the helix is sampling a smaller range of tilt due to restricted motion in a more ordered environment. In terms of formation of cholesterol rich domains, the increasing FWHM values of the nitrile absorption peak in αLAX(16) with increasing cholesterol concentration (Figure 5.9) implies that the nitrile probe is now positioned at two different chemical environments: one enriched in phospholipids with ordered tails and the other enriched in cholesterol. The intrinsic dipole moment of cholesterol is 2.01 D, which is significantly smaller than the dipole of a DMPC phospholipid (~14 D), particularly when it is decorated with hydrogen-bound water molecules.[15] In cholesterol-rich domains, the direct effect from the smaller dipole moment of cholesterol is much more prominent than the indirect effect resulting from condensing of the membrane, thus decreasing the dipole field.

The effect of increasing concentrations of 6-kc on the membrane dipole field is starkly different. As shown schematically in Figure 5.10d, it is homogeneously distributed across a bilayer with no significant change in lipid packing. The phospholipid and 6-kc mixing is ideal at all concentrations of sterol and no domain formation is promoted. This mechanism is supported by the normal distribution plots of the helix tilt angle simulated for bilayers containing different concentrations of 6-kc (Figure 5.4), which are broad in general, as well as the FWHM of the nitrile-stretching band, which do not systematically change with 6-kc concentration (Figure 5.9). Because of the ideal mixing, as sterol concentration increases so does the dipole density from the sterol (~4 D) and hydrogen bonded water molecule, which is larger than the one associated with cholesterol due to the extra H-bond acceptor oxygen atom. This is verified by the

quantitative hydrogen bond analysis between sterol and water molecules (Figure 5.6), in which the number of hydrogen bonds associated with 6-kc is larger than one with cholesterol. Because of these factors, incorporation of 6-kc increases the overall dipole density with no accompanying hydrophobic screening, all of which contributes to a higher membrane dipole field compared to its ketone-less cholesterol analog.

Our results shed light on the sometimes conflicting results about the effect of sterols, particularly cholesterol, on membrane electrostatics. We show that cholesterol has the tendency to both increase as well as decrease the membrane dipole field, depending on phase changes induced by the addition of greater and greater quantities of cholesterol to the membrane. These results, when combined with the extensively studied cholesterol-lipid phase diagram and additional insight from the literature,[15-20] reveal that the dipole field is greater in the liquid disordered state than in the liquid ordered state. Moreover, we also show that adding an extra ketone group onto the cholesterol molecule completely perturbs the local electrostatic environment at the membrane-water interface and contributes to a monotonic increase in dipole field with increasing 6-kc concentrations. Using two sterols, we have shown how complex and dynamic systems such as biological membranes can be altered by the addition of a single ketone group on the sterol, with significant effects on non-covalent properties of the membrane such as the dipole field.

5.7 CONCLUSION

In conclusion, it is well known that the non-covalent intercalation of cholesterol into biological membranes has a great impact on membrane fluidity, self-association, and function. Despite extensive experimental and theoretical investigations, there is limited agreement on how and to what extent cholesterol and other sterols, such as 6-kc, alter a membrane's electrostatic potential, largely due to limited techniques for studying a property contained entirely within membrane interior. By addressing this with VSE spectroscopy and MD simulations, we measured changes in the dipole field as a function of sterol concentration and identity. These results were interpreted in terms of a phase transition that cholesterol-containing bilayers undergo above a concentration of 10 mol% sterol that is not seen in similar samples containing 6-kc. We demonstrate that at low concentrations of cholesterol, the lipid alkyl chain remains in a disordered L_d phase, resulting in greater dipole field. However, at higher concentrations of cholesterol up to 40 mol%, a transition to the liquid ordered phase causes a decrease in dipole field. This is in contrast with the consequences of adding 6-kc to the membrane, which results in a monotonic increase in dipole field as the concentration of 6-kc is increased. Through molecular-level understanding of cholesterol's contribution to the membrane dipole potential, future work in this laboratory will focus on how this electrostatic field regulates significantly more complex lipid membrane mechanisms such as binding of membrane-proteins and ion channel formations.

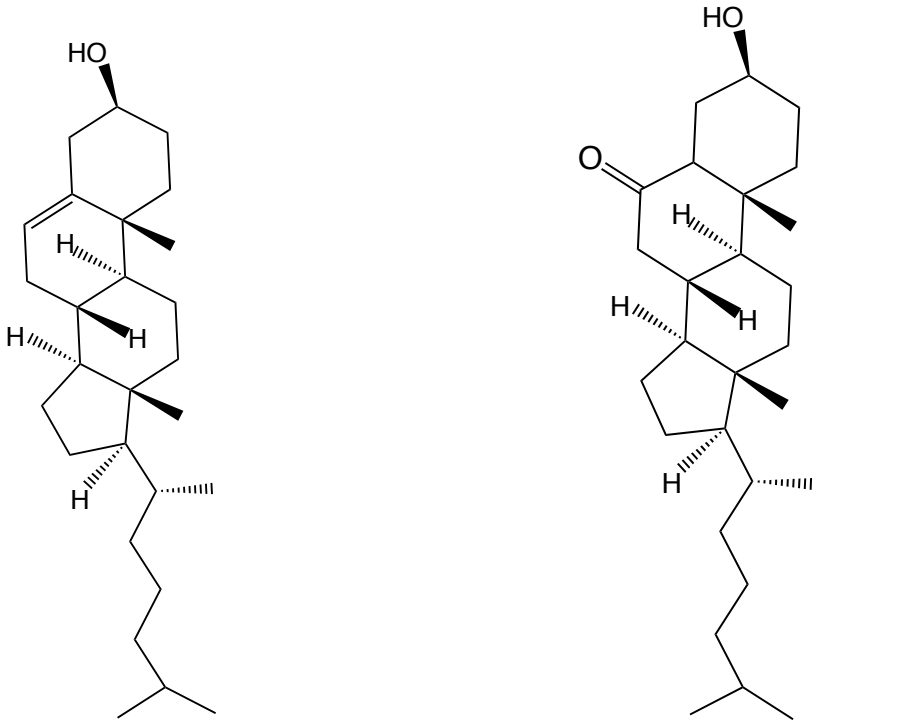

Cholesterol **6-Ketocholestanol**

Figure 5.1: Molecular structures of cholesterol and 6-ketocholestanol (6-kc).

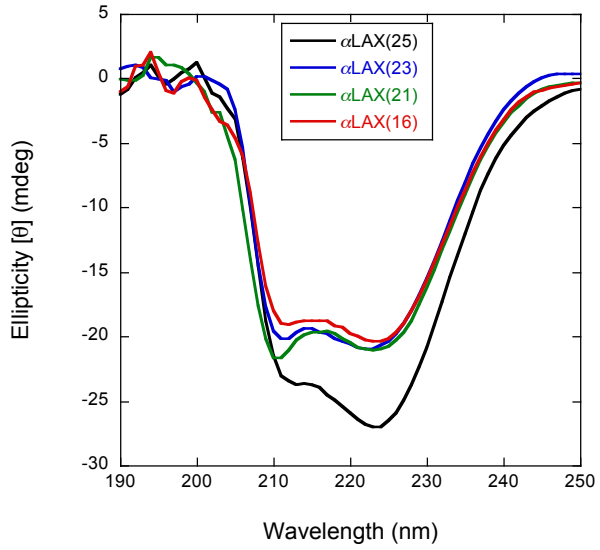

(a)

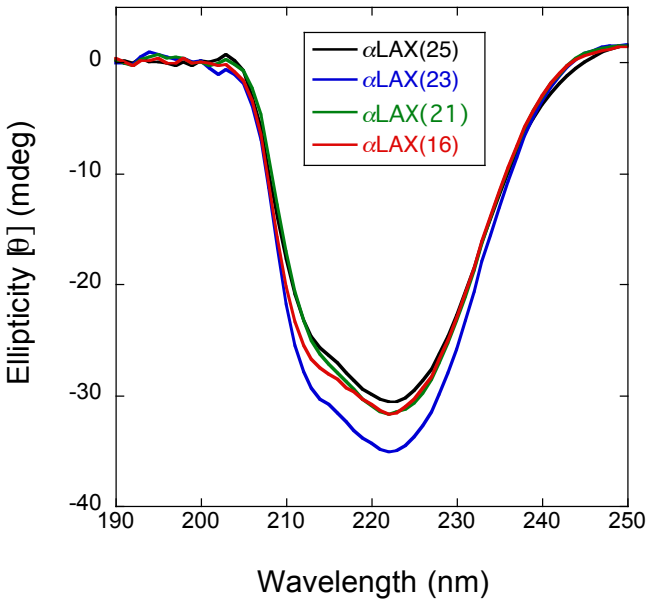

(b)

Figure 5.2: Circular dichroic (CD) spectra of 1 mM peptides: αLAX(25) (black), αLAX(23) (blue), αLAX(21) (green), and αLAX(16) (red) inserted in vesicles composed of (a) 30mM DMPC and 20 mol % cholesterol and (b) 30mM DMPC and 20 mol % 6-kc

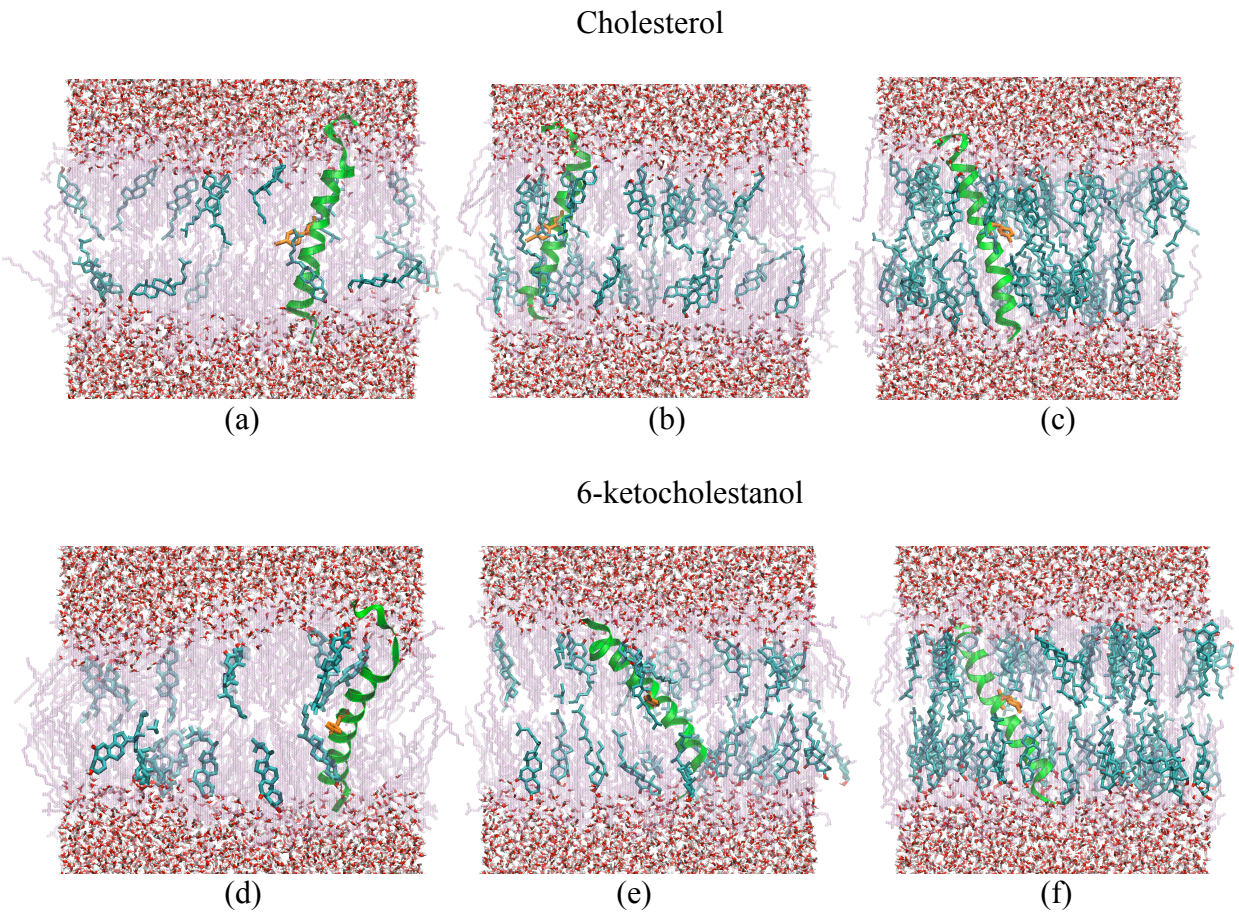

Figure 5.3: Representative snapshots taken from molecular dynamic simulations of *α*LAX(16) aligned vertically inside a lipid bilayer composed of DMPC molecules and (a) 10 mol% cholesterol; (b) 20 mol% cholesterol; (c) 40 mol% cholesterol; (d) 10 mol% 6-kc; (e) 20 mol% 6-kc; and (f) 40 mol% 6-kc. SPC water molecules are shown in red and gray, sterol molecules are shown in cyan, the *p*-CN- probe is shown in orange and DMPC phospholipids are shown in light purple. Molecular snapshots were prepared with the program VMD.

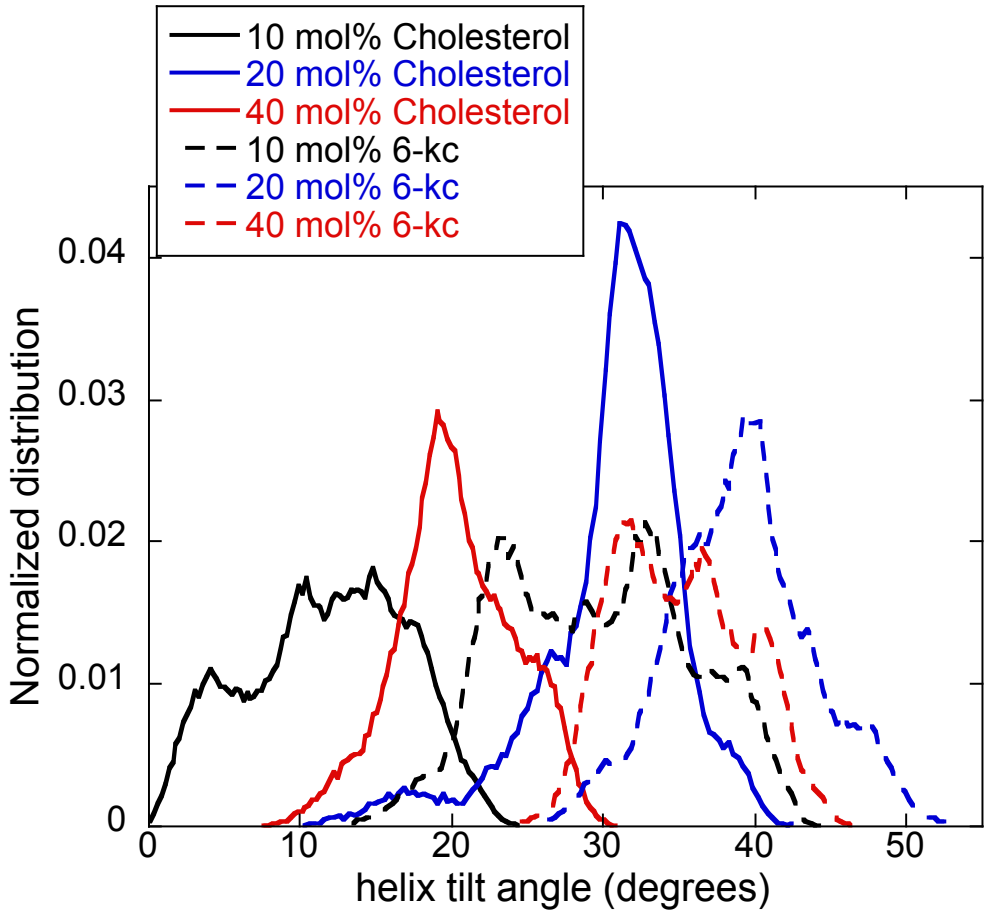

Figure 5.4: Normalized distribution of the helix tilt of αLAX(16) with respect to the membrane normal obtained from MD simulation of the peptide embedded into bilayer composed of DMPC and cholesterol (solid line) and DMPC and 6-ketocholestanol (dashed line) at concentrations of 10 mol% (black), 20 mol% (blue) and 40 mol% (red).

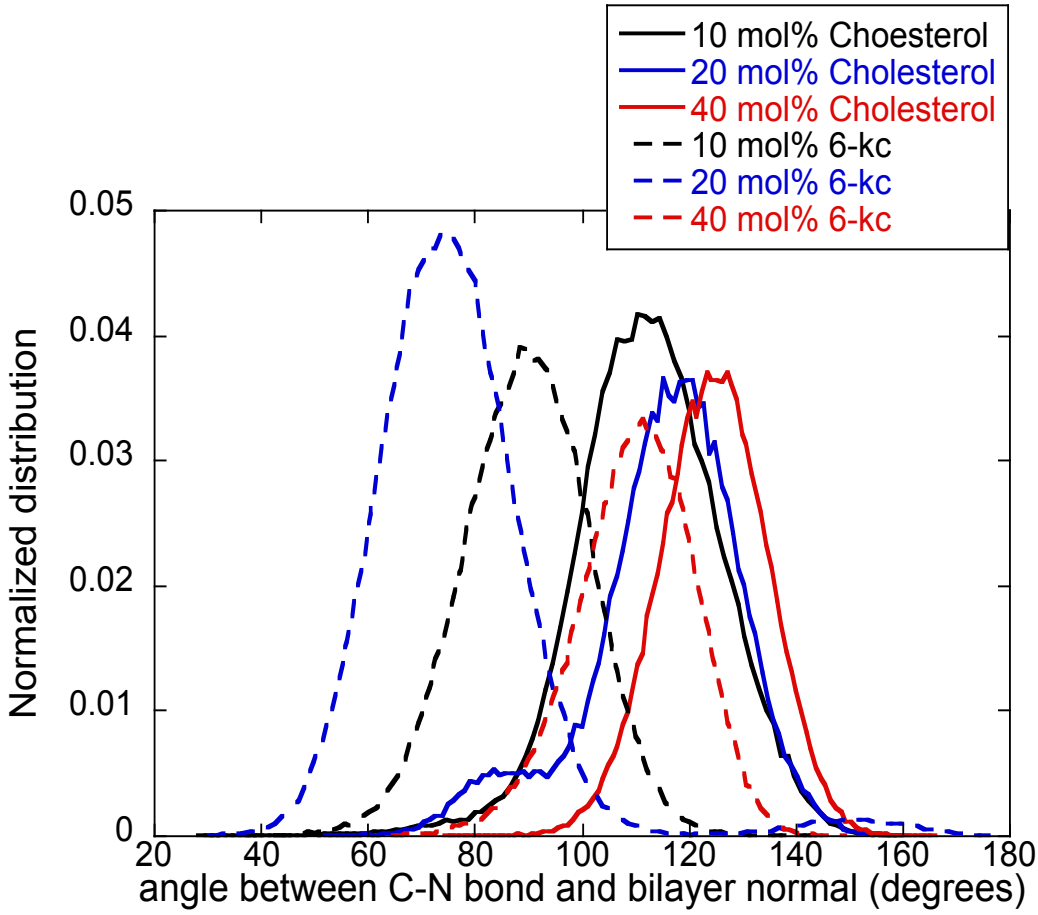

Figure 5.5: Normalized distribution of all possible orientations that nitrile oscillator samples with respect to the membrane normal in MD simulations of αLAX(16) peptide embedded into bilayer composed of DMPC and cholesterol (solid line), and DMPC and 6-ketocholestanol (dashed line) at concentrations of 10 mol% (black), 20 mol% (blue) and 40 mol% (red).

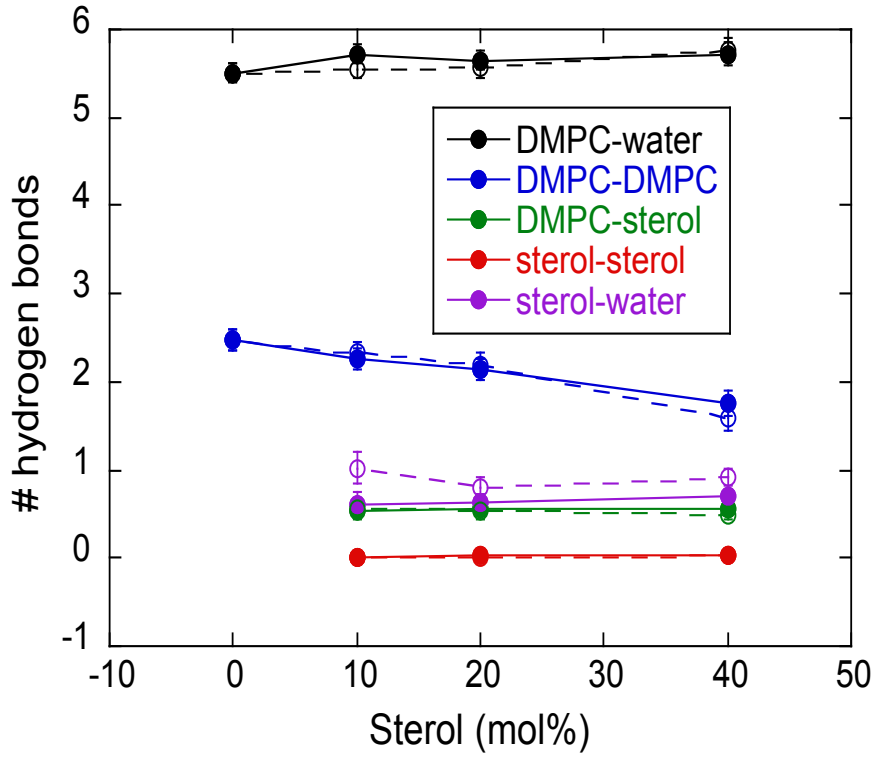

Figure 5.6: The average number of hydrogen bonds calculated between phospholipid-water (black); phospholipid-phospholipid (blue); phospholipid-sterol (green); sterol-sterol (red); and sterol-water (purple) in lipid bilayer containing cholesterol (solid circles) and 6-kc (unfilled circles) at different concentrations.

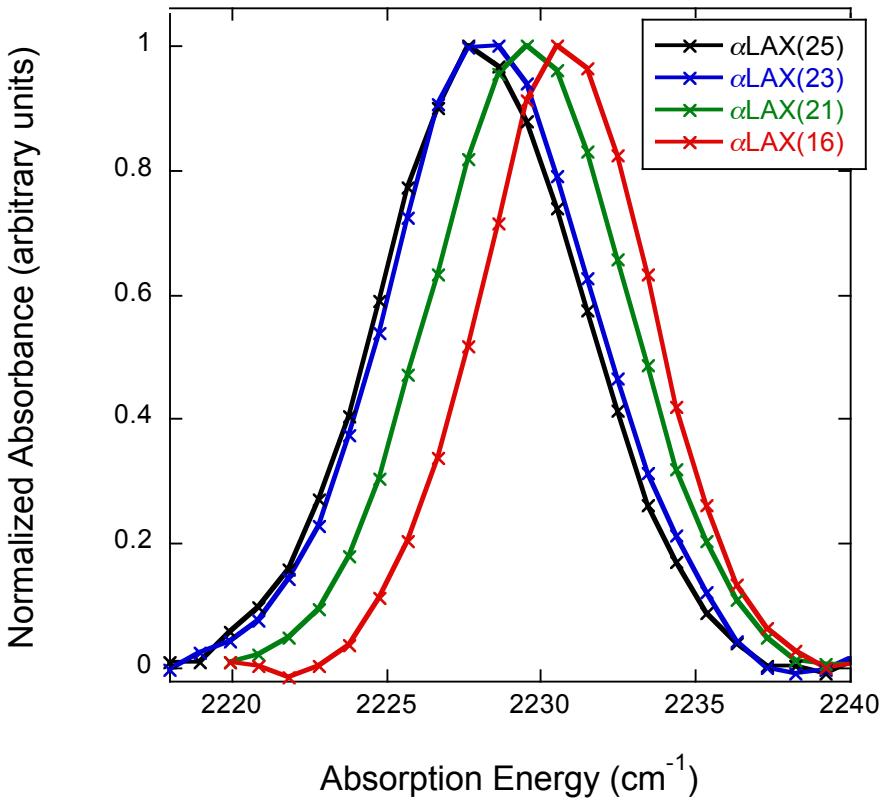

Figure 5.7: Normalized representative FTIR spectra of 1 mM peptides αLAX(25) (black), αLAX(23) (blue), αLAX(21) (green), and αLAX(16) (red) inserted in vesicles composed of 30 mM DMPC and 20 mol % cholesterol. Experimental data points are shown with "×".

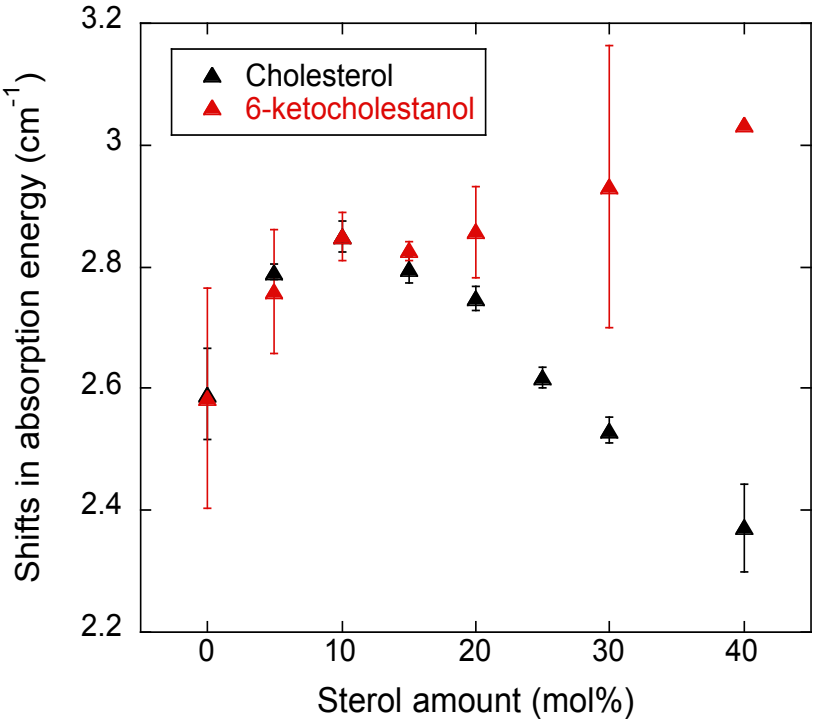

Figure 5.8: Average shifts in vibrational absorption energy of nitrile attached to αLAX(25) and αLAX(16) placed inside DMPC lipid bilayer containing cholesterol (black triangles) and 6-kc (red triangles), at different concentrations. Error bars show the standard deviation from at least three measurements.

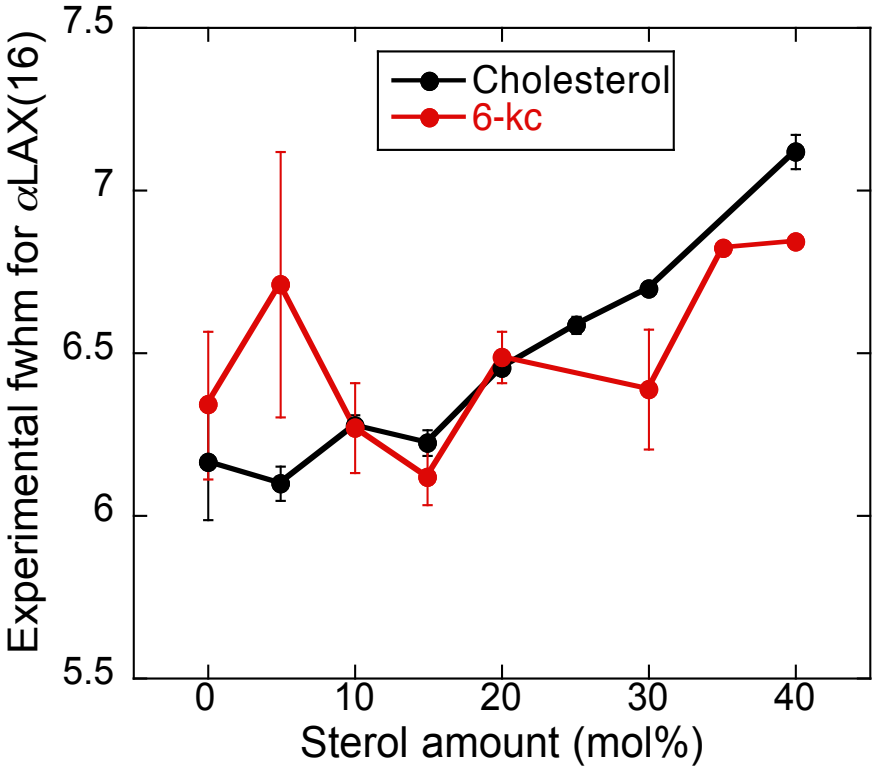

Figure 5.9: Average full width half maximum values for vibrational absorption peaks of nitrile placed inside DMPC lipid- αLAX(16) bilayer containing different concentrations of cholesterol shown in black and 6-kc shown in red. The values were average of at least three measurements.

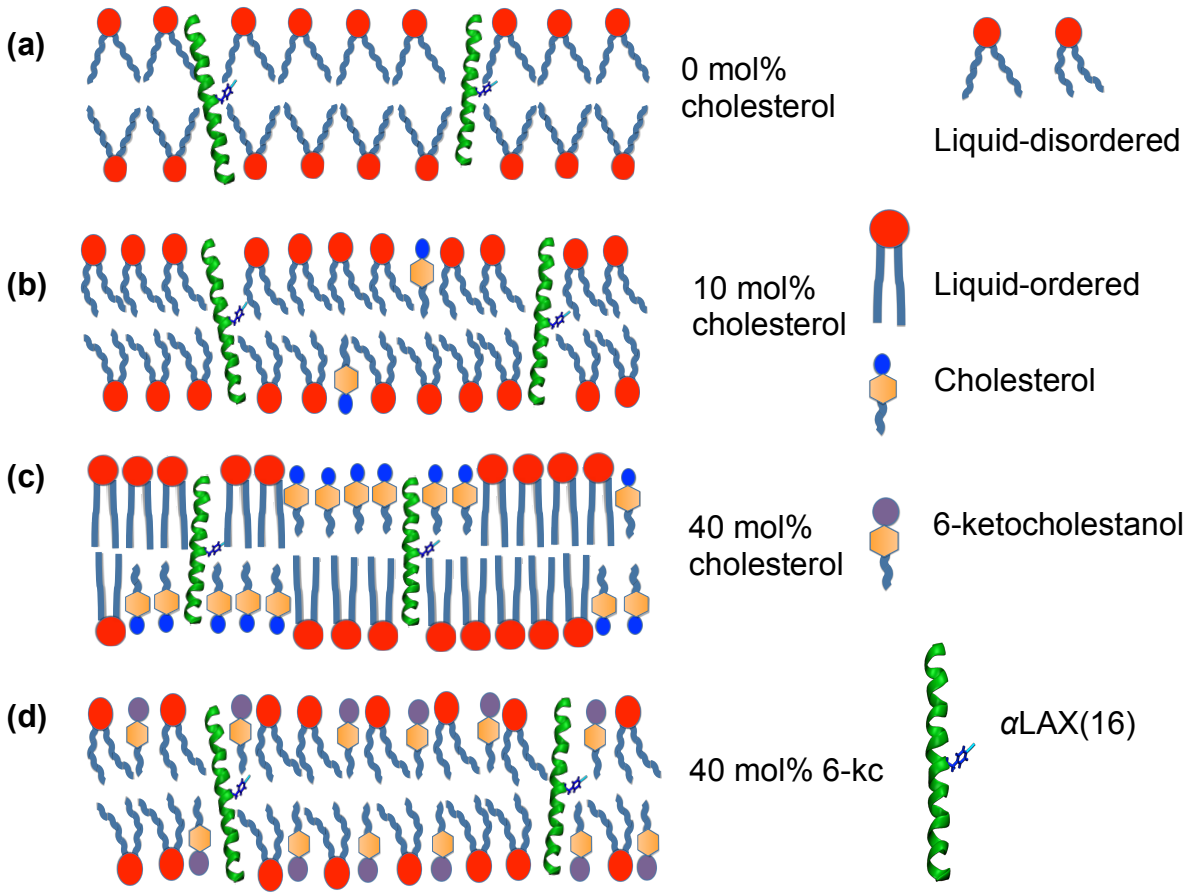

Figure 5.10: Schematic diagram of different proposed phases of the sterol-lipid-*α*LAX(16) bilayer at varying sterol concentration. (a) Fluid-like liquid disordered phase (L_d) above T_m with 0 mol% cholesterol; (b) L_d phase with 10 mol% cholesterol; (c) liquid ordered phase (L_o) enriched in cholesterol with 40 mol% cholesterol; and (d) liquid disordered phase (L_d) at all concentrations of 6-kc.

Sterol (mol %)	Cholesterol-DMPC		6-ketocholestanol-DMPC	
	$\vec{F}_d$ (MV/cm)	$\Delta\nu_{obs}$ (cm^{-1})	$\vec{F}_d$ (MV/cm)	$\Delta\nu_{obs}$ (cm^{-1})
0	10.3 ± 20	2.59 ± 0.08	10.3 ± 19	2.6 ± 0.2
5	11.1 ± 21	2.79 ± 0.01	11.0 ± 21	2.8 ±0.1
10	10.9 ± 16	2.85 ± 0.03	11.4 ± 21	2.85 ± 0.04
15	9.9 ± 16	2.80 ± 0.02	11.3 ± 21	2.83 ± 0.01
20	9.7 ± 14	2.75 ± 0.02	17.8 ± 3	2.86 ± 0.07
25	9.2 ± 14	2.62 ± 0.02		
30	6.6 ± 8	2.53 ± 0.02	18.2 ± 3	2.9 ± 0.2
40	6.2 ± 8	2.37 ± 0.07	13.2 ± 20	3.03

Table 5.1: Experimentally measured differences in nitrile's absorption energy ($\Delta\nu_{obs}$) when moved from αLAX(25) to αLAX(16), and the associated dipole field ($\vec{F}_d$) calculated using Equation 1 for DMPC vesicles containing varying concentrations of sterol and 1 mM peptide. Error in $\Delta\nu_{obs}$ represents one standard deviation of at least three experimental measurements. Error in $\vec{F}_d$ is propagated from $\Delta\nu_{obs}$ and the range of nitrile angles are calculated from MD simulations. The large magnitude of this error reflects the width of the angle distribution from MD simulations.

5.8 REFERENCES

1. van Meer, G. Lipid traffic in animal cells. *Annu. Rev. Cell. Biol.* **1989**, *5*, 247-275.
2. Léonard, A.; Dufourc, E. J. Interactions of Cholesterol with the Membrane Lipid Matrix. A Solid State NMR Approach. *Biochimie* **1991**, *73*, 1295-1302.
3. Jacobs, R.; Oldfield, E. Deuterium Nuclear Magnetic Resonance Investigation of Dimyristoyllecithin-Dipalmitoyllecithin and Dimyristoyllecithin-Cholesterol Mixtures. *Biochem* **1979**, *18*, 3280-3285.
4. Veatch, S. L.; Polozov, I. V.; Gawrisch, K.; Keller, S. L. Liquid Domain in Vesicles Investigated by NMR and Fluorescence Microscopy. *Biophys. J.* **2004**, *86*, 2910-2922.
5. Bin, X.; Lipkowski, J. Electrochemical and PM-IRRAS Studies of the Effect of Cholesterol on the Properties of the Headgroup Region of a DMPC Bilayer Supported at a Au(111) Electrode. *J. Phys. Chem. B* **2006**, *110*, 26430–26441.
6. Shimshick, E. J.; McConnel, H. M. Lateral Phase Separations in Binary-Mixtures of Cholesterol and Phospholipids. *Biochem. Biophys. Res. Commun.* **1973**, *53,* 446-451.
7. Oldfield, E.; Chapman, D. Effects of Cholesterol and Cholesterol Derivatives on Hydrocarbon Chain Mobility in Lipids. *Biochem. Biophys. Res. Commun.* **1971,** *43*, 610-616.
8. Mainali, L.; Raguz, M.; Subczynski, W. K. Formation of Cholesterol Bilayer Domains Precedes Formation of Cholesterol Crystals in

Cholesterol/Dimyristoylphosphatidylcholine Membranes: EPR and DSC Studies. *J. Phys. Chem. B.* **2013,** *117,* 8994-9003.

9. Mabrey, S.; Sturtevant, J. M. Investigation of Phase Transitions of Lipids and Lipid Mixtures by High Sensitivity Differential Scanning Calorimetry. *Proc. Natl. Acad. Sci. USA*. **1976,** *73*, 3862–3866.
10. Blandamer, M. J.; Briggs, B.; Cullis, P. M.; Rawlings, B. J.; Engberts, J. B. F. N. Vesicle-Cholesterol Interactions: Effects of Added Cholesterol on Gel-to-Liquid Crystal Transitions in a Phospholipid Membrane and Five Dialkyl-based Vesicles as Monitored Using DSC. *Phys. Chem. Chem. Phys.* **2003**, *5*, 5309-5312
11. McMullen, T. P. W.; McElhaney, R. N. New Aspects of the Interaction of Cholesterol with Dipalmitoylphosphatidylcholine Bilayers as Revealed by High-Sensitivity Differential Scanning Calorimetry. *Biochim. Biophys. Acta.* **1995**, *1234*, 90-98.
12. McMullen, T. P. W.; Lewis, R. N. A. H.; McElhaney, R. N. Cholesterol–Phospholipid Interactions, the Liquid-Ordered Phase and Lipid Rafts in Model and Biological Membranes. *Curr. Opin. Colloid Interface Sci.* **2004**, *8*, 459–468.
13. Efimova, S. S.; Ostroumova, O. S. Effect of Dipole modifiers on the Magnitude of the Dipole Potential of Sterol-Containing Bilayers. *Langmuir* **2012,** *28,* 9908-9914
14. Haldar, S.; Kanaparthi, R. K.; Samanta, A.; Chattopadhyay, A. Differential Effect of Cholesterol and Its Biosynthetic Precursors on Membrane Dipole Potential. *Biophys. J.* **2012,** *102,* 1561-1569.

15. Starke-Peterkovic, T.; Turner, N.; Vitha, M. F.; Waller, M. P.; Hibbs, D. E. Cholesterol Effect on the Dipole Potential of Lipid Membranes. *Biophys. J.* **2006,** *90,* 4060-4070.

16. Szabo, G. Dual Mechanism for the Action of Cholesterol on Membrane Permeability. *Nature.* **1974**, *252*, 47–49.

17. McIntosh, T. J., Magid, A. D.; Simon, S. A. Cholesterol Modifies the Short-range Repulsive Interactions Between Phosphatidyl- choline Membranes. *Biochem.* **1989**, *28*, 17–25.

18. Hofsäβ, C.; Lindahl, E.; Edholm, O. Molecular Dynamics Simulations of Phospholipid Bilayers with Cholesterol. *Biophys. J.* **2003**, *84*, 2192-2206.

19. Smondyrev, A. M.; Berkowitz, M. L. Structure of Dipalmitoylphosphatidylcholine/Cholesterol Bilayer at Low and High Cholesterol Concentrations: Molecular Dynamics Simulation. Biophys. J. **1999**, *77*, 2075-2089.

20. Chiu, S. W.; Jakobsson, E.; Scott, H. L. Combined Monte Carlo and Molecular Dynamics Simulation of Hydrated Dipalmitoyl–phosphatidylcholine–Cholesterol Lipid Bilayers. *J. Chem. Phys.* **2001**, *114*, 5432-5443.

21. Gabdoulline, R. R.; Vanderkooi, G.; Zheng, C. Comparison of the Structures of Dimyristoylphosphatidylcholine in the Presence and Absence of Cholesterol by Molecular Dynamics Simulations. *J. Phys. Chem.* **1996**, *100*, 15942-15946.

22. Yang, Y.; Mayer, K. M.; Wickremasignhs, N. S.; Hafner, J. H. Probing the Lipid Membrane Dipole Potential by Atomic Force Microscopy. *Biophys. J.* **2008**, *95*,

5193-5199.

23. Franklin, J. C.; Cafiso, D. S. Internal Electrostatic Potentials in Bilayers: Measuring and Controlling Dipole Potentials in Lipid Vesicles. *Biophys. J.* **1993**, *65*, 289-299.
24. Gross, E.; Bedlack, R. S.; Loew, L. M. Dual-Wavelength Ratiometric Fluorescence Measurement of the Membrane Dipole Potential. *Biophys. J.* **1994**, *67*, 208-216.
25. Haldar, S.; Kanaparthi, R. K.; Samanta, A.; Chattopadhyay, A. Differential Effect of Cholesterol and Its Biosynthetic Precursors on Membrane Dipole Potential. *Biophys. J.* **2012**, *102*, 1561-1569.
26. Efimova, S. S.; Ostroumova, O. S. Effect of Dipole Modifiers on the Magnitude of the Dipole Potential of Sterol-Containing Bilayers. *Langmuir* **2012**, *28*, 9908-9914.
27. Smondyrev, A. M.; Berkowitz, M. L. Effects of Oxygenated Sterol on Phospholipid Bilayer Properties: a Molecular Dynamics Simulation. *Chem. Phys. Lipids*. **2001**, *112*, 31-39.
28. Simon, S. A.; McIntosh, T. J.; Magid, A. D.; Needham, D. Modulation of the Interbilayer Hydration Pressure by the Addition of Dipoles at the Hydrocarbon/Water Interface. *Biophys. J.* **1992**, *61*, 786–799.
29. Duffin, R. L.; Garrett, M. P.; Flake, K. B.; Durrant, J. D.; Busath, D. D. Modulation of Lipid Bilayer Interfacial Dipole Potential by Phloretin, RH421, and

6-ketocholestanol as Probed by Gramicidin Channel Conductance. *Langmuir* **2003,** *19*, 1439–1442.

30. Johansson, A. C. V.; Lindahl, E. Amino-Acid Solvation Structure in Transmembrane Helices from Molecular Dynamics Simulations. *Biophys. J.* **2006**, *91*, 4450-4463.
31. Kelly, S. M.; Price, N. C. The Use of Circular Dichroism in the Investigation of Protein Structure and Function. *Current Protein and Peptide Science.* **2000**, *1*, 349-384.
32. Hu, W.; Webb, L. J. Direct Measurement of the Membrane Dipole Field in Bicelles Using Vibrational Stark Effect Spectroscopy. *J. Phys. Chem. Lett.* **2011**, *2*, 1925-1930.
33. Shrestha, R.; Cardenas, A. E.; Elber, R.; Webb, L. J. Measurement of the Membrane Dipole Electric Field in DMPC Vesicles Using Vibrational Shifts of *p*-Cyanophenylalanine and Molecular Dynamics Simulations. *J. Phys. Chem. B.* **2015**, *119*, 2869-2876.
34. Getahun, Z.; Huang, C. Y.; Wang, T.; DeLeon, B.; DeGrado, W. F.; Gai, F. Using Nitrile-Derivatized Amino Acids as Infrared Probes of Local Environment. *J. Am. Chem. Soc.* **2003**, *125*, 405–411.
35. Kučerka, N.; Nieh, M. P.; Katsaras, J. Fluid Phase Lipid Areas and Bilayer Thicknesses of Commonly Used Phosphatidylcholines as a Function of Temperature. *Biochim. Biophys. Acta.* **2011**, *1808*, 2761-2771.
36. Khelashvili, G.; Pabst, G.; Harries, D. Cholesterol Orientation and Tilt Modulus

in DMPC Bilayers. *J. Phys. Chem. B.* **2010**, *114*, 7524-7534.

37. Rog, T.; Pasenkiewicz-Gierula, M. Cholesterol Effects on the Phosphatidylcholine Bilayer Nonpolar Region: A Molecular Simulation Study. *Biophys. J.* **2001**, *81*, 2190-2202.
38. Jedlovszky, P.; Mezei, M. Effect of Cholesterol on the Properties of Phospholipid Membranes. 1. Structural Features. *J. Phys. Chem. B.* **2003***, 107*, 5311-5321.
39. Henriksen, J.; Rowat, A. C.; Brief, E.; Hsueh, Y. W.; Thewalt, J. L.; Zuckermann, M. J.; Ipsen, J. H. Universal Behaviour of Membranes with Sterols. *Biophys. J.* **2006**, *90*,1639-1649.
40. Smaby, J. M.; Momsen, M.; Brockman, H. L.; Brown, R. E. Phosphatidylcholine Acyl Unsaturation Modulates the Decrease in Interfacial Elasticity Induced by Cholesterol. *Biophys. J.* **1997**, *73*, 1492-1505.
41. Marsh, D.; Smith, I. C. P. Interacting Spin Labels as Probes of Molecular Separation within Phospholipid Bilayers. *Biochem. Biophys. Res. Commun.* **1972**, *49*, 916-922.
42. Kusumi, A.; Tsuda, M.; Akino, T.; Ohnishi, S.; Terayama, Y. Protein-Phospholipid-Cholesterol Interaction in the Photolysis Invertebrate Rhodopsin. *Biochem.* **1983**, *22*, 1165-1170.
43. Mouritsen, O. G.; Jørgensen, K. Dynamical Order and Disorder in Lipid Bilayers. *Chem. Phys. Lipids.* **1994**, *73*, 3-25.
44. McConnell, H. M.; Radhakrishnan, A. Condensed Complexes of Cholesterol and Phospholipids. *Biochim. Biophys. Acta.* **2003**, *1610*, 159-173.

45. Ohvo-Rekila, H.; Ramstedt, B.; Leppimaki, P.; Slotte, J. P. Cholesterol Interactions with Phospholipids in Membranes. *Prog. Lipid Res.* **2002**, *41*, 66-97.

46. Rheinstadter, M. C.; Mouritsen, O. G. Small-Scale Structure in Fluid Cholesterol-Lipid Bilayers. *Curr. Opin. Colloid Interface Sci.* **2013***, 18*, 440-447.

47. de Meyer, F.; Smit, B. Effect of Cholesterol on the Structure of a Phospholipid Bilayer. *PNAS*. **2009**, *106*, 3654-3658.

48. Ipsen, J. H.; Karlstrom, G.; Mouritsen, O. G.; Wennerstrom, H.; Zuckermann, M. J. Phase Equilibria in the Phosphatidylcholine-Cholesterol system. *Biochim. Biophys. Acta.* **1987**, *905*, 162-172.

Chapter 6 Unassisted Transport of Tryptophan Across a Lipid Bilayer

This chapter is adapted from the publication[2], Membrane Permeation of Peptide: It Is Better To Be Positive published in The Journal of Physical Chemistry B on May 05, 2015. The author's contribution to this publication is the collection of experimental data and preparation of the section under the heading Fluorescence Spectroscopy.

6.1 INTRODUCTION

Lipid bilayers provide barrier to the free diffusion of solutes such as ions, small amino acids, phosphates, water molecules and even proteins, maintaining a different environment inside and outside the cell. Selective solutes can (1) diffuse through a membrane either via carrier proteins, channels and pumps or (2) permeate directly through the membrane maintaining an electric field across biological membranes. This field is vital and living systems invest significant biological machinery (pumps) and energy to maintain it.[1] It is therefore of considerable interest to quantify the rate of ion "leakage" through membranes, i.e. the rate in which ions permeate through biological membranes without assistance. It is against this leakage that the cell must continuously struggle and pump back ions, a struggle that will stop only at the cell death.

The permeation rate depends on numerous properties such as size and charge of the permeant, pH of the surrounding and so on.[2,3,4] When considering permeation through membranes of complex molecules it is difficult to separate the impact of charge from

[2] Cardenas, A. E.; Shrestha, R.; Webb, L. J.; Elber, R. Membrane Permeation of a Peptide: It Is Better to be Positive. *J. Phys. Chem. B* **2015**, *119*, 6412-6420.

variations in molecular size and flexibility. The permeation mechanism that prefers positively charged amino acids versus negatively charged residues is not so clear.

If we use the simplest model of a membrane as a thin hydrophobic layer in aqueous solution, we expect the membrane to be non-selective to any particular charge. However, there has been considerable number of experimental and theoretical studies illustrating selectivity of charges by membrane. For example, Clarke[5] argued that a dipole electric field across the membrane assists the permeation of a particular type of charged systems, namely organic ions.[6] He made a reference to interesting experiments comparing the permeation of aromatic charges tetraphenylborate and tetraphenylphophonium.[7] The experiment by Liberman and Topaly suggests that the partition coefficients of the anions in the membrane are 10^5 times larger than the partition coefficients of the cations. These two ions have comparable sizes but opposite charges, and hence the suggestion that the prime force controlling the difference in their permeation rates must be electrostatic. Clarke proposed a mechanism for this surprising phenomenon and attributed the differences to favorable interactions of the membrane dipole moment with anions.[5]

There are several questions that the Clarke model raises that we address in this manuscript: (i) Is the electric field of pure membrane indeed following the Clarke prediction (i.e., more favorable for negative ions), and if yes, why and what is its origin? (ii) Is the model that successfully explained the permeation of organic ions applicable to more typical biological molecules such as peptides? (iii) Are there alternative molecular mechanisms favoring different charge permeation?

One of the popular amino acids found to permeate membranes is arginine, which is positively charged at variance with Clarke arguments. Permeations of arginine amino acids or side chains were illustrated computationally and experimentally.[8-12] On the other hand, arginine experiments are not necessarily a measure of charge effect on permeation. For example, it is possible that the long hydrophobic chain of arginine facilitates its permeation and not necessarily the charge, which is the focus of our discussion here. What we miss in this case is a comparative study to an anion with similar structural features to arginine.

To address this question we investigated the time scale and mechanism of unassisted permeation of simple peptide molecule: a zwitterionic amino acid, Tryptophan across a model membrane composed of 1,2–dioleoyl-sn-glycerol-3-phosphocholine (DOPC) lipids under different pH conditions and temperature. The choice of tryptophan for this experiment was motivated by its abundance in membrane proteins as an interfacial anchor and the ease of its detection by spectroscopic means. Variation of pH does not significantly affect the shape of this single amino acid. However, it impacts the charge. At low pH values, the N-terminal is mostly positively charged while the C-terminal is neutral. At moderate biological pH, tryptophan is zwitterionic and at high pH, the C-terminal is mostly negatively charged. We used fluorescence spectroscopy experiments and simulations to measure the rate of permeation of a single amino acid tryptophan through DOPC vesicles. In the simulations we assumed that the prime effect of the change in pH is to modify the charges of the zwitterionic amino acid and not the

charges on the lipid head group. Both simulations and experiments indicate that it is the positively charged ion of the tryptophan species that permeates through the membrane most efficiently. The result adds insight to understanding the transport mechanism of such molecules, which takes us a step closer in successfully designing membrane proteins.

6.2 Results and Discussion

The prime goal of our collaborative work was to examine mechanisms of passive transport of charged and moderately complex molecules through membrane. The questions that we addressed are: (i) Is the permeation through the hydrophobic core of the membrane bilayer possible at all at reasonable conditions? We illustrate below that such permeation is measurable experimentally at the minute to hour time scale and is feasible according to computer simulations. Therefore we continue to ask: (ii) Given that the overall shape of the permeant is fixed and only the charge is changing, what is the impact of charge variation on the permeability? Finally, (iii) What is the molecular mechanism of the passive permeation of these charged molecules?

6.2.1 Fluorescence Spectroscopy

We determined the concentration of tryptophan molecules trapped inside the lipid vesicles using tryptophan fluorescence measured at an excitation wavelength of 280 nm and emission wavelength of 348 nm. Recall that the experiments first place the phospholipid vesicles in tryptophan solution, allowing the solute to permeate the

membrane for a fixed period of time. The external solution is then washed away and the amount of permeating tryptophan is assessed from its fluorescence intensity in units of nanomoles (nmol). Figure 6.1 shows the measurements of tryptophan permeation as a function of time for different pH conditions. While the measurement time scale is rather slow on the molecular time scale (minutes and hours) and it is difficult to resolve the initial rise of tryptophan concentration in the DOPC vesicles, the differences in the long time amplitudes are obvious. It is clear that at low values of pH we obtain a significantly larger amount of positively charged tryptophan molecules (black diamonds) permeating to the vesicle than for the zwitterionic (yellow diamonds) or negatively charged peptide (blue diamonds).

The experimental permeation curves in Figure 6.1 show the impact of the pH on the permeation rates. The number of permeating molecules (the amplitude of the kinetic curve) is significantly affected by the charge state. Figure 6.1 clearly illustrates more efficient permeation to the vesicle by a positively charged tryptophan solution. This is in contrast with the prediction of the theory on membrane electric dipole by Clarke[5] and in agreement with simulations and experiments on arginine residues[5,6,8] and CPP[13,14]. Nevertheless, the data is noisy and the rapid rise at early times on the experimental time scale makes it difficult to determine if the kinetics are exponential and, if it is exponential, what is the value of the rate coefficient.

To test the sensitivity of the results to buffer conditions, we repeated the experiments by halving the concentrations of the buffer while keeping the system at the same pH (Figure 6.2). The ionic strength influences permeation in a complex way. When

the ionic strength decreases, it makes permeation slower for pH 2.4 and faster at pH 5.5. Our analysis focuses on the undiluted data for which the results are less noisy. The main conclusion of the paper that the positively charged species is permeating faster remains unaffected.

Despite these difficulties, we have attempted to quantitatively model the experimental data. We make the following assumptions to simplify the analysis and reduce the number of parameters required: (i) The changes in the pH influence only the tryprophan charge and not other features of the system (e.g. the overall structure of the membrane is not affected). (ii) The permeant species is primarily the positively charged tryptophan. The last assumption is motivated by the experimental observation showing significantly large permeability at low pH but little variation in the rate coefficient at different pH as estimated by an exponential fit of the experimental curves. The second assumption is also supported by the simulation results that predict that only the positive species is permeating (see next section). The equations below of mass balance and pH impact on permeation are similar to the discussion by Cullis et al.[15] however they did not consider the permeation dependence on the type of the charge.

At any pH the total concentration of the tryptophan molecules is a combination of three species: $\left[TRP\right]=\left[P^{+}\right]+\left[N^{-}\right]+\left[Z^{+/-}\right]$, where $\left[P^{+}\right]$ is the protonated, low pH, positively charged species, $\left[N^{-}\right]$ is the high pH, negatively charged species, and $\left[Z^{+/-}\right]$ is the zwitterion form. The equilibrium relationships in aqueous solution between the three species are given by

$$P^+ \Leftrightarrow Z^{+/-} + H^+ \qquad K_1 = \frac{\left[Z^{+/-}\right]\left[H^+\right]}{\left[P^+\right]} \qquad K_1 = 4.17 \times 10^{-3}$$

$$Z^{+/-} \Leftrightarrow N^- + H^+ \qquad K_2 = \frac{\left[N^-\right]\left[H^+\right]}{\left[Z^{+/-}\right]} \qquad K_2 = 4.07 \times 10^{-10} \qquad (6\text{-}1)$$

Using the second assumption that the dominant permeating species is the positively charged ion $\left[P^+\right]$ we can write an equation for the kinetic of change of the tryptophan concentration outside of the vesicle

$$\frac{d\left[TRP\right]}{dt} = \frac{d\left[P^+\right]}{dt} \qquad (6\text{-}2)$$

Let the volume of the experimental apparatus be V. The total number of tryptophan molecules is $N = \left[TRP\right] \cdot V$. One definition of the permeability coefficient (P) is

$$\frac{d\left[TRP\right] \cdot V}{dt} = -PA\left(\left[P^+\right] - \left[P^+_{inside}\right]\right) \qquad (6\text{-}3)$$

where A is the total accumulated surface areas of all the vesicles in solution. Initially the concentration inside the vesicle of the positively charged species, $\left[P^+_{inside}\right]$, is zero as we focus on the initial rate. At low pH values the concentration of the negatively charged species is negligible (Equation 6-1) we can therefore write for the initial rate at low pH

$$\left[TRP\right] \cong \left[P^+\right] + \left[Z^{+/-}\right] = \left[P^+\right] + \frac{K_1\left[P^+\right]}{\left[H^+\right]} \qquad \left[P^+\right] = \frac{\left[TRP\right]}{\left(1 + K_1 / \left[H^+\right]\right)}$$

Substituting in the expression for the rate we identify the apparent rate coefficient, k, which is measured experimentally and its relationship to the permeability coefficient, P.

$$\frac{d[TRP]}{dt} = -\frac{PA}{V} \cdot \frac{[H^+]}{[H^+] + K_1}[TRP] = -k[TRP]$$

$$P = \frac{kV}{A}\left(1 + \frac{K_1}{[H^+]}\right) \qquad (6\text{-}4)$$

We now extract from the experiment an estimate of the permeation coefficient. The rate coefficient at pH 2.4 is $k \cong 0.022/60$ s^{-1}. We consider the low pH results for our fit due to significantly lower error bars compared to other pH measurements. The total volume of the prepared solution is 400 dm^3. This solution includes 1.81×10^{19} DOPC molecules. The total surface area of these lipid molecules, exposed to the external solvent, is $72.1\times(1.81\times\times10^{19})\times(10^{-16})/2 = 65{,}250.5$ cm^2 where 72.1 $Å^2$ is the surface area of a single head[17]. Assuming that all the DOPC molecules are incorporated in vesicles and substituting in the expression for the permeation coefficient (Equation 6-4) we have for pH 2.4

$$P \cong \frac{0.022\times300}{60\times65{,}250.5}\left(1 + \frac{4.17\times10^{-3}}{10^{-2.4}}\right) = 3.45\times10^{-6} \text{ cm/s} \qquad (6\text{-}5)$$

6.2.2 Molecular Dynamic Simulations

Figure 6.3 shows the potential of mean force for permeation of different ionic species of tryptophan molecules through the DOPC bilayer membrane. The origin (Z = 0) is the center of the membrane. For all species, the barrier for permeation is located at the

center of the membrane. This barrier is significantly larger for the permeation of the negatively charged tryptophan and the zwitterionic molecule compared to the positively charged species. This is in qualitative agreement with the reported experimental observation. For the positively charged species the barrier at the center is about 10 kcal/mole lower and the barrier is even smaller for the permeation of a neutral tryptophan molecule. These free energy profiles also show that the positively charged tryptophan binds more strongly to the membrane (with a minimum at a location 14 Å away from the membrane center) than the other species. This binding interaction is very weak for the negatively charged tryptophan. Weaker binding of anions compared to cations has been observed before in constrained simulations. An example is binding to the surface of the membrane by sodium and chloride ions[16] or the permeation of these ions through the membrane.[17-19] Recent experiments and simulations suggest a similar membrane binding for both atomic ions.[20] The barrier for permeation measured from the binding locations in the membrane is 12.4 ± 0.7, 20.7 ± 0.7, 26.0 ± 0.9 and 29.2 ± 0.1 kcal/mol for the neutral, positively charged, negatively charged and zwitterionic tryptophan species, respectively.

Since the equilibrium free energy profiles are not easy to measure we estimate below the value of the permeation coefficients that is frequently determined experimentally.[21]

Table 6.1 shows the permeability coefficient for the three charged molecules of tryptophan computed with the solubility-diffusion model:[22,23]

$$P = \left(\int_{z_1}^{z_2} \frac{\exp\left(\beta \Delta G(z)\right)}{D(z)} dz \right)^{-1} \tag{6-6}$$

where $D(z)$ is a position dependent diffusion coefficient for the permeant along the membrane axis z, that we computed from our simulations using

$$D(z) = \frac{(RT)^2}{\int_0^\infty \left\langle \Delta F_z(z,t) \Delta F_z(z,0) \right\rangle dt} \tag{6-7}$$

with $\Delta F_z(z,t)$ the instantaneous deviation of the constrained force $F_z(z,t)$ from the average force $\left\langle F_z(z) \right\rangle$.

Table 6.1 shows that the permeability coefficients for the zwitterionic and negatively charged tryptophan are very low with values similar to the permeabilities estimated previously for other ionic species.[24-26] In contrast the permeability of the positively charged tryptophan is 9 orders of magnitude larger. Assuming that these charged species do not change their protonation state during insertion and diffusion through the membrane, those permeability estimates suggest that the only molecule that can move through the membrane is the positively charged tryptophan.

To assess the computed values we compared values of the diffusion constant to other reported values. Landolt-Börnstein reported a value of 0.66×10^{-5} cm^2/s for tryptophan in water.[27] Mark and Nilsson[28] found the diffusion coefficient for tryptophan in water to be in the range 13×10^{-5} cm^2/s and 4×10^{-5} cm^2/s. Our computations estimate diffusion coefficients in water as 6×10^{-5} cm^2/s and 8×10^{-5} cm^2/s for the positively and

negatively charged species. Hence, our simulations are similar to other calculations and are about an order of magnitude faster than experimental measurement. These deviations are quite typical in the field.

What is the mechanism that makes the permeation of the positively charge tryptophan so different compared to the permeation of the other two charged species? To answer this question we consider the changes of membrane structure that occur when any of the three species; positively charged, neutral and negatively charged tryptohan are close to the membrane center (Figures 6.4 – Figure 6.6). For all permeants we observe a defect of water permeation that accompanies the permeant and is widely known in the field of permeant-membrane interactions.[8,24-25] Significant variation in the sizes and characteristics of the defects is found for the tryptophan species. When the zwitterionic and negatively charged molecules are closer to the membrane center, up to fifteen water molecules accompany the permeant to compensate for the huge energetic penalty of having those charged species in the hydrophobic core of the membrane (Figures 6.4 and Figure 6.5). On average, only six water molecules follow the positive species, suggesting a smaller water perturbation.

Some modifications to the membrane structure are also observed. For example for the negatively charged species, and with less extent for the zwitterionic moiety, one choline group attempts to approach the permeant located at the center of the membrane (Figure 6.5a and Figure 6.5b). Since the choline is right at the top of the DOPC molecule the potential interruption to the membrane structure is significant and is very rare (see also Figure 6.5c). The membrane perturbation is different when the positively charged

tryptophan is closer to the membrane center. In this case usually two phosphate groups (that are more centered compared to the choline group) remain closer to the permeant as well as accompanying glycerol groups that surround the positively charged amino group (Figures 6.5c, Figure 6.6a, and Figure 6.6b) and help stabilize the ion. Hence, rather than deformation of mostly membrane components which is induced by a positive permeant (sliding of phosphate and glycerol groups towards the center), a negative or zwitterion permeant requires membrane disruption and the entry of a significant number of water molecules for charge compensation. The last is illustrated to be more costly by the PMF calculations (Figure 6.3).

The membrane distortions observed in the simulations modify the electrostatic interactions felt by the charged permeants. Figure 6.7 shows the electrostatic energy of the charged permeant while it moves across the membrane axis. For the positively charged tryptophan the electrostatic interaction is favorable when the permeant moves inside the membrane due to attractive interactions with several phosphate and glycerol groups (Figure 6.5 and Figure 6.6). Closer to the membrane center, contacts with those charged and polar groups become more difficult and the energy increases. Contrasting with these results, a negatively charged tryptophan feels an increasing unfavorable energy moving to the membrane center after it crosses the area where the positive charged choline groups are located (about 20–24 Å from the membrane center). This suggests that the membrane distortions that would be required to compensate for the electrostatic penalty for the permeation of this negative ion, specifically the approach of several

choline groups is more costly than the observed approach of phosphate and glycerol groups to interact with a positively charged tryptophan.

We expect that a neutral permeant will perturb the membrane less. We therefore also consider membrane perturbation by a neutral, uncharged tryptophan. To examine the impact of membrane structure on permeation of charged species we replace the uncharged tryptophan in the MD sampled structures by the charged species and compute the electric field experienced by the permeant. The results are also reported in Figure 6.7. The electrostatic energy as a function of the membrane depth of the permeant has similar but weaker trends compared to the energy profiles sampled in simulations of charged species permeation. Interestingly when unperturbed membrane is considered (i.e. membrane without a permeant) and an ion is simply placed at different membrane positions along the normal, the electrostatic energy flips. Negatively charged ions are preferred by the unperturbed membrane in accord with Clarke's argument. Previous simulations studies of pure lipid bilayers[29-31] have shown that this preference is due to the positive potential contribution of the oriented water molecules located at the membrane/water interface that over-compensate the negative potential contribution of the lipid head groups. Hence, it is the membrane distortion induced by the permeant that selects positively charged ions.

6.3 CONCLUSION

In this paper we illustrate, using a combination of experiments and simulations, the high efficiency of permeation of positively charged peptides compared to negatively

charged ions or to zwitterions. This observation is surprising given the overall hydrophobic structure of membrane moiety that has no significant electrostatic interactions. Furthermore, this observation is also in disagreement with earlier investigations of transport of organic ions that suggest anions as the better permeating species. An explanation to this challenge is provided by detailed analysis of the MD simulations, results that are also consistent with the experiments we have conducted.

We have shown that permeation is enhanced by defect formation in the membrane. The positively charged permeants effectively pull the negatively charged phosphate and the polar glycerol groups in the direction of the membrane center. The last two groups ease the electrostatic self-energy felt by the permeant in the low dielectric environment. In contrast negatively charged ions are less successful in pulling the (further away) positively charged choline groups. To compensate the high self-energy in the low dielectric environment anions induce membrane disruption and gather a significant number of water molecules around them. The disruption is significantly more costly in energy than the internal membrane distortion found for cations. We note that if the membrane is unperturbed a reverse trend is obtained; negative ions are more permeable than positive ions. This explains why organic anions, which are likely to have a small effect on the hydrophobic core of the membrane, translocate better than organic cations. It will be of considerable interest to conduct additional experiments with one of the peptide ends blocked reducing the impact of very different pH's on the environment.

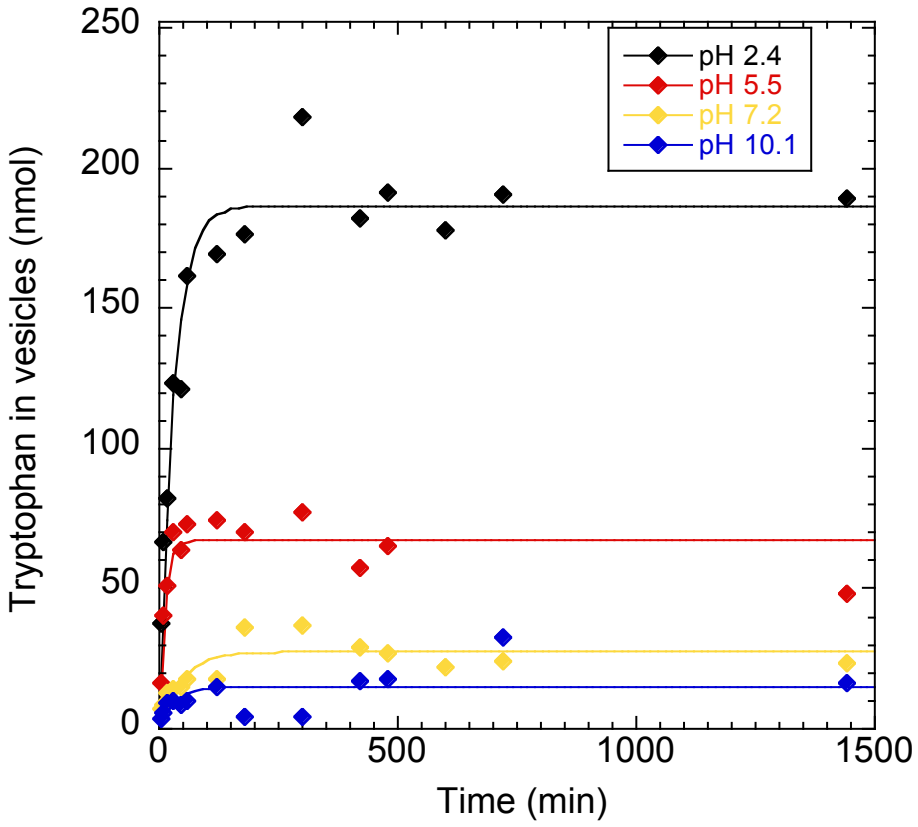

Figure 6.1: Permeation of tryptophan through DOPC membrane under different pH conditions. It is evident that the amount of tryptophan released is the highest at low pH levels, suggesting that permeation at low pH and positive charge is faster. The solid lines are exponential fittings to the experimental data points.

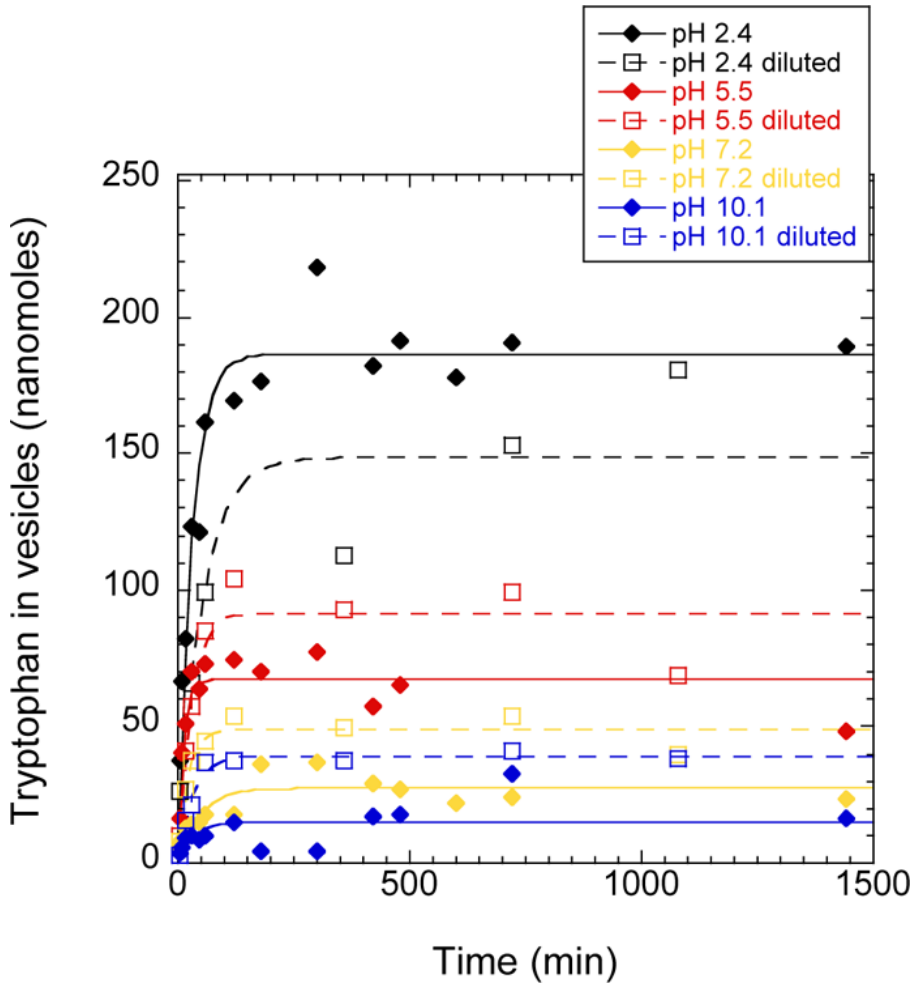

Figure 6.2: Permeation of tryptophan through a DOPC membrane under different pH conditions. It is evident that the amount of tryptophan released is the highest at low pH levels, suggesting that permeation at low pH and positive charge is fastest. The unfilled squares are the results of experiments conducted with diluted buffer. See text for more details. The solid and dashed lines are exponential fittings to the experimental data points for undiluted and diluted buffers, respectively.

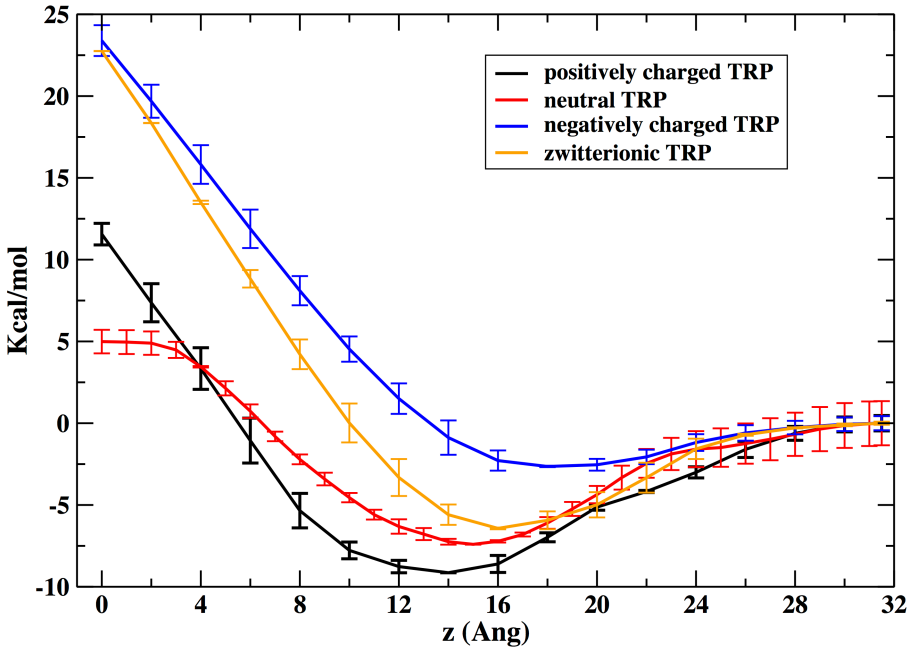

Figure 6.3: Free energy profile for the penetration of the different tryptophan species as a function of distance from the membrane center. Error bars are estimated by computing the energies for the two leaflets of the bilayer. The energies are shifted so they are zero farther away from the membrane.

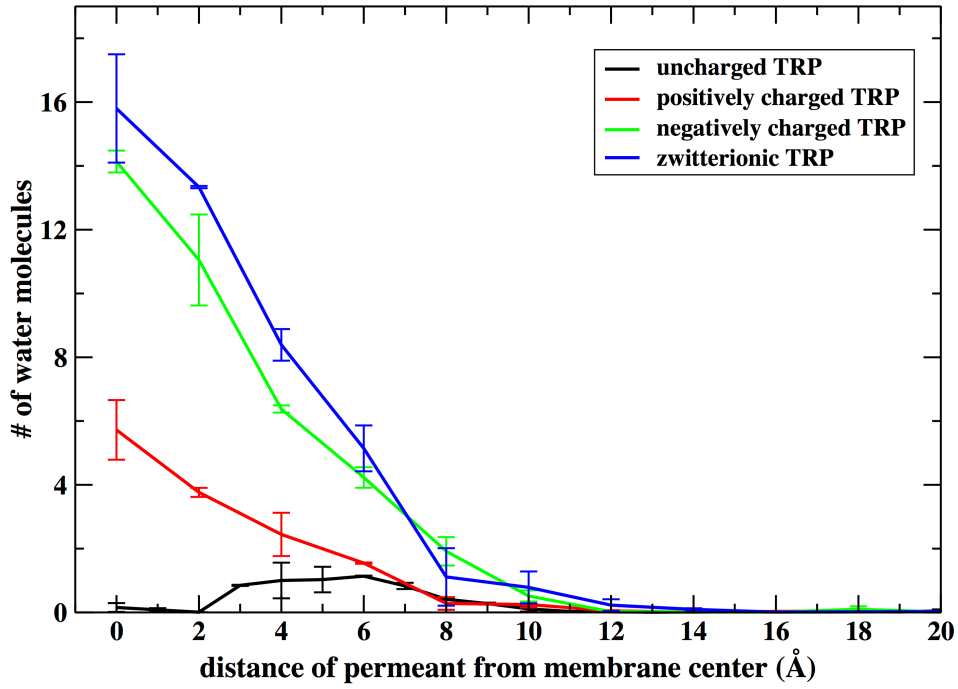

Figure 6.4: Number of water molecules that come closer than 10 Å from the membrane center plotted as a function of the location of the respective permeant. More than twice the number of water molecules penetrates to the membrane hydrophobic core when the zwitterionic or negatively charged tryptophan molecules are deeper inside the membrane compared to the water penetration for the positively charged tryptophan. In contrast, when an uncharged tryptophan is at the membrane center, water molecules remain away from that region. This observation suggests a significantly less disruptive permeation for the neutral and positively charged species compared to the negative ions and zwitterions.

(a)

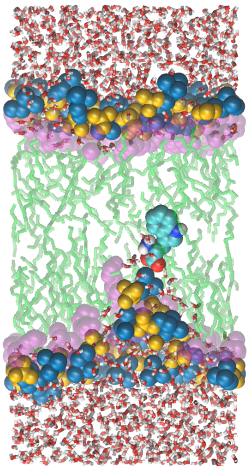

(b)

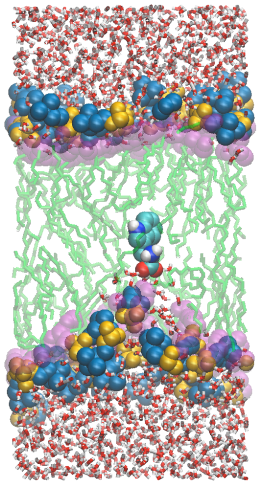

(c)

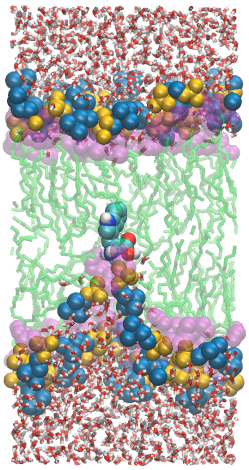

Figure 6.5: Representative molecular snapshots for a zwitterionic (a), negatively charged (b) and positively charged (c) tryptophan inserted in the middle of the membrane. A space filled representation is used for the tryptophan (with carbon atoms in cyan, oxygen in red, nitrogen in blue and hydrogen in light gray), the phosphate (yellow), the choline (dark blue) and the glycerol (clear purple) groups of the lipid molecules. The hydrophobic lipid tails are colored in green and the water atoms at the top and bottom are in red and light gray. See text for more details. These molecular snapshots were prepared with the program VMD.[32]

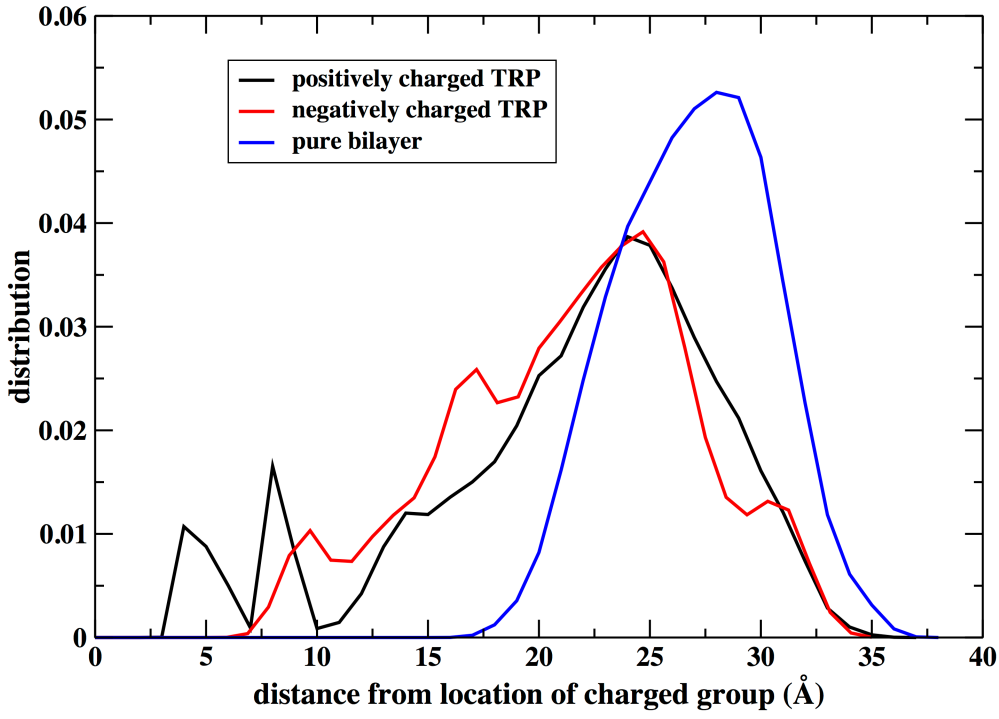

(a)

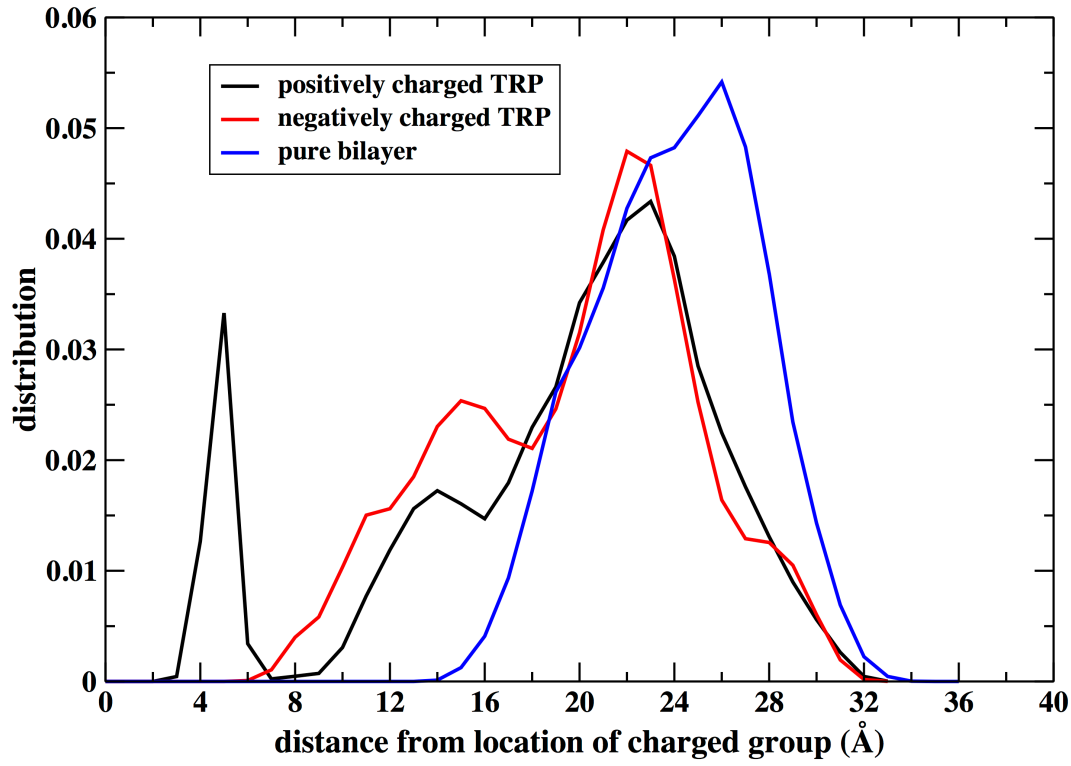

(b)

Figure 6.6 continued on the next page.

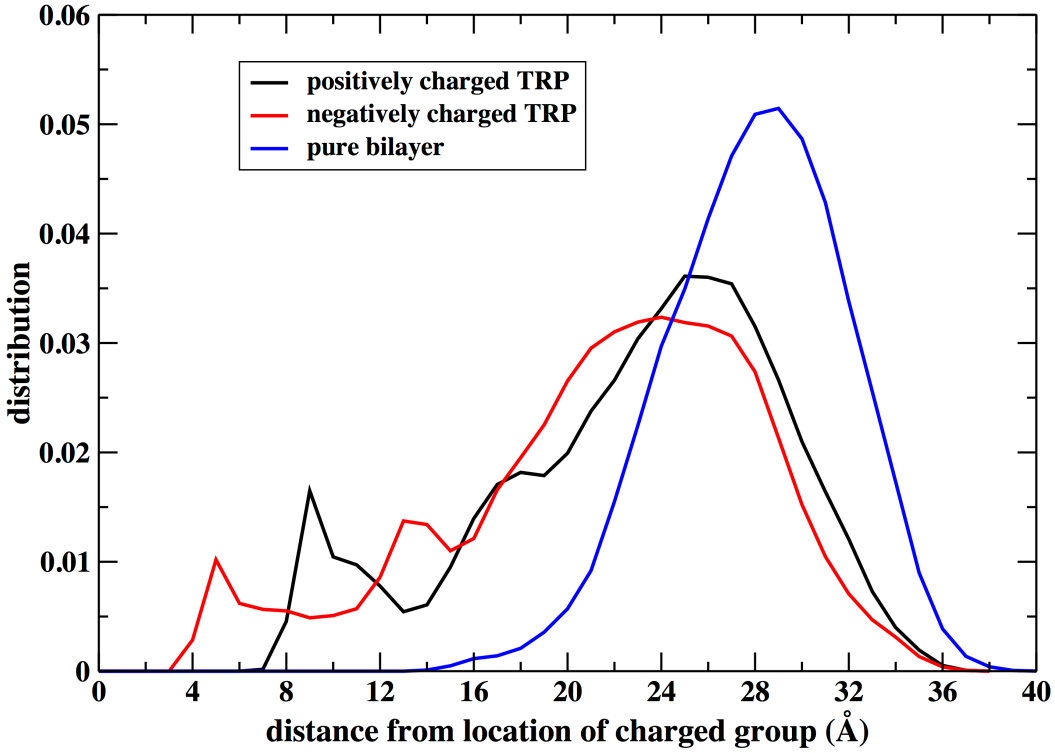

(c)

Figure 6.6: Radial distribution functions for (a) phosphate, (b) glycerol and (c) choline groups with respect to the location of the charged group in the permeant. In these figures the center of mass of the permeant is at the membrane center. Note the significant glycerol peak for the positively charged permeant suggesting significant screening effect. No such membrane group is found to support the negatively charged or zwitterion species. The plots also show the regular distribution of this species in an unperturbed membrane.

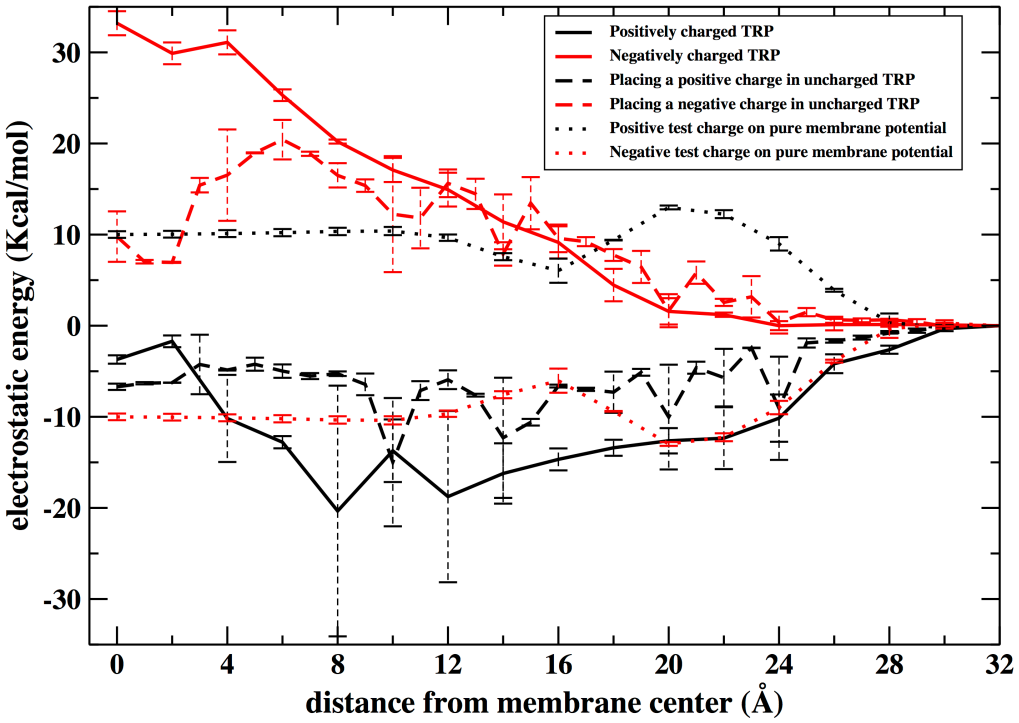

Figure 6.7: Electrostatic energy change on a translocating positive charge (black) or negative charge (red) moving inside the membrane. Alternate membrane sampling by Molecular Dynamics simulations are considered. Sampling system configurations with the charged peptides present the energy seen by the positive and negative charged tryptophan are shown with solid lines. Sampling membrane configurations by neutral tryptophan and then computing the energy of a positive charge placed on the nitrogen of the amino group or of a negative charge placed on the hydroxyl group of an uncharged tryptophan is shown with dashed lines. Finally, configurations sample of a pure DOPC membrane (no permeant) are used to place a point charge moving across an unperturbed membrane shown with dotted lines. Error bars are estimated by computing the

electrostatics energies for the two leaflets of the bilayer. The energies were shifted so they are all zero farther away from the membrane center. Note that the electric field computed without the permeant has an opposite tendency to perturbed membrane. It prefers transporting negative ions and not positively charged species. The unperturbed membrane results are in accord with the transport of organic ions [29] and Clarke theory.[5]

Permeant	Permeability coefficient (cm/s)
Zwitterionic tryptophan	$(2.2 \pm 1.3) \times 10^{-15}$
Positively charged tryptophan	$(2.2 \pm 2.0) \times 10^{-6}$
Negatively charged tryptophan	$(8.2 \pm 8.1) \times 10^{-15}$

Table 6.1: Permeability coefficients for tryptophan permeation with different charges. The range of values was estimated by computing the permeation independently for each half of the membrane. Note the significant range of values and that the permeation of the positively charged species is significantly larger in accord with experiment. The absolute value of the simulated permeation, however, is significantly larger than the experimental estimate.

6.4 REFERENCES

1. Alberts, B.; Johnson, A.; Lewis, J.; Raff, M.; Roberts, K.; Walter, P., *Molecular Biology of the Cell*; Garland Science: New York, **2008**.
2. Tepper, H. L.; Voth, G. A., Mechanisms of Passive Ion Permeation through Lipid Bilayers: Insights from Simulations. *J. Phys. Chem. B* **2006**, *110*, 21327-21337.
3. Chakrabarti, A. C. Permeability of Membranes to Amino-Acids and Modified Amino-Acids - Mechanisms Involved in Translocation. *Amino Acids* **1994**, *6*, 213−229.
4. Khavrutskii, I. V.; Gorfe, A. A.; Lu, B. Z.; McCammon, J. A., Free Energy for the Permeation of Na+ and Cl- Ions and Their Ion-Pair through a Zwitterionic Dimyristoyl Phosphatidylcholine Lipid Bilayer by Umbrella Integration with Harmonic Fourier Beads. *J. Am. Chem. Soc.* **2009**, *131*, 1706-1716.
5. Clarke, R. J., The Dipole Potential of Phospholipid Membranes and Methods for Its Detection. *Adv. Colloid Interface Sci.* **2001**, *89*, 263-281.
6. Wang, L. G., Measurements and Implications of the Membrane Dipole Potential. *Annu. Rev. Biochem,* **2012**, *81*, 615-635.
7. Liberman, Y. A.; Topaly, V. P. Permeability of Bimolecular Phospholipid Membranes for Fat-Soluble Ions. *Biofizika* **1969**, *14*, 452-61.
8. MacCallum, J. L.; Bennett, W. F. D.; Tieleman, D. P. Distribution of Amino Acids in a Lipid Bilayer from Computer Simulations. *Biophys. J.* **2008**, *94*, 3393−3404

9. Dorairaj, S.; Allen, T. W. On the Thermodynamic Stability of a Charged Arginine Side Chain in a Transmembrane Helix. *Proc. Natl. Acad. Sci. U.S.A.* **2007**, *104*, 4943−4948.
10. Yoo, J.; Cui, Q. Does Arginine Remain Protonated in the Lipid Membrane? Insights from Microscopic Pk(a) Calculations. *Biophys. J.* **2008**, *94*, L61−L63.
11. Li, L. B.; Vorobyov, I.; Allen, T. W. The Different Interactions of Lysine and Arginine Side Chains with Lipid Membranes. *J. Phys. Chem. B* **2013**, *117*, 11906−11920.
12. Gleason, N. J.; Vostrikov, V. V.; Greathouse, D. V.; Koeppe, R. E. Buried Lysine, but Not Arginine, Titrates and Alters Transmembrane Helix Tilt. *Proc. Natl. Acad. Sci. U.S.A.* **2013**, *110*, 1692− 1695.
13. Herce, H. D.; Garcia, A. E. Molecular Dynamics Simulations Suggest a Mechanism for Translocation of the Hiv-1 Tat Peptide across Lipid Membranes. *Proc. Natl. Acad. Sci. U.S.A.* **2007**, *104*, 20805−20810.
14. Huang, K.; Garcia, A. E. Free Energy of Translocating an Arginine-Rich Cell-Penetrating Peptide across a Lipid Bilayer Suggests Pore Formation. *Biophys. J.* **2013**, *104*, 412−420.
15. Cullis, P. R.; Hope, M. J.; Bally, M. B.; Madden, T. D.; Mayer, L. D.; Fenske, D. B. Influence of Ph Gradients on the Transbilayer Transport of Drugs, Lipids, Peptides and Metal Ions into Large Unilamellar Vesicles. *Biochim. Biophys. Acta.* **1997**, *1331*, 187−211.

16. Siva, K.; Elber, R. Ion Permeation through the Gramicidin Channel: Atomically Detailed Modeling by the Stochastic Difference Equation. *Proteins.* **2003**, 50, 63−80.

17. Bockmann, R. A.; Hac, A.; Heimburg, T.; Grubmuller, H. Effect of Sodium Chloride on a Lipid Bilayer. *Biophys. J.* **2003**, *85*, 1647− 1655.

18. Gurtovenko, A. A.; Vattulainen, I. Effect of Nacl and Kcl on Phosphatidylcholine and Phosphatidylethanolamine Lipid Membranes: Insight from Atomic-Scale Simulations for Understanding Salt-Induced Effects in the Plasma Membrane. *J. Phys. Chem. B* **2008**, *112*, 1953−1962.

19. Valley, C. C.; Perlmutter, J. D.; Braun, A. R.; Sachs, J. N. Nacl Interactions with Phosphatidylcholine Bilayers Do Not Alter Membrane Structure but Induce Long-Range Ordering of Ions and Water. *J. Membr. Biol.* **2011**, *244*, 35−42

20. Knecht, V.; Klasczyk, B. Specific Binding of Chloride Ions to Lipid Vesicles and Implications at Molecular Scale. *Biophys. J.* **2013**, *104*, 818−824

21. Missner, A.; Pohl, P. 110 Years of the Meyer-Overton Rule: Predicting Membrane Permeability of Gases and Other Small Compounds. *Chemphyschem.* **2009**, *10*, 1405−1414.

22. Marrink, S. J.; Berendsen, H. J. C. Simulation of Water Transport through a Lipid-Membrane. *J. Phys. Chem.* **1994**, *98*, 4155− 4168.

23. Marrink, S. J.; Berendsen, H. J. C. Permeation Process of Small Molecules across Lipid Membranes Studied by Molecular Dynamics Simulations. *J. Phys. Chem*. **1996**, *100*, 16729−16738.

24. Wilson, M. A.; Pohorille, A. Mechanism of Unassisted Ion Transport across Membrane Bilayers. *J. Am. Chem. Soc.* **1996**, *118*, 6580−6587.

25. Vorobyov, I.; Olson, T. E.; Kim, J. H.; Koeppe, R. E.; Andersen, O. S.; Allen, T. W. Ion-Induced Defect Permeation of Lipid Membranes. *Biophys. J.* **2014**, *106*, 586−597.

26. Ulander, J.; Haymet, A. D. J. Permeation across Hydrated Dppc Lipid Bilayers: Simulation of the Titrable Amphiphilic Drug Valproic Acid. *Biophys. J.* **2003**, *85*, 3475−3484.

27. Landolt-Bornstein, Zahlenwerte Und Funktionen Aus Physik, Chemie, Astronomie, Geophysik Und Technik; Springer: Berlin, 1969; Vol. II.

28. Mark, P.; Nilsson, L. A Molecular Dynamics Study of Tryptophan in Water. *J. Phys. Chem. B* **2002**, *106*, 9440−9445.

29. Saiz, L.; Klein, M. L. Electrostatic Interactions in a Neutral Model Phospholipid Bilayer by Molecular Dynamics Simulations. *J. Chem. Phys.* **2002**, *116*, 3052−3057.

30. Vorobyov, I.; Allen, T. W. The Electrostatics of Solvent and Membrane Interfaces and the Role of Electronic Polarizability. *J. Chem. Phys.* **2010**, *132*, 185101-1−185101-13.

31. Demchenko, A. P.; Yesylevskyy, S. O. Nanoscopic Description of Biomembrane Electrostatics: Results of Molecular Dynamics Simulations and Fluorescence Probing. *Chem. Phys. Lipids* **2009**, *160*, 63−84.

32. Humphrey, W.; Dalke, A.; Schulten, K. Vmd: Visual Molecular Dynamics. *J. Mol. Graphics Modell.* **1996**, *14*, 33-38.

Bibliography

1. Honig, B. H.; Hubbell, W. L.; Flewelling, R. F. Electrostatic Interactions in Membranes and Proteins. *Annu. Rev. Biophys. Biophys. Chem.* **1986**, *15*, 163-193.
2. McLaughlin, S. The Electrostatic Properties of Membranes. *Annu. Rev. Biophys. Biophys. Chem.* **1989**, *18*, 113-136.
3. Cevc, G. Membrane Electrostatics. *Biochim. Biophys. Acta*. **1990**, *1031*, 311-382.
4. Clarke, R. J. The Dipole Potential of Phospholipid Membranes and Methods for Its Detection. *Adv. Colloid Interface Sci.* **2001**, *89-90*, 263-281.
5. Brockman, H. Dipole Potential of Lipid Membranes. *Chem. Phys. Lipids.* **1994**, *73*, 57-79.
6. Liberman, Y. A.; Topaly, V. P.
7. Wang, L. Measurements and Implications of the Membrane Dipole Potential. *Annu. Rev. Biochem.* **2012**, *81*, 615-635.
8. Bechinger, B; Seelig, J. Interactions of Electric Dipoles with Phospholipid Head Groups. A ^{2}H and ^{31}P NMR Study of Phloretin and Phloretin Analogues in Phosphatidylcholine Membranes.
9. Schamberger, J.; Clarke, R. J. Hydrophobic Ion Hydration and the Magnitude of the Dipole Potential. *Biophys. J.* **2002**, *82*, 3081-3088.

10. Duffin, R. L.; Garrett, M. P.; Flake, K. B.; Durrant, J. D.; Busath, D. D. Modulation of Lipid Bilayer Interfacial Dipole Potential by Phloretin, RH421, and 6-ketocholestanol as Probed by Gramicidin Channel Conductance. *Langmuir* **2003,** *19*, 1439–1442.

11. Phillips, L. R.; Cole, C. D.; Hendershot, R. J.; Cotten, M.; Cross, T. A.; Busath, D. D. Noncontact Dipole Effects on Channel Permeation. III. Anomalous Proton Conductance Effects in Gramicidin. *Biophys. J.* **1999,** *77*, 2492–2501.

12. Hladky, S. B. The Energy Barriers to Ion Transport by Nonactin Across Thin Lipid Membranes. *Biochim. Biophys. Acta* **1974**, *352*, 71−85.

13. Bala, S.; Kombrabail, M. H.; Prabhananda, B. S. Effect of Phloretin on Ionophore Mediated Electroneutral Transmembrane Translocations of H(+), K(+) and Na(+) in Phospholipid Vesicles. *Biochim. Biophys. Acta*. **2001**, *1510*, 258−269

14. Cladera, J.; Martin, I.; Ruysschaert, J. M.; O'Shea, P. Characterization of the sequence of interactions of the fusion domain of the simian immunodeficiency virus with membranes. *J. Biol. Chem.* **1999**, *274*, 29951–29959.

15. Alakoskela, J.-M. I.; Kinnunen, P. K. J. Control of a Redox Reaction on Lipid Bilayer Surfaces by Membrane Dipole Potential. *Biophys. J.* **2001**, *80*, 294–304.

16. Alakoskela, J.-M. I.; Soderlund, T.; Holopainen, J. M.; Kinnunen, P. K. J. Dipole Potential and Head-group Spacing are Determinants for the Membrane Partitioning of Pregnanolone. *Mol. Pharmacol*. **2004**, *66*, 161–168.

17. Cladera, J.; O'Shea, P. Intramembrane Molecular Dipoles Affect the Membrane Insertion and Folding of a Model Amphiphilic Peptide. *Biophys. J.* **1998**, *74*, 2434–2442.

18. Starke-Peterkovic, T.; Turner, N.; Else, P. L.; Clarke, R. J. Electric Field Strength of Membrane Lipids From Vertebrate Species: Membrane Lipid Composition and Na1,K1-ATPase molecular activity. *Am. J. Physiol. Regul. Integr. Comp. Physiol.* **2005**, *288*, R663–R670.

19. Maggio, B. Modulation of Phospholipase A2 by Electrostatic Fields and Dipole Potential of Glycosphingolipids in Monolayers. *J. Lipid Res.* **1999**, *40*, 930–939.

20. Buzon, V.; Cladera, J. Effect of Cholesterol on the Interaction of the HIV GP41 Fusion Peptide with Model Membranes. Importance of the Membrane Dipole Potential. *Biochem* **2006**, *45*, 15768−15775.

21. Flewelling, R. F.; Hubbell, W. L. The Membrane Dipole Potential in a Total Membrane Potential Model. Applications to Hydrophobic Ion Interactions with Membranes. *Biophys. J.* **1986**, *49*, 541-552.

22. Franklin, J. C.; Cafiso, D. S. Internal Electrostatic Potentials in Bilayers: Measuring and Controlling Dipole Potentials in Lipid Vesicles. *Biophys. J.* **1993**, *65*, 289-299.

23. Gross, E.; Bedlack, R. S.; Loew, L. M. Dual-Wavelength Ratiometric Fluorescence Measurement of the Membrane Dipole Potential. *Biophys. J.* **1994**, *67*, 208-216.

24. Clarke, R. J. Effect of Lipid Structure on the Dipole Potential of Phosphatidylcholine Bilayers. *Biochim. Biophys. Acta* **1997**, *1327*, 269-278.

25. Klymchenko, A.S.; Duportail, G.; M´ely, Y.; Demchenko, A. P. Ultrasensitive Two-Color Fluorescence Probes for Dipole Potential in Phospholipid Membranes. *Proc. Natl. Acad. Sci. USA* **2003**, *100*, 11219–24.

26. Demchenko, A. P.; M´ely, Y.; Duportail, G.; Klymchenko, A. S. Monitoring Biophysical Properties of Lipid Membranes by Environment-Sensitive Fluorescent Probes. *Biophys. J.* **2009**, *96*, 3461–3470.

27. Demchenko, A. P.; Yesylevskyy, S. O. Nanoscopic Description of Biomembrane Electrostatics: Results of Molecular Dynamics Simulations and Fluorescence Probing. *Chem. Phys. Lipids.* **2009**, *160*, 63–84.

28. Zouni, A.; Clarke, R. J.; Holzwarth, J. F. Kinetics of the Solubilization of Styryl Dye Aggregates by Lipid Vesicles. *J. Phys. Chem*. **1994**, *98*, 1732–1738.

29. Wang, L.; Bose, P.S.; Sigworth, F. J. Using Cryo-EM to Measure the Dipole Potential of a Lipid Membrane. *PNAS.* **2006**, *103*, 18528-18533.

30. Yang, Y.; Mayer, K. M.; Wickremasignhs, N. S.; Hafner, J. H. Probing the Lipid Membrane Dipole Potential by Atomic Force Microscopy. *Biophys. J.* **2008**, *95*, 5193-5199.

31. Schamberger, J.; Clarke, R. J. Hydrophobic Ion Hydration and the Magnitude of the Dipole Potential. *Biophys. J.* **2002**, *82*, 3081-3088.

32. Chattopadhyay, A.; Boxer, S. G. Vibrational Stark Effect Spectroscopy. *J. Am. Chem. Soc.* **1995***, 117*, 1449-1450.

33. Fried, S. D.; Boxer, S. G. Measuring Electric Fields and Noncovalent Interactions Using the Vibrational Stark Effect. *Acc. Chem. Res.* **2015**, *48*, 998-1006.

34. Park, E. S.; Andrews, S. S.; Hu, R. B.; Boxer, S. G. Vibrational Stark Spectroscopy in Proteins: A Probe and Calibration for Electrostatic Fields. *J. Phys. Chem. B* **1999**, *103*, 9813-9817.

35. Saggu, M.; Levinson, N. M.; Boxer, S. G. Direct Measurements of Electric Fields in Weak O−H···π Hydrogen Bonds. *J. Am. Chem. Soc.* **2011**, *133*, 17414−17419.

36. Saggu, M.; Levinson, N. M.; Boxer, S. G. Experimental Quantification of Electrostatics in X−H···π Hydrogen Bonds. *J. Am. Chem. Soc.* **2012**, *134*, 18986−18997.

37. Andrews, S. S.; Boxer, S. G. Vibrational Stark Effects of Nitriles I. Methods and Experimental Results. *J. Phys. Chem. A.* **2000**, *104*, 11853−11863.

38. Fafarman, A. T.; Boxer, S. G. Nitrile Bonds as Infrared Probes of Electrostatics in Ribonuclease S. *J. Phys. Chem. B* **2010**, *114*, 13536− 13544.

39. Waegele, M. M.; Culik, R. M.; Gai, F. Site-Specific Spectroscopic Reporters of the Local Electric Field, Hydration, Structure, and Dynamics of Biomolecules. *J. Phys. Chem. Lett.* **2011**, *2*, 2598-2609.

40. Suydam, I. T.; Boxer, S. G. Vibrational Stark Effects Calibrate the Sensitivity of Vibrational Probes for Electric Fields in Proteins.*Biochem* **2003**, *42*, 12050−12055.

41. Fafarman, A. T.; Boxer, S. G. Nitrile Bonds as Infrared Probes of Electrostatics in Ribonuclease S. *J. Phys. Chem. B.* **2010**, *114*, 13536–13544.

42. Silverman, L. N.; Pitzer, M. E.; Ankomah, P. O.; Boxer, S. G.; Fenlon, E. E. Vibrational Stark Effect Probes for Nucleic Acids. *J. Phys. Chem. B.* **2007**, *111*, 11611-11613.

43. Getahun, Z.; Huang, C. Y.; Wang, T.; DeLeon, B.; DeGrado, W. F.; Gai, F. Using Nitrile-Derivatized Amino Acids as Infrared Probes of Local Environment. *J. Am. Chem. Soc.* **2003**, *125*, 405–411.

44. Stafford, A. J.; Ensign, D. L.; Webb, L. J. Vibrational Stark Effect Spectroscopy at the Interface of Ras and Rap1A Bound to the Ras Binding Domain of RalGDS Reveals an Electrostatic Mechanism for Protein-Protein Interaction. *J. Phys. Chem. B* **2010**, *114*, 15331–15344.

45. Webb, L. J.; Boxer, S. G. Electrostatic Fields Near the Active Site of Human Aldose Reductase: 1. New Inhibitors and Vibrational Stark Effect Measurements. *Biochem.* **2008**, *47*, 1588-1598.

46. Alfieri, K. N.; Vienneau, A. R.; Londergan, C. H. Using Infrared Spectroscopy of Cyanylated Cysteine To Map Membrane Binding Structure and Orientation of the Hybrid Antimicrobial Peptide CM15. *Biochem* **2011**, *50*, 11097-11108.

47. Mukherjee, S.; Chowdhury, P.; DeGrado, W. F.; Gai, F. Site- Specific Hydration Status of an Amphipathic Peptide in AOT Reverse Micelles. *Langmuir* **2007**, *23*, 11174–11179.

48. Tucker, M. J.; Getahun, Z.; Nanda, V.; DeGrado, W. F.; Gai, F. A New Method for Determining the Local Environment and Orientation of Individual Side Chains of Membrane-Binding Peptides. *J. Am. Chem. Soc.* **2004**, *126*, 5078–5079.

49. Liu, J.; Strzalka, J.; Tronin, A.; Johansson, J. S.; Blasie, J. K. Mechanism of Interaction between the General Anesthetic Halothane and a Model Ion Channel Protein, II: Fluorescence and Vibrational Spectroscopy Using a Cyanophenylalanine Probe. *Biophys. J.* **2009**, *96*, 4176–4187.

50. Hu, W.; Webb, L. J. Direct Measurement of the Membrane Dipole Field in Bicelles Using Vibrational Stark Effect Spectroscopy. *J. Phys. Chem. Lett.* **2011**, *2*, 1925-1930.

51. Andrews, S. S.; Boxer, S. G. Vibrational Stark Effects of Nitriles I. Methods and Experimental Results. *J. Phys. Chem. A* **2000**, *104*, 11853–11863.

52. Andrews, S. S.; Boxer, S. G. Vibrational Stark Effects of Nitriles II. Physical Origins of Stark Effects from Experiment and Perturbation Models. *J. Phys. Chem. A* **2002**, *106*, 469–477.

53. Ayers, B.; Blaschke, U. K.; Camarero, J. A.; Cotton, G. J.; Holford, M.; Muir, T. W. Introduction of Unnatural Amino Acids into Proteins Using Expressed Protein Ligation. *Biopolymers* **1999**, *51*, 343–354.

54. Cotton, G. J.; Muir, T. W. Generation of a Dual-Labeled Fluorescence Biosensor for Crk-II Phosphorylation Using Solid-Phase Expressed Protein Ligation. *Chem. Biol.* **2000**, *7*, 253–261.

55. Heim, R.; Prasher, D. C.; Tsien, R. Y. Wavelength Mutations and Posttranslational Autooxidation of Green Fluorescent Protein. *Proc. Natl. Acad. Sci. U.S.A.* **1994**, *91*, 12501–12504.

56. Furter, R. Expansion of the Genetic Code: Site-Directed p- Fluoro-phenylalanine Incorporation in E. coli. *Protein Sci.* **1998**, *7*, 419–426.

57. Wang, L.; Brock, A.; Herberich, B.; Schultz, P. G. Expanding the genetic code of E. coli. *Science* **2001**, *292*, 498–500.

58. Cowie, D. B.; Cohen, G. N. Biosynthesis by E. coli of Active Altered Proteins Containing Selenium Instead of Sulfur. *Biochim. Biophys. Acta* **1957**, *26*, 252–261.

59. Brawerman, G.; Ycas, M. Incorporation of the Amino Acid Analog Tryptazan into the Proteins of E. coli. Arch. *Biochem. Biophys.* **1957**, *68*, 112–117.

60. Munier, R.; Cohen, G. N. Incorporation of Structural Analo- gues of Amino Acid into the Bacterial Proteins during Their Synthesis in Vivo. *Biochim. Biophys. Acta* **1959**, *31*, 378–391.

61. Elber, R.; Roitberg, A.; Simmerling, C.; Goldstein, R.; Li, H. Y.; Verkhivker, G.; Keasar, C.; Zhang, J.; Ulitsky, A. Moil a program for simulations of macromolecules. *Comput. Phys. Commun.* **1995**, *91*, 159-189.

62. Ruymgaart, A.P.; Cardenas, A. E.; Elber, R. MOIL-opt: Energy-Conserving Molecular Dynamics on a GPU/CPU System. *J. Chem. Theory Comput.* **2011**, *7*, 3072–3082.

63. Berger, O.; Edholm, O.; Jähnig, F. Molecular dynamics simulations of a fluid bilayer of dipalmitoylphosphatidylcholine at full hydration, constant pressure, and constant temperature. *Biophys. J.* **1997**, *72*, 2002-2013.

64. Jorgensen, W. L.; Tiradorives, J. The OPLS Potential Functions for Proteins. Energy Minimization for Crystals of Cyclic Peptides and Crambin. *J. Am. Chem. Soc.* **1988**, *110*, 1657-1666.

65. Jo, S.; Kim, T.; Iyer, V. G.; Im, W. CHARMM-GUI: A web-based graphical user interface for CHARMM. *J. Comput. Chem.* **2008**, *29*, 1859-1865.

66. Jo, S.; Lim, J. B.; Klauda, J. B.; Im, W. CHARMM-GUI Membrane Builder for Mixed Bilayers and Its Application to Yeast Membranes. *Biophys. J.* **2009**, *97*, 50-58.

67. Jorgensen, W. L.; Chandrasekhar, J.; Madura, J. D.; Impey, R. W.; Klein, M. L. Comparison of simple potential functions for simulating liquid water. *J. Chem. Phys.* **1983**, *79*, 926-935.

68. Hu, W.; Webb, L. J. Direct Measurement of the Membrane Dipole Field in Bicelles Using Vibrational Stark Effect Spectroscopy. *J. Phys. Chem. Lett.* **2011**, *2*, 1925-1930.

69. Essmann, U.; Perera, L.; Berkowitz, M. L; Darden, T.; Lee, H.; Pedersen, L. G. A smooth particle mesh Ewald method. *J. Chem. Phys.* **1995**, *103*, 8577-8593.

70. Weinbach, Y.; Elber, R. Revisiting and parallelizing SHAKE. *J. Comput. Phys.* **2005**, *209*, 193-206.

71. Ryckaert, J. P.; Ciccotti, G.; Berendsen, H. J. C Numerical integration of the cartesian equations of motion of a system with constraints: molecular dynamics of n-alkanes. *J. Comput. Phys.* **1977**, *23*, 327-341.

72. Tuckerman, M.; Berne, B. J.; Martyna, G. J. Reversible multiple time scale molecular dynamics. *J. Chem. Phys.* **1992**, *97*, 1990-2001.

73. Patra, M.; Karttunen, M.; Hyvonet, M.T.; Falck, E.; Lindqvist, P.; Vattulainen, I. Molecular dynamics simulations of lipid bilayers: Major artifacts due to truncating electrostatics interactions. *Biophys. J.* **2003**, *84*, 3636-3645.

74. Morrissey, J. H. *Morrisey Lab Protocol for Preparing Phospholipid Vesicles (SUV) by Sonication*. Trigger Website. http://tf7.org/suv.pdf (accessed March 15, 2012).

75. Pasenkiewicz-Gierula, M.; Rog, T.; Kitamura, K.; Kusumi, A. Cholesterol effects on the phosphatidylcholine bilayer polar region: A molecular simulation study. *Biophys. J.* **2000**, *78*, 1376-1389

76. Price, M. L. P.; Ostrovsky, D.; Jorgensen, W. L. Gas-phase and liquid-state properties of esters, nitriles, and nitro compounds with the OPLS-AA force field. *J. Comput. Chem.* **2001**, *22*, 1340-1352

77. Berendsen, H. J. C.; Grigera, J. R.; Straatsma, T. P. THE MISSING TERM IN EFFECTIVE PAIR POTENTIALS. *J. Phys. Chem.* **1987**, *91*, 6269-6271

78. Di Pierro, M.; Elber, R.; Leimkuhler, B. A Stochastic Algorithm for the Isobaric-Isothermal Ensemble with Ewald Summations for All Long Range Forces. *J Chem Theory Comput* **2015**, *11*, 5624-5637

79. Egberts, E.; Berendsen, H. J. C. Molecular-Dynamics Simulation of a Smectic Liquid-Crystal with Atomic Detail. *J. Chem. Phys.* **1988**, *89*, 3718-3732

80. Liu, Y. F.; Nagle, J. F. Diffuse Scattering Provides Material Parameters and Electron Density Profiles of Biomembranes. *Phys. Rev. E* **2004**, *69*, 040901-1−040901-4.

81. Jorgensen, W. L.; Tiradorives, J. The Opls Potential Functions for Proteins - Energy Minimizations for Crystals of Cyclic-Peptides and Crambin. *J. Am. Chem. Soc.* **1988**, *110*, 1657−1666.

82. Berger, O.; Edholm, O.; Jahnig, F. Molecular Dynamics Simulations of a Fluid Bilayer of Dipalmitoylphosphatidylcholine at Full Hydration, Constant Pressure, and Constant Temperature. *Biophys. J.* **1997**, *72*, 2002−2013.

83. Berendsen, H. J. C.; Grigera, J. R.; Straatsma, T. P. The Missing Term in Effective Pair Potentials. *J. Phys. Chem.* **1987**, *91*, 6269−6271.

84. Essmann, U.; Perera, L.; Berkowitz, M. L.; Darden, T.; Lee, H.; Pedersen, L. G.; Smooth, A. Particle Mesh Ewald Method. *J. Chem. Phys*. **1995**, *103*, 8577−8593.

85. Weinbach, Y.; Elber, R. Revisiting and Parallelizing Shake. *J. Comput. Phys.* **2005**, *209*, 193−206.

86. Ryckaert, J. P.; Ciccotti, G.; Berendsen, H. J. C. Numerical Integration of Cartesian Equations of M Otion of a System with Constraints - Molecular Dynamics of N-Alkanes. *J. Comput. Phys*. **1977**, *23*, 327−341.

87. Tuckerman, M.; Berne, B. J.; Martyna, G. J. Reversible Multiple Time Scale Molecular-Dynamics. *J. Chem. Phys.* **1992**, *97*, 1990−2001.

88. Cardenas, A. E.; Jas, G. S.; DeLeon, K. Y.; Hegefeld, W. A.; Kuczera, K.; Elber, R. Unassisted Transport of N-Acetyl-LTryptophanamide through Membrane: Experiment and Simulation of Kinetics. *J. Phys. Chem. B* **2012**, *116*, 2739−2750.

89. Marrink, S. J.; Berendsen, H. J. C. Simulation of Water Transport through a Lipid-Membrane. *J. Phys. Chem.* **1994,** *98*, 4155− 4168.

90. Marrink, S. J.; Berendsen, H. J. C. Permeation Process of Small Molecules across Lipid Membranes Studied by Molecular Dynamics Simulations. *J. Phys. Chem.* **1996**, *100*, 16729−16738.

91. Kirmizialtin, S.; Elber, R. Computational Exploration of Mobile Ion Distributions around Rna Duplex. *J. Phys. Chem. B* **2010**, *114*, 8207−8220.

92. Straub, J. E.; Thirumalai, D. Exploring the Energy Landscape in Proteins. *Proc. Natl. Acad. Sci. U.S.A.* **1993**, *90*, 809−813.

93. Szoka, F. Jr.; Papahadjopoulos, D. Comparative Properties and Methods of Preparation of Lipid Vesicles (Liposomes). *Ann. Rev. Biophys. Bioeng.* **1980**, *9*, 467-508.

94. Huang, C. Studies on Phosphatidylcholine Vesicles. Formation and Physical Characteristics. *Biochem.* **1969**, *8 (1),* 344-352.

95. Kumar, V. V.; Baumann, W. J. Bilayer Asymmetry in Lysophosphatidylcholine/Cholesterol (1:1) Vesicles. A Phosphorus-31 NMR

Study. *Biochemical and Biophysical Research Communications* **1986**, *139*, 25-30.

96. Fenske, D. B. Structural and Motional Properties of Vesicles as revealed by Nuclear Magnetic Resonance. *Chem. Phys. Lipids.* **1993**, *64*, 143-16219.

97. Bystrov, V. F.; Shapiro, Y. E.; Viktorov, A. V.; Barsukov, L. I.; Bergelson, L. D. ^{31}P-NMR signals from inner and outer surfaces of phospholipid membranes. *FEBS Lett.* **1972,** *25*, 337-338

98. Fröhlich, M.; Brecht, V.; Peschka-Süss, R. Parameters Influencing the Determination of Liposome Lamellarity by ^{31}P-NMR. *Chemistry and Physics of Lipids.* **2001**, *109*, 103-112.

99. Xue-Feng, L.; Gao-Yong, Z.; Jin-Feng, Dong.; Xiao-Hai, Z.; Xin-Lin, H. An Atomic Force Microscopy Study on Small Unilamellar Vesicle Structures on Mica. *Chin. J. Chem*. **2006**, *24*, 311-315.

100. Teschke, O.; de Souza, E. F. Liposome Structure Imaging by Atomic Force Microscopy: Verification of Improved Liposome Stability during Adsorption of Multiple Aggregate. *Langmuir* **2002**, *18*, 6513-6520.

101. Hessa, T.; Kim, H.; Bihlmaier, K.; Lundin, C.; Boekel, J.; Andersson, H.; Hilsson, I.; White, S. H.; Heijne, G. von. Recognition of Transmembrane Helices by the Endoplasmic Reticulum Translocon. *Nature* **2005**, *433*, 377-381.

102. Johansson, A. C. V.; Lindahl, E. Amino-Acid Solvation Structure in Transmembrane Helices from Molecular Dynamics Simulations. *Biophys. J.* **2006**, *91*, 4450-4463.

103. Hu, W.; Webb, L. J. Direct Measurement of the Membrane Dipole Field in Bicelles Using Vibrational Stark Effect Spectroscopy. *J. Phys. Chem. Lett.* **2011**, *2*, 1925-1930.

104. Kelly, S. M.; Price, N. C. The Use of Circular Dichroism in the Investigation of Protein Structure and Function. *Current Protein and Peptide Science.* **2000**, *1*, 349-384.

105. Litman, B. J. Effect of Light Scattering on the Circular Dichroism of Biological Membranes. *Biochem* **1972**, *11*, 3243-3247.

106. Kučerka, N.; Nieh, M. P.; Katsaras, J. Fluid Phase Lipid Areas and Bilayer Thicknesses of Commonly Used Phosphatidylcholines as a Function of Temperature. *Biochim. Biophys. Acta.* **2011**, *1808*, 2761-2771.

107. Kučerka, N.; Liu, Y.; Chu, N.; Petrache, H. I.; Tristram-Nagle, S.; Nagle, J. F. Structure of Fully Hydrated Fluid Phase DMPC and DLPC Lipid Bilayers Using X-Ray Scattering from Oriented Multilamellar Arrays and from Unilamellar Vesicles. *Biophys. J.* **2005**, *88*, 2626-2637.

108. Webb, R. J.; East, J. M.; Sharma, R. P.; Lee, A. G. Hydrophobic Mismatch and the Incorporation of P1eptides into Lipid Bilayers: A Possible Mechnaism for Retention in the Golgi. *Biochem* **1998**, *37*, 673-679.

109. Getahun, Z.; Huang, C. Y.; Wang, T.; DeLeon, B.; DeGrado, W. F.; Gai, F. Using Nitrile-Derivatized Amino Acids as Infrared Probes of Local Environment. *J. Am. Chem. Soc.* **2003**, *125*, 405–411.

110. Waegele, M. M.; Culik, R. M.; Gai, F. Site-Specific Spectroscopic Reporters of the Local Electric Field, Hydration, Structure, and Dynamics of Biomolecules. *J. Phys. Chem. Lett.* **2011**, *2*, 2598-2609.

111. Getahun, Z.; Huang, C. Y.; Wang, T.; DeLeon, B.; DeGrado, W. F.; Gai, F. Using Nitrile-Derivatized Amino Acids as Infrared Probes of Local Environment. *J. Am. Chem. Soc.* **2003**, *125*, 405–411.

112. van Meer, G. Lipid traffic in animal cells. *Annu. Rev. Cell. Biol.* **1989**, *5*, 247-275.

113. Léonard, A.; Dufourc, E. J. Interactions of Cholesterol with the Membrane Lipid Matrix. A Solid State NMR Approach. *Biochimie* **1991**, *73*, 1295-1302.

114. Jacobs, R.; Oldfield, E. Deuterium Nuclear Magnetic Resonance Investigation of Dimyristoyllecithin-Dipalmitoyllecithin and Dimyristoyllecithin-Cholesterol Mixtures. *Biochem* **1979**, *18*, 3280-3285.

115. Veatch, S. L.; Polozov, I. V.; Gawrisch, K.; Keller, S. L. Liquid Domain in Vesicles Investigated by NMR and Fluorescence Microscopy. *Biophys. J.* **2004**, *86*, 2910-2922.

116. Bin, X.; Lipkowski, J. Electrochemical and PM-IRRAS Studies of the Effect of Cholesterol on the Properties of the Headgroup Region of a DMPC Bilayer Supported at a Au(111) Electrode. *J. Phys. Chem. B* **2006**, *110*, 26430–26441.

117. Shimshick, E. J.; McConnel, H. M. Lateral Phase Separations in Binary-Mixtures of Cholesterol and Phospholipids. *Biochem. Biophys. Res. Commun.* **1973**, *53,* 446-451.

118. Oldfield, E.; Chapman, D. Effects of Cholesterol and Cholesterol Derivatives on Hydrocarbon Chain Mobility in Lipids. *Biochem. Biophys. Res. Commun.* **1971,** *43*, 610-616.

119. Mainali, L.; Raguz, M.; Subczynski, W. K. Formation of Cholesterol Bilayer Domains Precedes Formation of Cholesterol Crystals in Cholesterol/Dimyristoylphosphatidylcholine Membranes: EPR and DSC Studies. *J. Phys. Chem. B*. **2013,** *117,* 8994-9003.

120. Mabrey, S.; Sturtevant, J. M. Investigation of Phase Transitions of Lipids and Lipid Mixtures by High Sensitivity Differential Scanning Calorimetry. *Proc. Natl. Acad. Sci. USA*. **1976,** *73*, 3862–3866.

121. Blandamer, M. J.; Briggs, B.; Cullis, P. M.; Rawlings, B. J.; Engberts, J. B. F. N. Vesicle-Cholesterol Interactions: Effects of Added Cholesterol on Gel-to-Liquid Crystal Transitions in a Phospholipid Membrane and Five Dialkyl-based Vesicles as Monitored Using DSC. *Phys. Chem. Chem. Phys.* **2003**, *5*, 5309-5312

122. McMullen, T. P. W.; McElhaney, R. N. New Aspects of the Interaction of Cholesterol with Dipalmitoylphosphatidylcholine Bilayers as Revealed by High-Sensitivity Differential Scanning Calorimetry. *Biochim. Biophys. Acta.* **1995**, *1234*, 90-98.

123. McMullen, T. P. W.; Lewis, R. N. A. H.; McElhaney, R. N. Cholesterol–Phospholipid Interactions, the Liquid-Ordered Phase and Lipid Rafts in Model and Biological Membranes. *Curr. Opin. Colloid Interface Sci.* **2004**, *8*, 459–468.

124. Efimova, S. S.; Ostroumova, O. S. Effect of Dipole modifiers on the Magnitude of the Dipole Potential of Sterol-Containing Bilayers. *Langmuir* **2012,** *28,* 9908-9914

125. Haldar, S.; Kanaparthi, R. K.; Samanta, A.; Chattopadhyay, A. Differential Effect of Cholesterol and Its Biosynthetic Precursors on Membrane Dipole Potential. *Biophys. J.* **2012,** *102,* 1561-1569.

126. Starke-Peterkovic, T.; Turner, N.; Vitha, M. F.; Waller, M. P.; Hibbs, D. E. Cholesterol Effect on the Dipole Potential of Lipid Membranes. *Biophys. J.* **2006,** *90,* 4060-4070.

127. Szabo, G. Dual Mechanism for the Action of Cholesterol on Membrane Permeability. *Nature.* **1974**, *252*, 47–49.

128. McIntosh, T. J., Magid, A. D.; Simon, S. A. Cholesterol Modifies the Short-range Repulsive Interactions Between Phosphatidyl- choline Membranes. *Biochem.* **1989**, *28*, 17–25.

129. Hofsäβ, C.; Lindahl, E.; Edholm, O. Molecular Dynamics Simulations of Phospholipid Bilayers with Cholesterol. *Biophys. J.* **2003**, *84*, 2192-2206.

130. Smondyrev, A. M.; Berkowitz, M. L. Structure of Dipalmitoylphosphatidylcholine/Cholesterol Bilayer at Low and High Cholesterol Concentrations: Molecular Dynamics Simulation. Biophys. J. **1999**, *77*, 2075-2089.

131. Chiu, S. W.; Jakobsson, E.; Scott, H. L. Combined Monte Carlo and Molecular Dynamics Simulation of Hydrated Dipalmitoyl–phosphatidylcholine–Cholesterol Lipid Bilayers. *J. Chem. Phys.* **2001**, *114*, 5432-5443.

132. Gabdoulline, R. R.; Vanderkooi, G.; Zheng, C. Comparison of the Structures of Dimyristoylphosphatidylcholine in the Presence and Absence of Cholesterol by Molecular Dynamics Simulations. *J. Phys. Chem.* **1996**, *100*, 15942-15946.

133. Yang, Y.; Mayer, K. M.; Wickremasignhs, N. S.; Hafner, J. H. Probing the Lipid Membrane Dipole Potential by Atomic Force Microscopy. *Biophys. J.* **2008**, *95*, 5193-5199.

134. Franklin, J. C.; Cafiso, D. S. Internal Electrostatic Potentials in Bilayers: Measuring and Controlling Dipole Potentials in Lipid Vesicles. *Biophys. J.* **1993**, *65*, 289-299.

135. Gross, E.; Bedlack, R. S.; Loew, L. M. Dual-Wavelength Ratiometric Fluorescence Measurement of the Membrane Dipole Potential. *Biophys. J.* **1994**, *67*, 208-216.

136. Haldar, S.; Kanaparthi, R. K.; Samanta, A.; Chattopadhyay, A. Differential Effect of Cholesterol and Its Biosynthetic Precursors on Membrane Dipole Potential. *Biophys. J.* **2012**, *102*, 1561-1569.

137. Efimova, S. S.; Ostroumova, O. S. Effect of Dipole Modifiers on the Magnitude of the Dipole Potential of Sterol-Containing Bilayers. *Langmuir* **2012**, *28*, 9908-9914.

138. Smondyrev, A. M.; Berkowitz, M. L. Effects of Oxygenated Sterol on

Phospholipid Bilayer Properties: a Molecular Dynamics Simulation. *Chem. Phys. Lipids.* **2001**, *112*, 31-39.

139. Simon, S. A.; McIntosh, T. J.; Magid, A. D.; Needham, D. Modulation of the Interbilayer Hydration Pressure by the Addition of Dipoles at the Hydrocarbon/Water Interface. *Biophys. J.* **1992**, *61*, 786–799.
140. Duffin, R. L.; Garrett, M. P.; Flake, K. B.; Durrant, J. D.; Busath, D. D. Modulation of Lipid Bilayer Interfacial Dipole Potential by Phloretin, RH421, and 6-ketocholestanol as Probed by Gramicidin Channel Conductance. *Langmuir* **2003,** *19*, 1439–1442.
141. Johansson, A. C. V.; Lindahl, E. Amino-Acid Solvation Structure in Transmembrane Helices from Molecular Dynamics Simulations. *Biophys. J.* **2006**, *91*, 4450**-**4463.
142. Kelly, S. M.; Price, N. C. The Use of Circular Dichroism in the Investigation of Protein Structure and Function. *Current Protein and Peptide Science.* **2000**, *1*, 349-384.
143. Hu, W.; Webb, L. J. Direct Measurement of the Membrane Dipole Field in Bicelles Using Vibrational Stark Effect Spectroscopy. *J. Phys. Chem. Lett.* **2011**, *2*, 1925-1930.
144. Shrestha, R.; Cardenas, A. E.; Elber, R.; Webb, L. J. Measurement of the Membrane Dipole Electric Field in DMPC Vesicles Using Vibrational Shifts of *p*-Cyanophenylalanine and Molecular Dynamics Simulations. *J. Phys. Chem. B.* **2015**, *119*, 2869-2876.

145. Getahun, Z.; Huang, C. Y.; Wang, T.; DeLeon, B.; DeGrado, W. F.; Gai, F. Using Nitrile-Derivatized Amino Acids as Infrared Probes of Local Environment. *J. Am. Chem. Soc.* **2003**, *125*, 405–411.

146. Kučerka, N.; Nieh, M. P.; Katsaras, J. Fluid Phase Lipid Areas and Bilayer Thicknesses of Commonly Used Phosphatidylcholines as a Function of Temperature. *Biochim. Biophys. Acta.* **2011**, *1808*, 2761-2771.

147. Khelashvili, G.; Pabst, G.; Harries, D. Cholesterol Orientation and Tilt Modulus in DMPC Bilayers. *J. Phys. Chem. B.* **2010**, *114*, 7524-7534.

148. Rog, T.; Pasenkiewicz-Gierula, M. Cholesterol Effects on the Phosphatidylcholine Bilayer Nonpolar Region: A Molecular Simulation Study. *Biophys. J.* **2001**, *81*, 2190-2202.

149. Jedlovszky, P.; Mezei, M. Effect of Cholesterol on the Properties of Phospholipid Membranes. 1. Structural Features. *J. Phys. Chem. B.* **2003***, 107*, 5311-5321.

150. Henriksen, J.; Rowat, A. C.; Brief, E.; Hsueh, Y. W.; Thewalt, J. L.; Zuckermann, M. J.; Ipsen, J. H. Universal Behaviour of Membranes with Sterols. *Biophys. J.* **2006**, *90*,1639-1649.

151. Smaby, J. M.; Momsen, M.; Brockman, H. L.; Brown, R. E. Phosphatidylcholine Acyl Unsaturation Modulates the Decrease in Interfacial Elasticity Induced by Cholesterol. *Biophys. J.* **1997**, *73*, 1492-1505.

152. Marsh, D.; Smith, I. C. P. Interacting Spin Labels as Probes of Molecular Separation within Phospholipid Bilayers. *Biochem. Biophys. Res. Commun.*

1972, *49*, 916-922.

153. Kusumi, A.; Tsuda, M.; Akino, T.; Ohnishi, S.; Terayama, Y. Protein-Phospholipid-Cholesterol Interaction in the Photolysis Invertebrate Rhodopsin. *Biochem.* **1983**, *22*, 1165-1170.
154. Mouritsen, O. G.; Jørgensen, K. Dynamical Order and Disorder in Lipid Bilayers. *Chem. Phys. Lipids.* **1994**, *73*, 3-25.
155. McConnell, H. M.; Radhakrishnan, A. Condensed Complexes of Cholesterol and Phospholipids. *Biochim. Biophys. Acta.* **2003**, *1610*, 159-173.
156. Ohvo-Rekila, H.; Ramstedt, B.; Leppimaki, P.; Slotte, J. P. Cholesterol Interactions with Phospholipids in Membranes. *Prog. Lipid Res.* **2002**, *41*, 66-97.
157. Rheinstadter, M. C.; Mouritsen, O. G. Small-Scale Structure in Fluid Cholesterol-Lipid Bilayers. *Curr. Opin. Colloid Interface Sci.* **2013***, 18*, 440-447.
158. de Meyer, F.; Smit, B. Effect of Cholesterol on the Structure of a Phospholipid Bilayer. *PNAS*. **2009**, *106*, 3654-3658.
159. Ipsen, J. H.; Karlstrom, G.; Mouritsen, O. G.; Wennerstrom, H.; Zuckermann, M. J. Phase Equilibria in the Phosphatidylcholine-Cholesterol system. *Biochim. Biophys. Acta.* **1987**, *905*, 162-172.
160. Alberts, B.; Johnson, A.; Lewis, J.; Raff, M.; Roberts, K.; Walter, P., *Molecular Biology of the Cell*; Garland Science: New York, **2008**.
161. Tepper, H. L.; Voth, G. A., Mechanisms of Passive Ion Permeation through

Lipid Bilayers: Insights from Simulations. *J. Phys. Chem. B* **2006**, *110*, 21327-21337.

162. Chakrabarti, A. C. Permeability of Membranes to Amino-Acids and Modified Amino-Acids - Mechanisms Involved in Translocation. *Amino Acids* **1994**, *6*, 213−229.

163. Khavrutskii, I. V.; Gorfe, A. A.; Lu, B. Z.; McCammon, J. A., Free Energy for the Permeation of Na+ and Cl- Ions and Their Ion-Pair through a Zwitterionic Dimyristoyl Phosphatidylcholine Lipid Bilayer by Umbrella Integration with Harmonic Fourier Beads. *J. Am. Chem. Soc.* **2009**, *131*, 1706-1716.

164. Clarke, R. J., The Dipole Potential of Phospholipid Membranes and Methods for Its Detection. *Adv. Colloid Interface Sci.* **2001**, *89*, 263-281.

165. Wang, L. G., Measurements and Implications of the Membrane Dipole Potential. *Annu. Rev. Biochem,* **2012**, *81*, 615-635.

166. Liberman, Y. A.; Topaly, V. P. Permeability of Bimolecular Phospholipid Membranes for Fat-Soluble Ions. *Biofizika* **1969**, *14*, 452-61.

167. MacCallum, J. L.; Bennett, W. F. D.; Tieleman, D. P. Distribution of Amino Acids in a Lipid Bilayer from Computer Simulations. *Biophys. J.* **2008**, *94*, 3393−3404

168. Dorairaj, S.; Allen, T. W. On the Thermodynamic Stability of a Charged Arginine Side Chain in a Transmembrane Helix. *Proc. Natl. Acad. Sci. U.S.A.* **2007**, *104*, 4943−4948.

169. Yoo, J.; Cui, Q. Does Arginine Remain Protonated in the Lipid Membrane? Insights from Microscopic Pk(a) Calculations. *Biophys. J.* **2008**, *94*, L61−L63.

170. Li, L. B.; Vorobyov, I.; Allen, T. W. The Different Interactions of Lysine and Arginine Side Chains with Lipid Membranes. *J. Phys. Chem. B* **2013**, *117*, 11906−11920.

171. Gleason, N. J.; Vostrikov, V. V.; Greathouse, D. V.; Koeppe, R. E. Buried Lysine, but Not Arginine, Titrates and Alters Transmembrane Helix Tilt. *Proc. Natl. Acad. Sci. U.S.A.* **2013**, *110*, 1692− 1695.

172. Herce, H. D.; Garcia, A. E. Molecular Dynamics Simulations Suggest a Mechanism for Translocation of the Hiv-1 Tat Peptide across Lipid Membranes. *Proc. Natl. Acad. Sci. U.S.A.* **2007**, *104*, 20805−20810.

173. Huang, K.; Garcia, A. E. Free Energy of Translocating an Arginine-Rich Cell-Penetrating Peptide across a Lipid Bilayer Suggests Pore Formation. *Biophys. J.* **2013**, *104*, 412−420.

174. Cullis, P. R.; Hope, M. J.; Bally, M. B.; Madden, T. D.; Mayer, L. D.; Fenske, D. B. Influence of Ph Gradients on the Transbilayer Transport of Drugs, Lipids, Peptides and Metal Ions into Large Unilamellar Vesicles. *Biochim. Biophys. Acta.* **1997**, *1331*, 187−211.

175. Siva, K.; Elber, R. Ion Permeation through the Gramicidin Channel: Atomically Detailed Modeling by the Stochastic Difference Equation. *Proteins.* **2003**, 50, 63−80.

176. Bockmann, R. A.; Hac, A.; Heimburg, T.; Grubmuller, H. Effect of Sodium Chloride on a Lipid Bilayer. *Biophys. J.* **2003**, *85*, 1647− 1655.

177. Gurtovenko, A. A.; Vattulainen, I. Effect of Nacl and Kcl on Phosphatidylcholine and Phosphatidylethanolamine Lipid Membranes: Insight from Atomic-Scale Simulations for Understanding Salt-Induced Effects in the Plasma Membrane. *J. Phys. Chem. B* **2008**, *112*, 1953−1962.

178. Valley, C. C.; Perlmutter, J. D.; Braun, A. R.; Sachs, J. N. Nacl Interactions with Phosphatidylcholine Bilayers Do Not Alter Membrane Structure but Induce Long-Range Ordering of Ions and Water. *J. Membr. Biol.* **2011**, *244*, 35−42

179. Knecht, V.; Klasczyk, B. Specific Binding of Chloride Ions to Lipid Vesicles and Implications at Molecular Scale. *Biophys. J.* **2013**, *104*, 818−824

180. Missner, A.; Pohl, P. 110 Years of the Meyer-Overton Rule: Predicting Membrane Permeability of Gases and Other Small Compounds. *Chemphyschem.* **2009**, *10*, 1405−1414.

181. Marrink, S. J.; Berendsen, H. J. C. Simulation of Water Transport through a Lipid-Membrane. *J. Phys. Chem.* **1994**, *98*, 4155− 4168.

182. Marrink, S. J.; Berendsen, H. J. C. Permeation Process of Small Molecules across Lipid Membranes Studied by Molecular Dynamics Simulations. *J. Phys. Chem*. **1996**, *100*, 16729−16738.

183. Wilson, M. A.; Pohorille, A. Mechanism of Unassisted Ion Transport across Membrane Bilayers. *J. Am. Chem. Soc.* **1996**, *118*, 6580−6587.

184. Vorobyov, I.; Olson, T. E.; Kim, J. H.; Koeppe, R. E.; Andersen, O. S.; Allen, T. W. Ion-Induced Defect Permeation of Lipid Membranes. *Biophys. J.* **2014**, *106*, 586−597.

185. Ulander, J.; Haymet, A. D. J. Permeation across Hydrated Dppc Lipid Bilayers: Simulation of the Titrable Amphiphilic Drug Valproic Acid. *Biophys. J.* **2003**, *85*, 3475−3484.

186. Landolt-Bornstein, Zahlenwerte Und Funktionen Aus Physik, Chemie, Astronomie, Geophysik Und Technik; Springer: Berlin, 1969; Vol. II.

187. Mark, P.; Nilsson, L. A Molecular Dynamics Study of Tryptophan in Water. *J. Phys. Chem. B* **2002**, *106*, 9440−9445.

188. Saiz, L.; Klein, M. L. Electrostatic Interactions in a Neutral Model Phospholipid Bilayer by Molecular Dynamics Simulations. *J. Chem. Phys.* **2002**, *116*, 3052−3057.

189. Vorobyov, I.; Allen, T. W. The Electrostatics of Solvent and Membrane Interfaces and the Role of Electronic Polarizability. *J. Chem. Phys.* **2010**, *132*, 185101-1−185101-13.

190. Demchenko, A. P.; Yesylevskyy, S. O. Nanoscopic Description of Biomembrane Electrostatics: Results of Molecular Dynamics Simulations and Fluorescence Probing. *Chem. Phys. Lipids* **2009**, *160*, 63−84.

191. Humphrey, W.; Dalke, A.; Schulten, K. Vmd: Visual Molecular Dynamics. *J. Mol. Graphics Modell.* **1996**, *14*, 33-38.

Vita

Rebika Shrestha was born and raised in the Himalayan country of Nepal. After finishing GCE Cambridge A-levels from Budhanilkantha School in Kathmandu, Nepal, she joined Randolph Macon Woman's College in Lynchburg, VA for her undergraduate studies. In 2010, she completed her undergraduate degree with Bachelor of Science in Mathematics and Bachelor of Science in Chemistry with Departmental Honors. She worked as a Chemist at TEVA Pharmaceuticals and Sigmapharm Laboratories in Pennsylvania for a year. In 2011, she started her graduate school at the University of Texas at Austin and worked under Dr. Lauren J. Webb.

Permanent email: rebikasth@gmail.com

This dissertation was typed by Rebika Shrestha.